ISSN 2587-1366

TURKISH JOURNAL OF ENGINEERING

VOLUME 5 ISSUE 4 OCTOBER 2021

JOURNAL SECRETARY

TURKISH JOURNAL OF ENGINEERING (TUJE)

Turkish Journal of Engineering (TUJE) is a multi-disciplinary journal. The Turkish Journal of Engineering (TUJE) publishes the articles in English and is being published 4 times (January, April, July and October) a year. The Journal is a multidisciplinary journal and covers all fields of basic science and engineering. It is the main purpose of the Journal that to convey the latest development on the science and technology towards the related scientists and to the readers. The Journal is also involved in both experimental and theoretical studies on the subject area of basic science and engineering. Submission of an article implies that the work described has not been published previously and it is not under consideration for publication elsewhere. The copyright release form must be signed by the corresponding author on behalf of all authors. All the responsibilities for the article belongs to the authors. The publications of papers are selected through double peer reviewed to ensure originality, relevance and readability.

AIM AND SCOPE

The Journal publishes both experimental and theoretical studies which are reviewed by at least two scientists and researchers for the subject area of basic science and engineering in the fields listed below:

- Aerospace Engineering
- Environmental Engineering
- Civil Engineering
- Geomatic Engineering
- Mechanical Engineering
- Geology Science and Engineering
- Mining Engineering
- Chemical Engineering
- Metallurgical and Materials Engineering
- Electrical and Electronics Engineering
- Mathematical Applications in Engineering
- Computer Engineering
- Food Engineering

PEER REVIEW PROCESS

All submissions will be scanned by iThenticate® to prevent plagiarism. Author(s) of the present study and the article about the ethical responsibilities that fit PUBLICATION ETHICS agree. Each author is responsible for the content of the article. Articles submitted for publication are priorly controlled via iThenticate ® (Professional Plagiarism Prevention) program. If articles that are controlled by iThenticate® program identified as plagiarism or self-plagiarism with more than 25% manuscript will return to the author for appropriate citation and correction. All submitted manuscripts are read by the editorial staff. To save time for authors and peer-reviewers, only those papers that seem most likely to meet our editorial criteria are sent for formal review. Reviewer selection is critical to the publication process, and we base our choice on many factors, including expertise, reputation, specific recommendations and our own previous experience of a reviewer's characteristics. For instance, we avoid using people who are slow, careless or do not provide reasoning for their views, whether harsh or lenient. All submissions will be double blind peer reviewed. All papers are expected to have original content. They should not have been previously published and it should not be under review. Prior to the sending out to referees, editors check that the paper aim and scope of the journal. The journal seeks minimum three independent referees. All submissions are subject to a double blind peer review; if two of referees gives a negative feedback on a paper, the paper is being rejected. If two of referees gives a positive feedback on a paper and one referee negative, the editor can decide whether accept or reject. All submitted papers and referee reports are archived by journal Submissions whether they are published or not are not returned. Authors who want to give up publishing their paper in TUJE after the submission have to apply to the editorial board in written. Authors are responsible from the writing quality of their papers. TUJE journal will not pay any copyright fee to authors. A signed Copyright Assignment Form has to be submitted together with the paper.

PUBLICATION ETHICS

Our publication ethics and publication malpractice statement is mainly based on the Code of Conduct and Best-Practice Guidelines for Journal Editors. Committee on Publication Ethics (COPE). (2011, March 7). Code of Conduct and Best-Practice Guidelines for Journal Editors. Retrieved from http://publicationethics.org/files/Code%20of%20Conduct_2.pdf

PUBLICATION FREQUENCY

The TUJE accepts the articles in English and is being published 4 times (January, April, July and October) a year.

CORRESPONDENCE ADDRESS

Journal Contact: tuje@mersin.edu.tr

CONTENTS

Volume 5 – Issue 4

ARTICLES

Turkish Journal of Engineering

https://dergipark.org.tr/en/pub/tuje

e-ISSN 2587-1366

Fuzzy-Optimized model reference adaptive control of interacting and noninteracting processes based on MIT and Lyapunov rules

Demilade D. Dinakin *1, **Peter O. Oluseyi** 1

1*University of Lagos, Faculty of Engineering, Department of Electrical and Electronics Engineering, Lagos, Nigeria*

Keywords
Adaptation gain
Fuzzy Logic Control (FLC)
Lyapunov rule
MIT rule
Model reference
Adaptive control

ABSTRACT

Various system parameter variations occur during operations in several existing process industries. These parameter variations result in process shifts, thus, requiring adequate control strategies to compensate for these alterations, which consequently maintain desired system response. A paradigm is the coupled tank systems; in such systems, the level and flow of liquid must be adequately controlled to maintain the reaction equilibrium as well as to avoid spillage or equipment damage. The model reference adaptive control (MRAC) is an adaptive control strategy that creates a control law, subject to an adaptation gain, which causes the system's plant to continuously track a reference model until a zero tracking error is achieved. The Massachusetts Institute of Technology (MIT) and Lyapunov approaches were used to develop the adaptation mechanism, which is used to adjust the parameters in the control law. Conventionally, a fixed value is adopted as the adaptation gain; however, the adaption gain can also be determined heuristically. The fuzzy logic control was used to optimally determine the value of the adaptation gain, which thus results in the fuzzy-optimized MRAC (FOMRAC) system. Consequently, these schemes were comparatively analysed for the control of the flow and level of liquid in coupled two-tank systems, arranged in noninteracting and interacting fashions. Using MATLAB/Simulink, results depicted that the FOMRAC systems had faster settling times in comparison with the fixed adaptation gain MRAC systems. Overall, the FOMRAC system based on Lyapunov rule yielded the lowest performance indices values. In addition, the scheme completely eliminated the overshoot that resulted from the implementation of the other schemes for the control of the interacting process.

1. INTRODUCTION

Process control (Coughanowr and LeBlanc 2009) is a branch of control engineering and chemical engineering that involves the implementation of industrial control systems or strategies to achieve its main objective which is to regulate the value of some quantity or parameter. Process control is utilized in various industries ranging from oil refining, petrochemicals, food processing, bottling, pulp and paper manufacturing, chemical manufacturing or processing, power generating, bio-technology, pharmaceuticals and so on.

One basic problem in the process industries is the control of the level and flow of liquid in multiple-tank systems (Atchaya 2017; Bhuvaneswari et al. 2012; Mamur et al. 2017; Nandhinipriyanka et al. 2018; Narayan and Srivastava 2013; Senthilkumar and Lincon 2012). Usually, liquid is pumped and stored into a tank and then pumped into a different tank(s) (Medewar et al. 2017). Such tanks are connected in series and can be arranged in an interacting or noninteracting manner. Taking a two-tank system as a case study, the liquid level of tank 2 has no effect on the liquid level of tank 1 in a noninteracting arrangement. On the other hand, the liquid levels of both tanks affect each other in an interacting setup. It is highly imperative that the level and flow of liquid in such tanks are regulated so as to maintain the reaction equilibrium and to avoid spillage or equipment damage (Damrudhar and Tanti 2016; Manohar et al. 2013).

There are different industrial control strategies which include: open-loop control, feed-forward control, closed-loop control, etc. In open-loop control, the system's output has no effect on the control action and is entirely

---

* **Corresponding Author**

*(zemidinak@gmail.com) ORCID ID 0000 – 0002 – 6098 – 043X
(poluseyi@unilag.edu.ng) ORCID ID 0000 – 0002 – 1164 – 7630

Cite this article

Dinakin D D & Oluseyi P O (2021). Fuzzy-Optimized model reference adaptive control of interacting and noninteracting processes based on MIT and Lyapunov rules. Turkish Journal of Engineering, 5(4), 141-153.

Research Article / DOI: XXXXXXXXXXXX

Received: 01/01/2020; Accepted: 23/06/2020

dependent on the input signal. The feed-forward control uses a process model to predict and reduce the impact/influence of measured disturbances on the plant/process. The feedback control involves introducing a feedback loop to a system, thus, creating a control action that enables the system to achieve a desired output response. The block diagram representation is shown in Fig. 1.

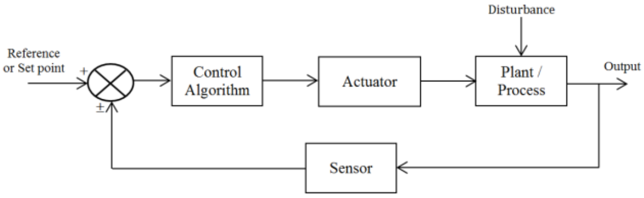

Figure 1. A typical industrial feedback control system

The proportional-integral-derivative (PID) controller is one of the widely used controllers in feedback control. Existing literature reveals numerous control techniques applied to coupled tank systems. In Changela and Kumar (2015); Fellani and Gabaj (2015); Parvat et al. (2015); Saju et al. (2014), the PID controller was used for liquid level control of various tank system setups using MATLAB software. Impressive results were recorded; however, it has been identified that adaptive control schemes are replacing the conventional control schemes because of the inadequacies experienced in coping with unanticipated disturbances or unpredictable faults (Stellet 2011). In other words, acting alone, the PID controller has a fixed gain thereby making it restricted in terms of adapting to external changes. Therefore, intelligent techniques, including meta-heuristic algorithms, have been used to tune the PID controller. Such include: particle swarm optimization (PSO-PID) (Medewar et al. 2017) internal model control (IMC-PID) (Lavanya et al. 2013; Senapati et al. 2018; Saju, et al. 2014; Jang 2017), approximate m-constant integral gain optimization (AMIGO-PID) (Senapati et al. 2018), Wiener model using Chidambaram technique (Saju, et al. 2014); Other control techniques used by other researchers include: the fuzzy logic control (FLC) (Changela and Kumar 2015; Parvat et al. 2015), PID-fuzzy (Senapati et al. 2018), model predictive control (Tijani et al. 2017), sliding mode control (SMC) (Ayten et al. 2018; Salunkhe, et al. 2015), back-stepping control strategy (John, et al. 2015), etc.

A feedback control system that adjusts its characteristics in a control environment so that some specified criteria are satisfied is known as an adaptive control system. Adaptive control systems are either model reference or self-tuning (Zhang 2010). The model reference adaptive control (MRAC) or model reference adaptive system (MRAS) tunes the controller parameters using a model of the plant (reference model). There are several approaches to tuning these parameters which include: the Massachusetts Institute of Technology (MIT) rule (Jain and Nigam 2013), Lyapunov rule (Nasar et al. 2015), etc.

The MIT rule is a gradient approach to the analysis and design of MRAC systems. It involves defining an error signal, which is the difference between the plant's output and the reference model's output. This error signal is used to tune the controller parameters by defining an objective function. The parameters of the controller are adjusted in the direction of the negative gradient of the objective function. It should be noted that the adaptive control loop of the MRAC system designed using the MIT rule has the tendency to be unstable. The Lyapunov approach, however, guarantees a stable adaptive control law. The Lyapunov approach is achieved using a Lyapunov function of both the output error or state error and the parameter error. The stability of the control loop is guaranteed if the derivative of the Lyapunov function is negative definite (Astrom and Wittenmark 1989; Dumont 2011).

The MIT and Lyapunov approaches are used to develop the adaptation mechanism which is used to adjust the parameters in the control law (Pankaj et al. 2011). This parameter adjustment results in a zero error and ensures system stability. The system performance is influenced by the adaptation gain from the adaptation mechanism (Stellet 2011; Swarnkar et al. 2011). A large value of adaptation gain can cause system instability. As seen in Stellet (2011), the MRAC system was used to control the liquid level in a coupled tank system and results were taken for different selected adaptation gains and compared with the result of implementing the PID controller. It was observed that for lower adaptation gains, the PID controller performed better than the MRAC whereas the MRAC performed better for slightly higher adaptation gain. This, thus, indicates that the adaptation gain must be optimally chosen to eliminate this poor performance. Usually, the adaptation gain is determined heuristically (Cheung 1996; Cheung et al. 1996; Keerth and Sathyanarayana 2012; Zadeh 1975). A heuristic approach adequate enough for determining the adaptation gain is the FLC. The FLC is a knowledge based algorithm which involves using linguistic variables to obtain optimal solution to a control problem (Zadeh 1975).

This study seeks to use the FLC to heuristically determine the adaptation gain of the MRAC systems for optimal performance. First, the coupled two-tank systems in noninteracting and interacting setups are modeled. The transfer function representations of both models are afterwards derived and then the MIT and Lyapunov approaches are used to design the MRAC systems for the control of both coupled two-tank systems. The performance of fuzzy-optimized model reference adaptive control (FOMRAC) systems based on both approaches is comparatively analyzed with the performance of the fixed adaptation gain MRAC systems using the following performance indices: integral square error (ISE), integral absolute error (IAE), integral time squared error (ITSE) and integral time absolute error (ITAE). The simulation is performed using MATLAB/Simulink.

The organization of the paper is as follows: Section 2 presents the mathematical models of the coupled tank systems and gives detailed description of the development of the control systems. Section 3 presents the investigations of the software implementation of the control techniques on the coupled tank systems using different performance indices. The paper is finally concluded in Section 4.

2. RESEARCH METHOD

Figure 2 shows the models of noninteracting and interacting coupled two-tank systems. The topology is a series arrangement. Liquid flows, first, into Tank 1 then into Tank 2. The outlet of each tank has a concentrated flow resistance dominated by a valve. The aim is to control the level of liquid in Tank 2. From Fig. 2, h_1 and h_2 are the heights (in m) of Tank 1 and Tank 2 respectively; q_0 is the volumetric flow of liquid (in m^3/s) into Tank 1 while q_1 and q_2 are the volumetric flow of liquid (in m^3/s) out of Tank 1 and Tank 2 respectively. The outlet of each tank has a concentrated flow resistance dominated by a valve. R_1 and R_2 are the resistances to flow of liquid (in s/m^2) out of Tank 1 and Tank 2 respectively. The cross-sectional areas (in m^2) of Tank 1 and Tank 2 respectively are denoted by A_1 and A_2.

Applying mass balance equation, the transfer function of the noninteracting coupled tank system [Fig. 2(a)] is given by Eq. (1):

$$\frac{h_2(s)}{q_0(s)} = \frac{R_2}{(\tau_1 s + 1)(\tau_2 s + 1)} \tag{1}$$

Similarly, applying mass balance equation and assuming linear resistance to flow, the transfer function of the interacting coupled tank system [Fig. 2(b)] is given by Eq. (2):

$$\frac{h_2(s)}{q_0(s)} = \frac{R_2}{\tau_1 \tau_2 s^2 + (\tau_1 + \tau_2 + A_1 R_2)s + 1} \tag{2}$$

The parameters used to model both coupled two-tank systems, extracted from Damrudhar and Tanti (2016); Fellani and Gabaj (2015) are shown in Table 1.

Table 1. Parameters used to model both coupled two-tank systems

Parameter	Value	Unit
A_1	0.025	m^2
A_2	0.025	m^2
R_1	100	s/m^2
R_2	200	s/m^2
h_1	0.3	m
h_2	0.15	m
τ_1	2.5	s
τ_2	5	s

Substituting the parameters in Table 1 in the expressions in Eq. (1) and Eq. (2), the transfer functions of the noninteracting and interacting coupled tank systems respectively are:

$$\frac{h_2(s)}{q_0(s)} = \frac{200}{(2.5s + 1)(5s + 1)} = \frac{200}{12.5s^2 + 7.5s + 1} \tag{3}$$

$$\frac{h_2(s)}{q_0(s)} = \frac{200}{12.5s^2 + (2.5 + 5 + 5)s + 1} = \frac{200}{12.5s^2 + 12.5s + 1} \tag{4}$$

The poles of Eq. (3) are located at −0.2 and −0.4 while the poles of Eq. (4) are located at −0.0877 and −0.9123. Comparing Eq. (3) and Eq. (4) with the standard form of second order systems in Eq. (5),

$$\frac{C(s)}{R(s)} = \frac{K{\omega_n}^2}{s^2 + 2\zeta\omega_n s + {\omega_n}^2} \tag{5}$$

Both systems have gains, K, of 200 and natural frequencies, ω_n, of 0.2828. The damping ratios of the noninteracting and interacting systems respectively are 1.0607 and 1.7678. A system with a damping ratio greater than one indicates an over-damped system. Over-damped systems approach a steady state more slowly than critically damped systems.

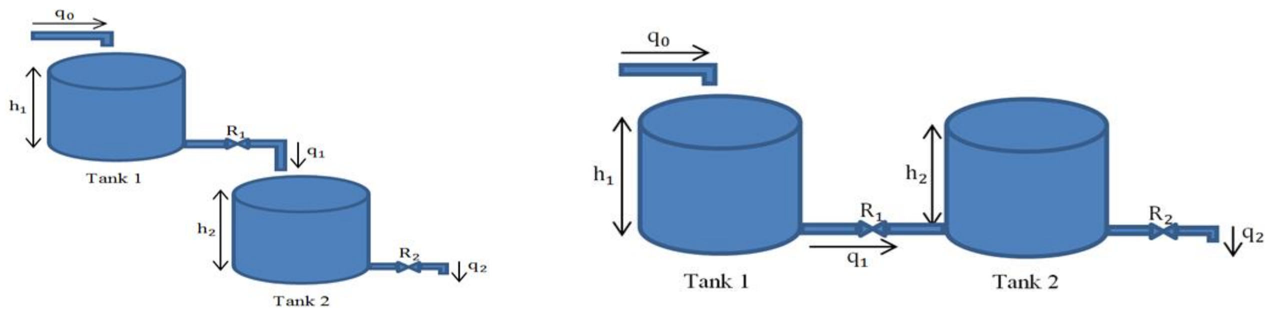

(a) noninteracting

(b) interacting

Figure 2. Coupled two-tank systems

2.1. Model Reference Adaptive Control (MRAC) System

The block diagram of a typical MRAC system is shown in Fig. 3. It consists of two loops; a feedback loop and a parameter adjustment loop. Where, u_c is the reference or set point, y_m, is the output of the reference model, y is the output of the plant while u is the input to the plant/process and is the control law, which is a function of the adaptation parameters. A reference model is used to tune the parameters of the controller thus, adjusting the control law which makes the plant/process track the output, y_m, of the reference model. There are a number of approaches that can be used to determine the adjustment mechanism or adaptation law of the MRAC system. Two of such are the MIT and Lyapunov approaches.

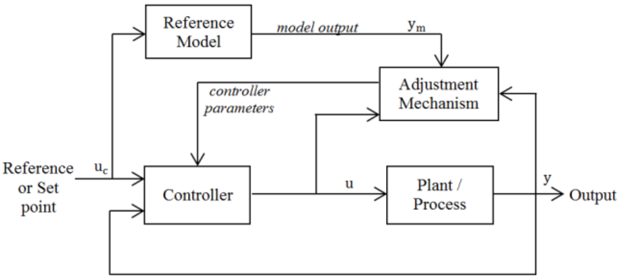

Figure 3. Block diagram of model reference adaptive control system

2.1.1. Lyapunov and MIT rules

Both coupled tank setups are second order systems as seen in Eq. (3) and Eq. (4). But first, the adaptation mechanism for a first order system using the Lyapunov rule is derived. The Lyapunov rule guarantees a stable adaptive control law. Considering a first order plant given by:

$$\frac{dy}{dt} = -ay + bu \tag{6}$$

A reference model is given by:

$$\frac{dy_m}{dt} = -a_m y_m + b_m u_c \tag{7}$$

The control law is given by:

$$u = \theta_1 u_c - \theta_2 y \tag{8}$$

The error function is the difference between the output of the plant, y, and the output of the reference model, y_m. This is expressed as:

$$e = y - y_m \tag{9}$$

By mathematical derivations, Eq. (10) is obtained,

$$\dot{e} = -a_m e - (b\theta_2 + a - a_m)y + (b\theta_1 - b_m)u_c \tag{10}$$

The Lyapunov approach requires a Lyapunov function; the function, V, must be positive definite while its derivative, $\dot{V}$, must be negative definite. It should be noted that there is no systematic way of finding a suitable Lyapunov function, V, (Astrom and Wittenmark 1989). Choosing the Lyapunov function:

$$V(e,\theta_1,\theta_2) = \frac{1}{2}\left(e^2 + \frac{1}{b\gamma}(b\theta_2 + a - a_m)^2 + \frac{1}{b\gamma}(b\theta_1 - b_m)^2\right) \tag{11}$$

Differentiating the Lyapunov function and substituting Eq. (10),

$$\dot{V} = -a_m e^2 + \frac{1}{\gamma}(b\theta_2 + a - a_m)(\dot{\theta}_2 - \gamma y e) + \frac{1}{\gamma}(b\theta_1 - b_m)(\dot{\theta}_1 + \gamma u_c e) \tag{12}$$

To ensure that $\dot{V}$ is negative definite,

$$\frac{1}{\gamma}(b\theta_2 + a - a_m)(\dot{\theta}_2 - \gamma y e) + \frac{1}{\gamma}(b\theta_1 - b_m)(\dot{\theta}_1 + \gamma u_c e) = 0 \tag{13}$$

Therefore, the adaptation laws using the Lyapunov approach are:

$$\frac{\partial\theta_1}{\partial t} = -\gamma u_c \tag{14}$$

$$\frac{\partial\theta_2}{\partial t} = \gamma y e \tag{15}$$

The MIT rule for a first order system is also derived. This is achieved using the error function in Eq. (10). Then, an objective function, J, is defined which is given by:

$$J(\theta) = \frac{1}{2}e^2 \tag{16}$$

$$\frac{\partial J}{\partial e} = e \tag{17}$$

The adaptation parameters are then adjusted in the direction of the negative gradient of the objective function, J. Therefore,

$$\frac{d\theta}{dt} = -\gamma\frac{\partial J}{\partial\theta} = -\gamma e\frac{\partial e}{\partial\theta} \tag{18}$$

Using the first order system, reference model and control law expressed by Eq. (6), Eq. (7) and Eq. (8) respectively. A perfect model means that $y = y_m$. Therefore,

$$\theta_1 = \frac{b_m}{b} \tag{19}$$

$$\theta_2 = \frac{a_m - a}{b} \tag{20}$$

From Eq. (18),

$$\frac{d\theta_1}{dt} = -\gamma e\frac{\partial e}{\partial\theta_1} \tag{21}$$

$$\frac{d\theta_2}{dt} = -\gamma e\frac{\partial e}{\partial\theta_2} \tag{22}$$

Substituting Eq. (8) in Eq. (6) and taking the Laplace transform,

$$y(s) = \frac{b\theta_1}{s + a + b\theta_2}u_c \tag{23}$$

Taking the Laplace transform of Eq. (7),

$$y_m(s) = \frac{b_m}{s + a_m}u_c \tag{24}$$

Substituting Eq. (23) and Eq. (24) in Eq. (9),

$$e(s) = \frac{b\theta_1}{s + a + b\theta_2}u_c - \frac{b_m}{s + a_m}u_c \tag{25}$$

$$\frac{\partial e}{\partial\theta_1} = \frac{b}{s + a + b\theta_2}u_c \tag{26}$$

Substituting Eq. (20),

$$\frac{\partial e}{\partial\theta_1} = \frac{b}{s + a_m}u_c \tag{27}$$

$$\frac{\partial e}{\partial \theta_2} = -\frac{b^2\theta_1}{(s+a+b\theta_2)^2}u_c \tag{28}$$

Substituting Eq. (23) and Eq. (20),

$$\frac{\partial e}{\partial \theta_2} = -\frac{b}{s+a_m}y \tag{29}$$

Substituting Eq. (27) and Eq. (29) in Eq. (21) and Eq. (22) respectively, the adaptation laws using the MIT rule are:

$$\frac{d\theta_1}{dt} = -\gamma' e\frac{b}{s+a_m}u_c \tag{30}$$

$$\frac{d\theta_2}{dt} = \gamma' e\frac{b}{s+a_m}y \tag{31}$$

Since the parameter, *b*, is unknown, it is absorbed using the equation: $\gamma = \gamma' b/a_m$. Equation (30) and Eq. (31) become Eq. (32) and Eq. (33) respectively.

$$\frac{d\theta_1}{dt} = -\gamma e\frac{a_m}{s+a_m}u_c \tag{32}$$

$$\frac{d\theta_2}{dt} = \gamma e\frac{a_m}{s+a_m}y \tag{33}$$

Comparing the adaptation laws obtained using the Lyapunov and MIT rules, it is observed that they are both identical except that the MIT rule introduces a filter which is equivalent to the transfer function of the reference model (Pankaj et al. 2011). Now, considering a second order system,

$$\ddot{y} = -a\dot{y} - by + bu \tag{34}$$

With a reference model,

$$\ddot{y}_m = -a_m\dot{y}_m - b_m y_m + b_m u_c \tag{35}$$

By following the procedure utilized above, the adaptation law for a second order system using the MIT rule is given by:

$$\frac{d\theta_1}{dt} = -\gamma e\frac{b_m}{s^2+a_m s+b_m}u_c \tag{36}$$

$$\frac{d\theta_2}{dt} = \gamma e\frac{b_m}{s^2+a_m s+b_m}y \tag{37}$$

Again, the adaptation laws for a second order system using MIT rule introduces a filter, which is the transfer function of the second order reference model. It can therefore be concluded that the adaptation laws, using the Lyapunov approach, for the first order system holds for the second order system. The adaptation gain, *γ*, determines the performance of the plant and is usually determined heuristically. This gain is determined using the FLC.

2.2. Fuzzy Logic Control (FLC)

Fuzzy logic control is a knowledge-based control strategy and it basically involves three stages which include: fuzzification, inference process and defuzzification (Amat et al. 2018; Dinakin and Oluseyi 2018; Mekhanet et al. 2016). The mapping of the input and output variables into membership functions is called fuzzification. The inference process involves formulating a mapping, by the utilization of a rule-base, from which decisions can be made (MATLAB 2016). It should be noted that there is no systematic tool for the formulation of the rule-base of the FLC (Reusch 1997). The final stage of the FLC is defuzzification and it involves converting the fuzzy output into a crisp or quantifiable value.

The error, *e*, which is the difference between the output of the plant and the output of the reference model, and the rate of change of error, *e'*, are taken as the fuzzy inputs while the adaptation gain, *γ* from the adaptation law is the fuzzy output. This is shown in Fig. 4.

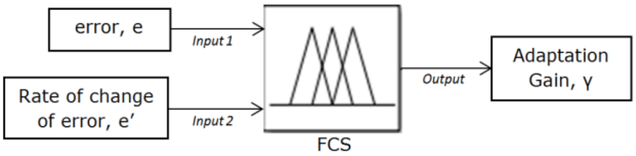

Figure 4. Input and output variables for fuzzy control system

The inputs, *e* and *e'*, are mapped, using equally spaced Gaussian membership functions (shown in Fig. 5), into the set {negative high (NH), negative medium (NM), negative low (NL), zero (ZE), positive low (PL), positive medium (PM), positive high (PH)} while the output, γ is mapped into the set {zero (Z), low (L), medium (M), high (H)}.

The rule-base is made up of IF-THEN rules which relate the inputs with the output. The rules used to determine the adaptation gain of the adaptation law/mechanism are shown in Table 2. For instance, if error is NH and rate of change of error is NH, then the adaptation gain is H. If error is PL and rate of change of error is PM, then the adaptation gain is M. If error is ZE and rate of change of error is ZE, then the adaptation gain is Z, and so on.

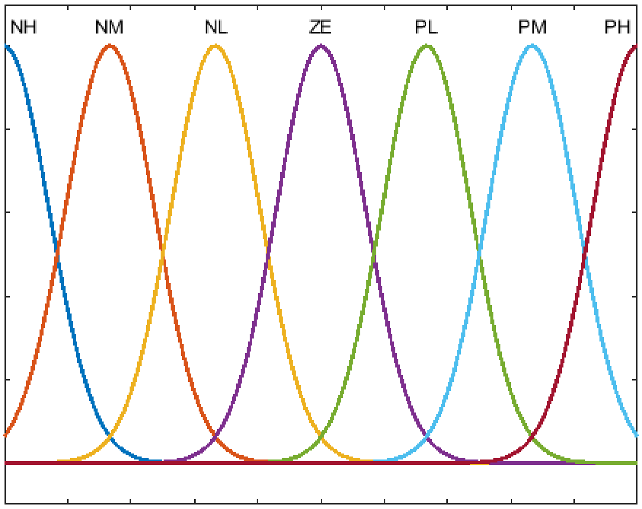

Figure 5. Gaussian membership function

The rules in Table 2 create a 3D surface plot as shown in Fig. 6.

The plant parameters of the MRAC system are obtained from Eq. (3) and Eq. (4) and shown in Table 3.

Table 2. Rules relating the inputs with the output

e′ \ e	NH	NM	NL	ZE	PL	PM	PH
NH	H	H	M	M	L	Z	Z
NM	H	M	M	L	L	Z	Z
NL	M	M	L	L	Z	Z	L
ZE	M	L	L	Z	L	L	M
PL	L	Z	Z	L	L	M	M
PM	Z	Z	L	L	M	M	H
PH	Z	Z	L	M	M	H	H

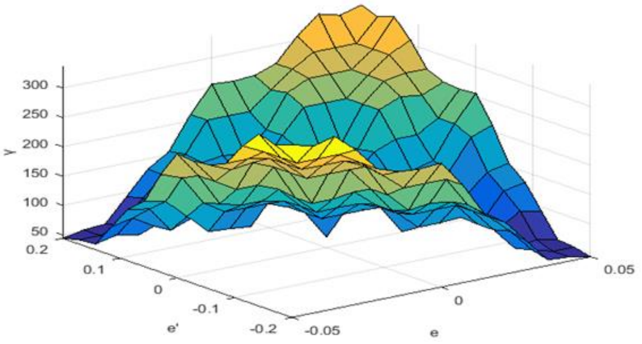

Figure 6. 3D rules' surface plot

Table 3. Plant parameters of the MRAC system

System	Parameter	Value
Noninteracting	a	0.6
	b	0.08
Interacting	a	1
	b	0.08

It has already been established that both systems are over-damped systems. Therefore, a critically damped model is chosen so that the plants continuously track the model. Critically damped systems have repeated poles and a damping ratio of one. The model parameters are chosen and shown in Table 4.

Table 4. Model parameters of the MRAC system

System	Parameter	Value
Noninteracting	a_m	0.8
	b_m	0.16
Interacting	a_m	2
	b_m	1

From Table 4, the transfer functions of the reference models of the noninteracting and interacting systems respectively are:

$$\frac{y_m(s)}{u_c(s)} = \frac{1}{6.25s^2 + 5s + 1} \tag{38}$$

$$\frac{y_m(s)}{u_c(s)} = \frac{1}{s^2 + 2s + 1} \tag{39}$$

This indicates that the models have repeated poles at -0.4 for the noninteracting system and at -1 for the interacting system. Fig. 7 shows the block diagrams representations of the overall transfer function of the MRAC systems of both the noninteracting and interacting coupled two-tank systems. The adaptation mechanisms for the noninteracting tank system using the MIT and Lyapunov rules are shown in Fig. 8.

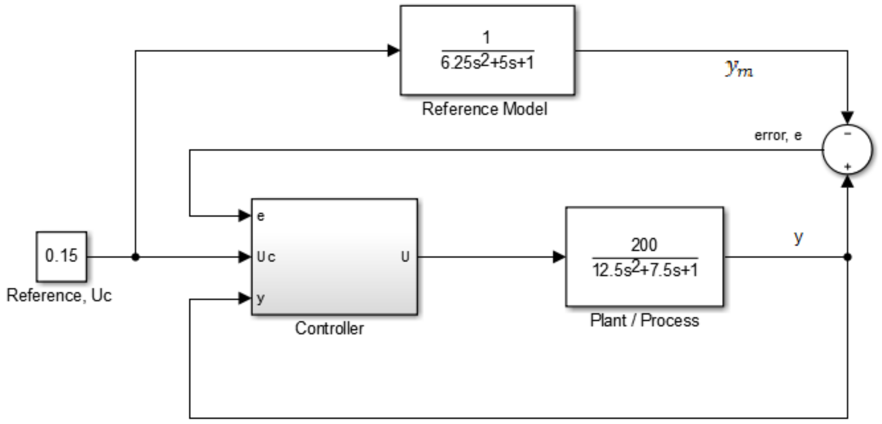

(a) noninteracting

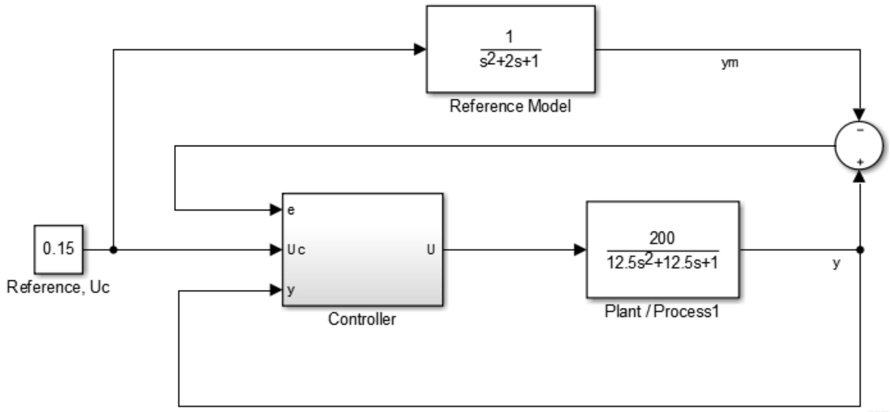

(b) interacting

Figure 7. Block diagram representation of the overall transfer function of the MRAC systems

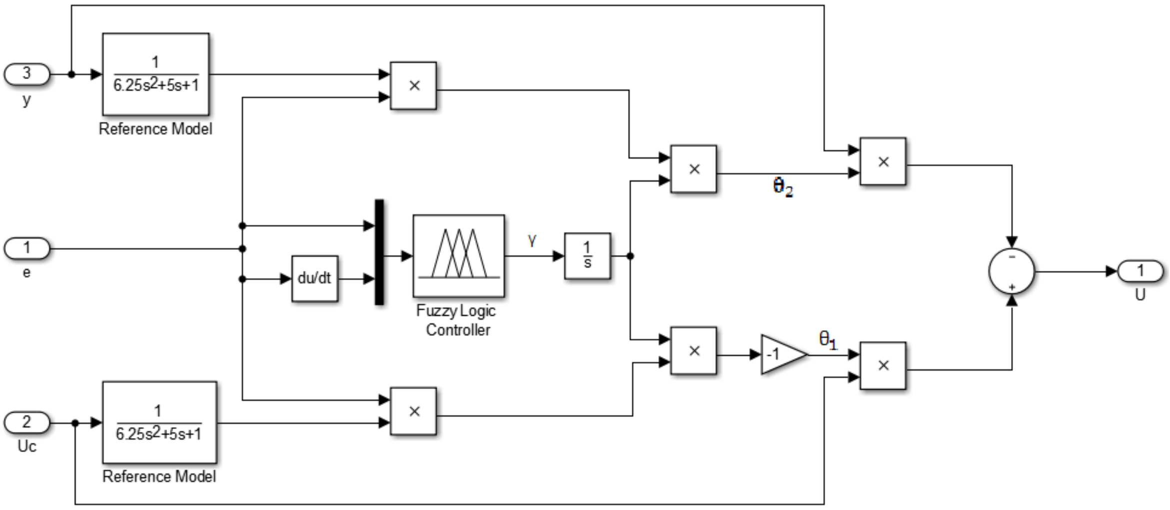

(a) MIT

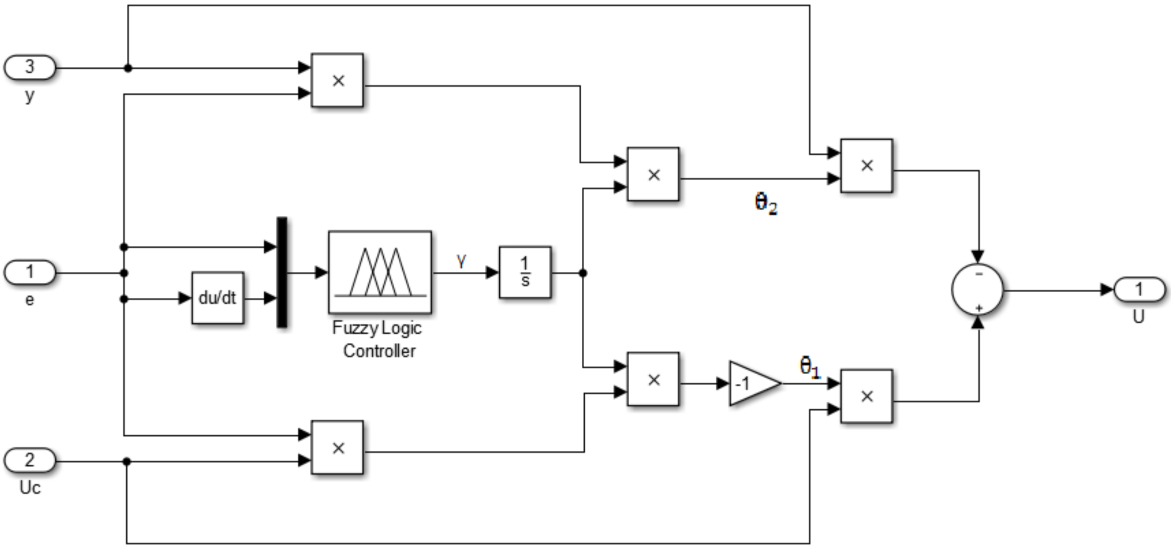

(b) Lyapunov

Figure 8. Adaptation mechanism fort he noninteracting tank systems

2.3 Performance Analysis

The performance of the FOMRAC systems designed using the MIT and Lyapunov approaches is compared with the performance of conventional fixed adaptation gain MRAC systems. The maximum adaptation gain value used in the design of the FLC is 400; hence, this value is used as the adaptation gain for the fixed adaption gain MRAC systems. The following performance indices are used for the comparative analysis of each controller: ISE, IAE, ITAE and ITSE. The formulas for the ISE, IAE, ITAE and ITSE respectively are given as follows:

$$\mathrm{ISE} = \int_0^t e(t)^2\,dt \tag{40}$$

$$\mathrm{IAE} = \int_0^t |e(t)|\,dt \tag{41}$$

$$\mathrm{ITSE} = \int_0^t te(t)^2\,dt \tag{42}$$

$$\mathrm{ITAE} = \int_0^t t|e(t)|\,dt \tag{43}$$

3. RESULTS AND DISCUSSION

Simulation is done using MATLAB/Simulink. The noninteracting and interacting coupled two-tank system is simulated with the designed controllers. The simulation is done for a period of 30 seconds. The set point which is the value of height, h_2, is 0.15m. Simulation is done first for the fixed adaptation gain MRAC controllers. The fuzzy logic controller is then used to optimize the adaptation gain. As the adaptation gain changes, the adaptation parameters (θ_1 and θ_2) also change.

Figures 9 and 10 show the variations in the adaptation parameters for the MRAC systems with a fixed adaptation gain of 400 and for the FOMRAC systems respectively, based on the MIT rule.

For the fixed adaptation gain MRAC systems, it can be seen that the adaptation parameters converge to constant values of $+2.5002\mathrm{E}-3$ and $-2.4939\mathrm{E}-3$ for θ_1 and θ_2 respectively for the noninteracting tank system and constant values of $+2.5002\mathrm{E}-3$ and $-2.4942\mathrm{E}-3$ for θ_1 and θ_2 respectively for the interacting tank system. Likewise, for the FOMRAC systems, the adaptation parameters converge to constant values of $+2.4988\mathrm{E}-3$ and $-2.4988\mathrm{E}-3$ for θ_1 and θ_2 respectively for the noninteracting tank system and constant values of $2.5E-3$ and $-2.5E-3$ for θ_1 and θ_2 respectively for the interacting tank system.

Figures 11 and 12 show the variations in adaptation parameters for the noninteracting and interacting systems based on the Lyapunov rule for the fixed adaptation gain systems and FOMRAC systems respectively. The adaptation parameters also converge to constant values. For the fixed adaptation gain systems, θ_1 and θ_2 converge to $2.4997E-3$ and $-2.4924E-3$ respectively for the noninteracting tank system and values of $2.5003E-2$ and $-2.4935E-2$respectively for the interacting tank system. For the FOMRAC systems, θ_1 and θ_2 converge to $2.5416E-3$ and $-2.5416E-3$ respectively for the noninteracting tank system and values of $2.5588E-3$ and $-2.5588E-3$ respectively for the interacting tank system.

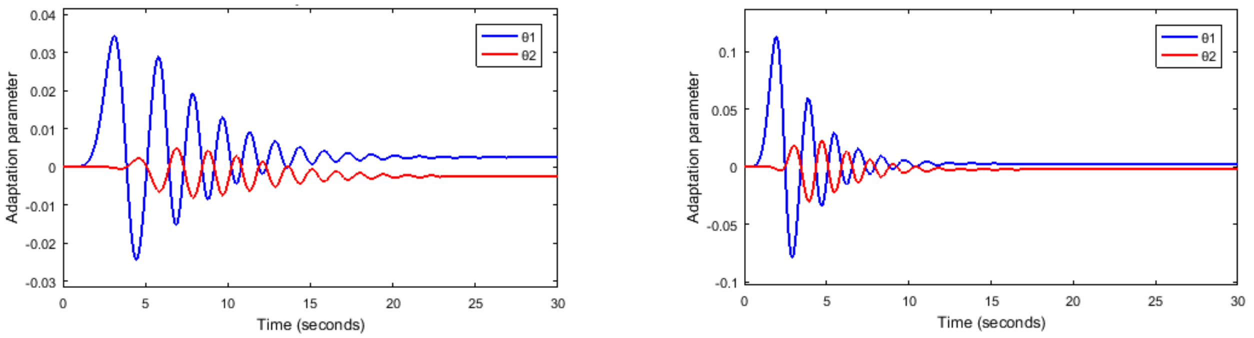

(a) noninteracting (b) interacting

Figure 9. Variations in adaptation parameters of the fixed adaptation gain MRAC systems based on MIT rule

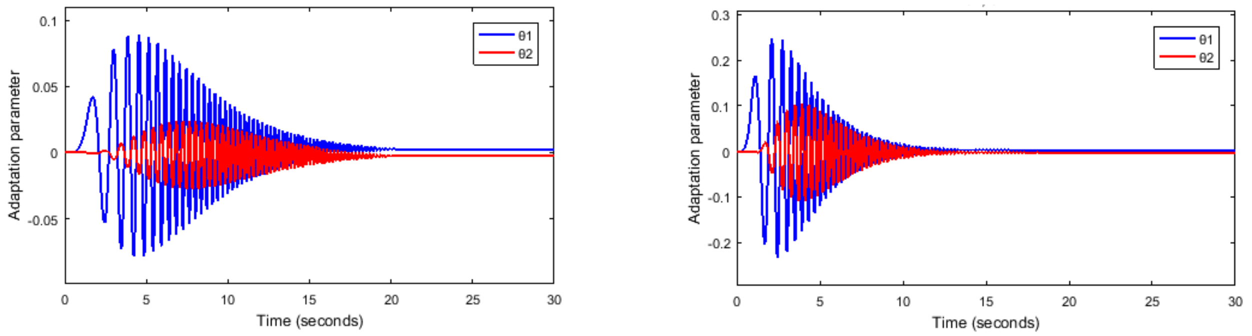

(a) noninteracting (b) interacting

Figure 10. Variations in adaptation parameters of the FOMRAC systems based on MIT rule

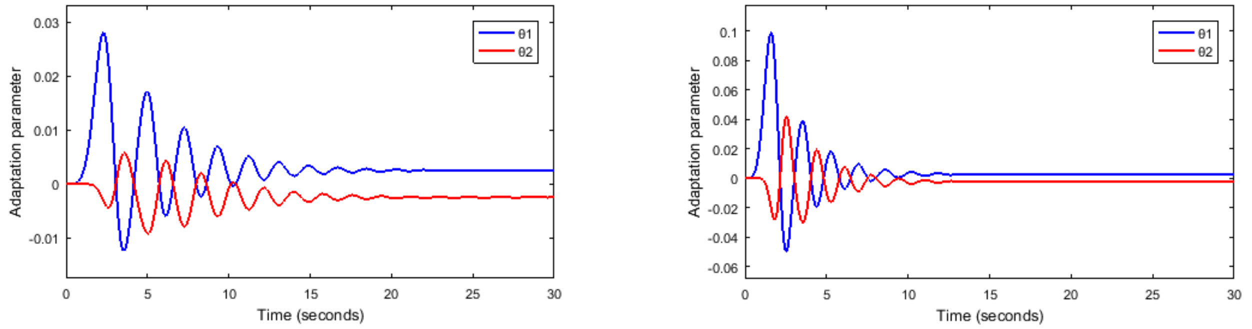

(a) noninteracting (b) interacting

Figure 11. Variations in adaptation parameters of the fixed adaptation gain MRAC systems based on Lyapunov rule

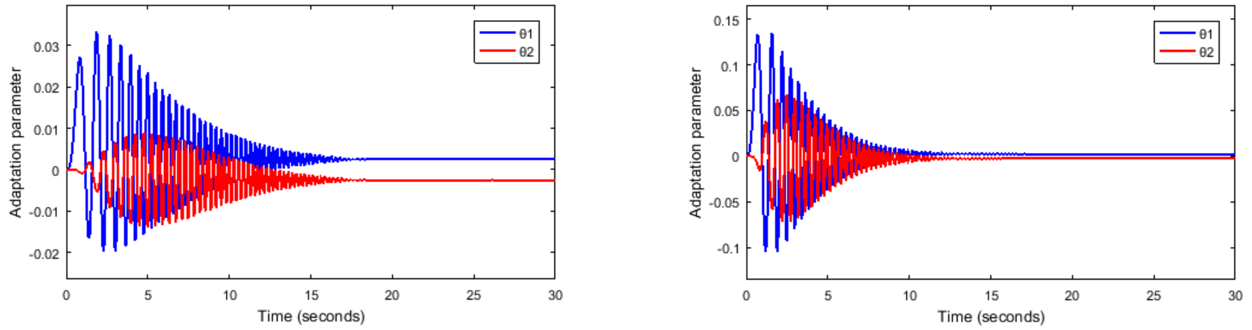

(a) noninteracting (b) interacting

Figure 12. Variations in adaptation parameters of the FOMRAC systems based on Lyapunov rule

For MRAC, the control law is subject to a control parameter, u, which is a function of the adaptation parameters. The variation of the control parameters with time for the fixed adaptation gain MRAC systems and the FOMRAC systems respectively are shown in Figs. 13 and 14 respectively. It is also seen that, for the fixed adaptation gain MRAC system [Fig 13(a)], both control parameters converge to constant values; $7.4819E-4$ using the MIT rule and $7.4773E-4$ using Lyapunov rule. Likewise, for the FOMRAC system [Fig 14(a)]; $7.5E-4$ using the MIT rule and $7.3409E-4$ using the Lyapunov rule. The control parameters of the fixed adaptation gain system shown in Fig 13(b) and the FOMRAC system shown in Fig 14(b) converge to constant values of $7.4826-4$ (MIT rule) and $7.4806E-4$ (Lyapunov rule) and converge to constant values of $7.5011E-4$ (MIT rule) and $7.5141E-4$ (Lyapunov rule).

The control parameters are used to improve the plant parameters, a and b, so that the plant adequately tracks the reference model. Using the fixed adaptation gain MRAC and FOMRAC systems based on the MIT and Lyapunov rules, Figs. 15 - 18 show the response characteristics for the plants and reference models of the noninteracting and interacting tank systems. It is observed that the plant adequately tracks the reference model in all systems.

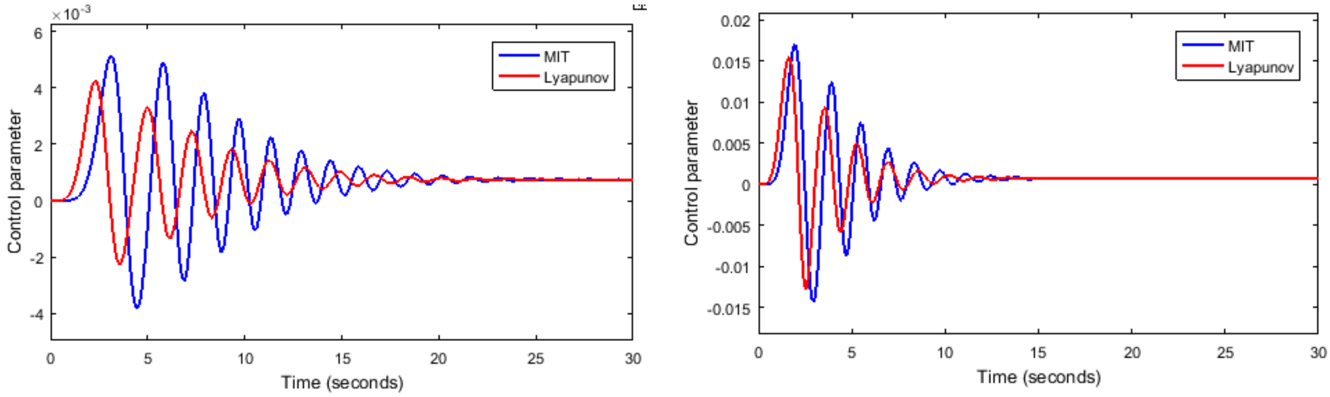

(a) noninteracting (b) interacting

Figure 13. Variations in control parameters of the fixed adaptation gain MRAC systems

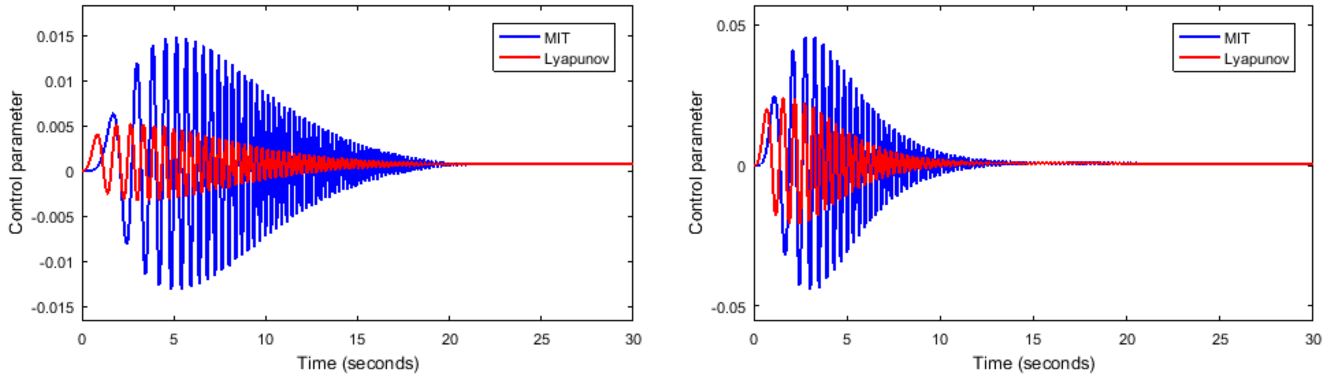

(a) noninteracting (b) interacting

Figure 14. Variations in control parameters of the FOMRAC systems

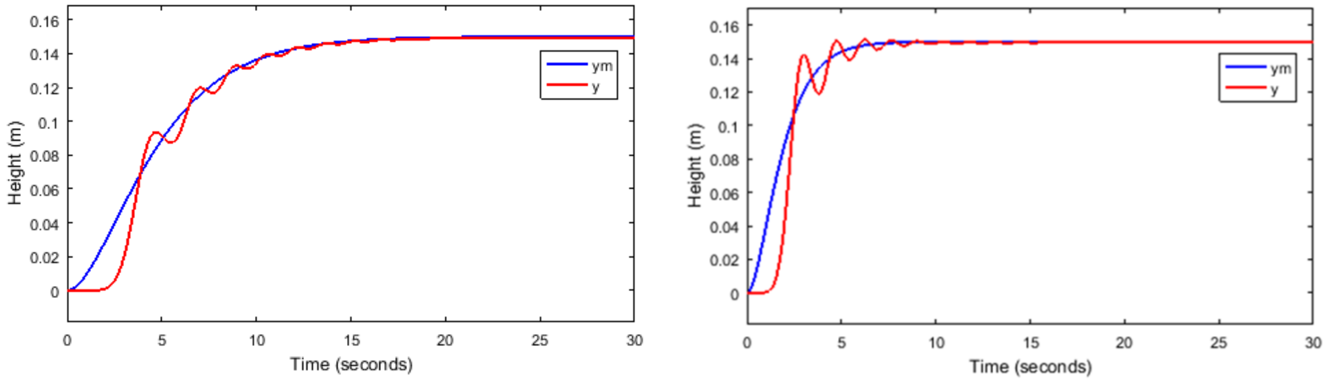

(a) noninteracting (b) interacting

Figure 15. Response characteristics for the reference model and plant of the fixed adaptation gain MRAC systems based on MIT rule

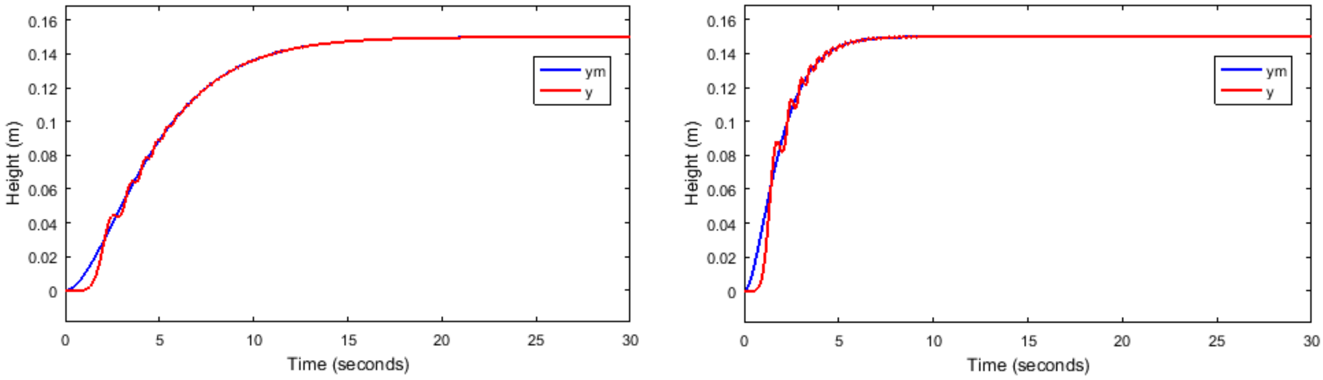

(a) noninteracting (b) interacting

Figure 16. Response characteristics for the reference model and plant of the FOMRAC systems based on MIT rule

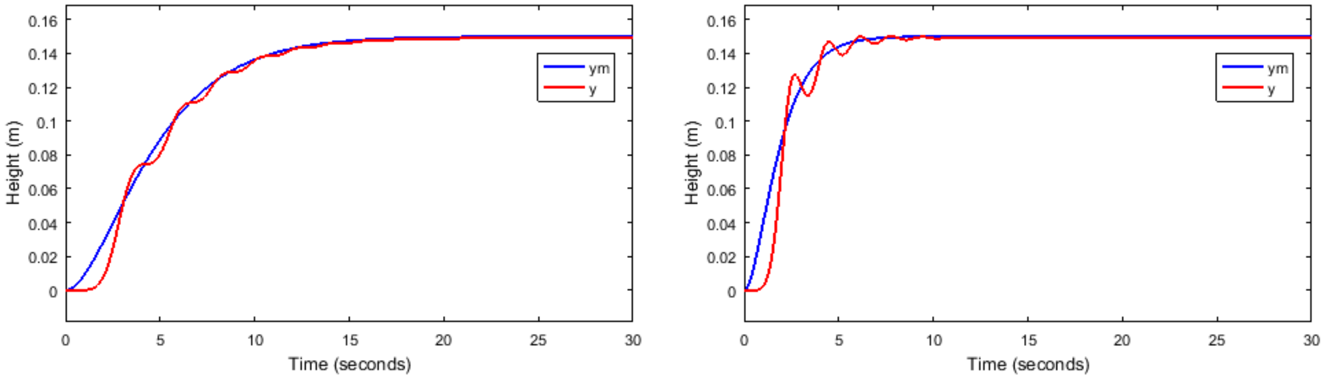

(a) noninteracting (b) interacting

Figure 17. Response characteristics for the reference model and plant of the fixed adaptation gain MRAC systems based on Lyapunov rule

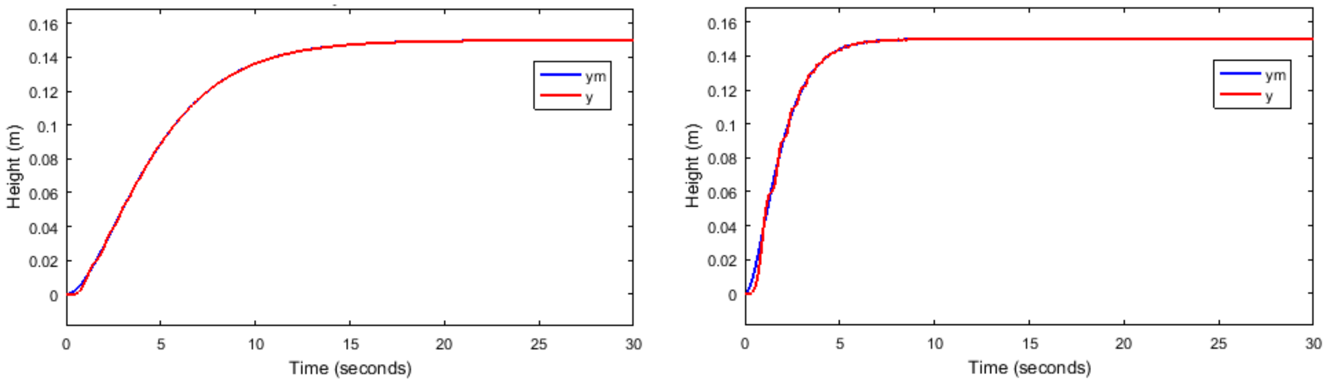

(a) noninteracting (b) interacting

Figure 18. Response characteristics for the reference model and plant of the FOMRAC systems based on Lyapunov rule

As the plants track the reference models, the error is reduced to zero. The error plots of the systems for the fixed adaptation gain MRAC and FOMRAC systems based on the MIT and Lyapunov rules are shown in Fig. 19. The performance indices: ISE, IAE, ITAE and ITSE are used for comparative analysis based on the error plots of the controllers. This is shown in Table 7. It is seen that the FOMRAC system based on the Lyapunov rule obtained the least fitness values.

The output/response curves for a set point (h_2) of 0.15m of all four control schemes for the noninteracting and interacting tank systems are shown in Fig. 20. It is observed from the plot characteristics shown in Table 8 that the fixed adaptation gain MRAC systems and FOMRAC scheme exhibit zero overshoot for the noninteracting tank system. On the other hand, the FOMRAC scheme based on Lyapunov rule completely eliminates the slight overshoot that resulted from the implementation of the other three control schemes for the interacting tank system. In comparison to the fixed adaptation gain MRAC systems, the FOMRAC systems have better steady state errors. Furthermore, the FOMRAC scheme based on Lyapunov rule has the fastest settling time for both the noninteracting and interacting tank systems.

Finally, it is common knowledge that adaptive controllers prevail under changing model parameters. Hence, to establish that the controllers can adequately deal with parameter variations or disturbances, all controllers are simulated for a unit ramp reference input and the result is shown in Fig. 21. It is seen that all four controllers adequately track the reference input.

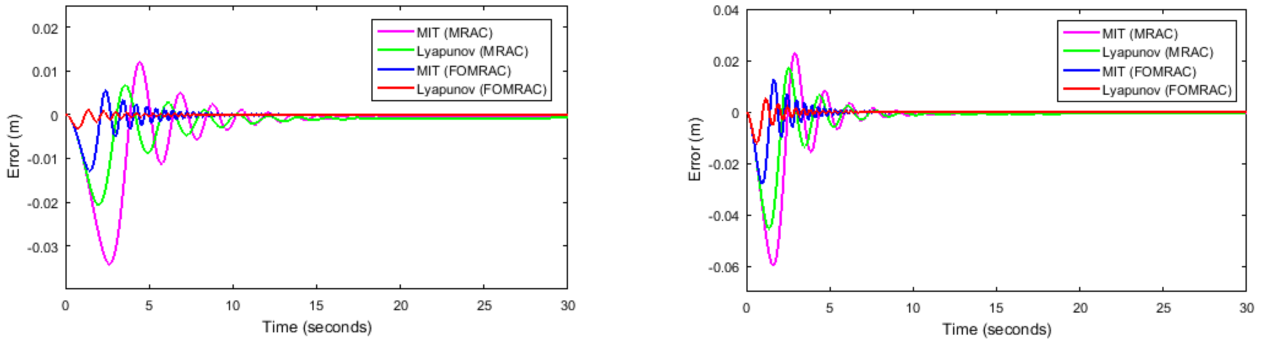

(a) noninteracting (b) interacting

Figure 19. Error plots for the fixed adaptation gain MRAC systems and the FOMRAC systems

Table 7. Performance indices of each control type for both coupled tank systems

System	Control Type	Objective Functions			
		ISE	IAE	ITAE	ITSE
Noninteracting	MIT (MRAC)	1.968E − 3	1.100E − 1	5.743E − 1	5.633E − 3
	Lyapunov (MRAC)	6.347E − 4	7.164E − 2	5.126E − 1	1.813E − 3
	MIT (FOMRAC)	1.566E − 4	2.396E − 2	6.762E − 2	2.628E − 4
	Lyapunov (FOMRAC)	6.490E − 6	4.898E − 3	1.610E − 2	8.021E − 6
Interacting	MIT (MRAC)	4.030E − 3	1.262E − 1	4.741E − 1	7.022E − 3
	Lyapunov (MRAC)	2.101E − 3	9.656E − 2	4.572E − 1	3.413E − 3
	MIT (FOMRAC)	5.199E − 4	3.533E − 2	6.485E − 2	5.671E − 4
	Lyapunov (FOMRAC)	7.529E − 5	1.322E − 2	2.575E − 2	6.442E − 5

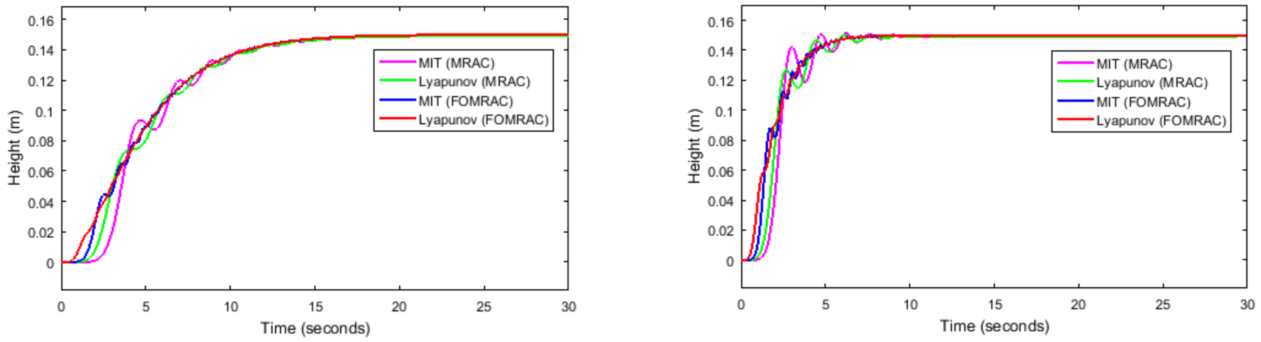

(a) noninteracting (b) interacting

Figure 20. Response plots for a set point of 0.15m

Table 8. Plot characteristics of the response plots for a set point of 0.15m

System	Control Type	Objective Functions			
		Rise Time (s)	Percentage Overshoot (%)	Steady State Error (m)	Settling Time (s)
Noninteracting	MIT (MRAC)	7.1491	0	−5.1644E − 4	14.7653
	Lyapunov (MRAC)	7.5781	0	−7.2903E − 4	15.0728
	MIT (FOMRAC)	7.8797	0	−1.9823E − 5	14.6085
	Lyapunov (FOMRAC)	8.4349	0	−2.0624E − 5	14.5798
Interacting	MIT (MRAC)	1.1062	1.2648	−4.8290E − 4	7.1279
	Lyapunov (MRAC)	2.6083	0.4622	−6.0940E − 4	7.0991
	MIT (FOMRAC)	2.7983	0.0121	−7.5632E − 6	6.1365
	Lyapunov (FOMRAC)	3.0678	0	−8.1561E − 6	5.8708

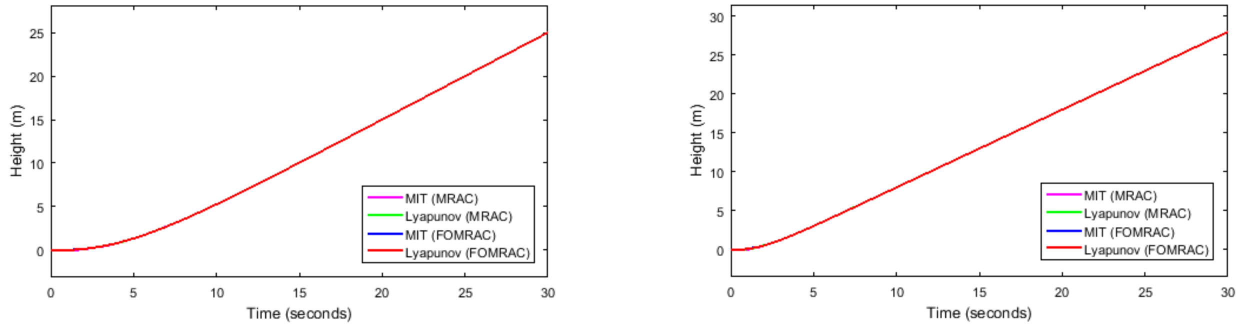

(a) noninteracting (b) interacting

Figure 21. Response plots for a unit ramp input

4. CONCLUSION

MRAC has proven to be adequately capable of handling systems with constant parameter changes as visibly portrayed in the results. The performance of the fuzzy-optimized MRAC systems based on the MIT and Lyapunov rules were compared with the performance of conventional fixed adaptation gain MRAC systems, for the control of the level and flow of liquid in coupled two-tank systems arranged in noninteracting and interacting setups. In both tank setups, it was observed that there were longer settling times when the fixed adaptation gain MRAC systems were adopted as opposed to the FOMRAC systems. Specifically, the FOMRAC system based on Lyapunov rule eliminated the resulting overshoot from the implementation of the other three schemes for the control of interacting processes. Also, the FOMRAC scheme based on Lyapunov rule had the least objective function values, thus, making it the ideal control strategy for noninteracting and interacting processes.

ACKNOWLEDGEMENT

The authors sincerely appreciate the National Information Technology Development Agency (NITDA) for the research grant provided to carry out this work through the National Information Technology Development Fund (NITDEF). Ref: NITDA/HQ/DG/135/2005/VOL.2.

REFERENCES

Amat M A H C, Naim S & Zakaria S (2018). Fuzzy logic approach to identify deprivation index in Peninsular Malaysia. Bulletin of Electrical Engineering and Informatics, 7(4), 601-608. DOI: 10.11591/eei.v7i4.1352

Astrom K J & Wittenmark B (1989). Adaptive Control, Addison-Wesley, USA.

Atchaya, G. (2017). "Review of linear and non-linear liquid level control system." Journal of Innovative Science & Engineering Research, 2(2), pp. 3-7.

Ayten K K, Dumlu A & Kaleli A (2018). Real-time implementation of self-tuning regulator control technique for coupled tank industrial process system. Proceedings of the Institution of Mechanical Engineers, Part I: Journal of Systems and Control Engineering, 1-14. DOI: 10.1177/0959651818773179

Bhuvaneswari N S, Praveena R & Divya R (2012). System identification and modeling for interacting and non-interacting tank systems using intelligent techniques. arXiv preprint, arXiv: 1208.1103.

Changela M & Kumar A (2015). Designing a controller for two tank interacting system. International Journal of Science and Research (IJSR), 4(5), 589-593.

Cheung J Y M (1996). A fuzzy logic model reference adaptive controller. IEE Colloquium on Adaptive Controllers in practice, pp. 1-6.

Cheung J Y M, Cheng K W E & Kamal A S (1996). Motor speed control by using a fuzzy logic model reference adaptive controller. 6th International Conference on Power Electronics and Variable Speed Drives, 430-435.

Coughanowr D R & LeBlanc S E (2009). Process systems analysis and control, McGraw-Hill, New York, USA. ISBN: 978–0–07–339789–4

Damrudhar O and Tanti D K (2016). Comparative performance analysis for two tanks liquid level control system with various controllers using MATLAB. International Journal of Latest Trends in Engineering and Technology (IJLTET), 7(2), 345-352. DOI:10.21172/1.72.555

Dinakin D D & Oluseyi P O (2018). Optimal under-frequency load curtailment via continuous load control in a single area power system using fuzzy logic, PID-fuzzy and neuro-fuzzy (ANFIS) controllers. Jordan Journal of Electrical Engineering (JJEE), 4(4), 208-223.

Dumont G (2011). EECE 574 – Adaptive Control, Lecture notes – Model Reference Adaptive Control.

Fellani M A & Gabaj A M (2015). PID controller design for two tanks liquid level control system using MATLAB. International Journal of Electrical and Computer Engineering (IJECE), 5(3), 436-442.

Jain P & Nigam M J (2013). Design of a model reference adaptive controller using modified MIT rule for a second order system. Advance in Electronic and Electric Engineering, 3(4), 477-484.

Jang L K (2017). Feedback control for liquid level in a gravity-drained multi-tank system. Chemical Engineering & Process Techniques, 3(1), 1-10.

John J A, Jaffar N E & Francis R M (2015). Modeling and control of coupled tank liquid level system using backstepping method. International Journal of Engineering Research & Technology (IJERT), 4(6), 667-671.

Keerth K & Sathyanarayana M S (2012). Fuzzy implementation of model reference adaptive control of DC drives. International Journal of Engineering Science and Advanced Technology (IJESAT), 2(3), 605-611.

Lavanya M, Aravind P, Valluvan M & Caroline B E (2013). Model based control for interacting and non-interacting level process using labview. International Journal Advanced Research in Electrical, Electronics and Instrumentation Engineering, 2(7), 3174-3179.

Mamur H, Atacak I, Korkmaz F & Bhuiyan M R A (2017). Modeling and application of a computer-controlled liquid level tank system. Computer science & Information Technology (CS & IT), pp. 97-106.

Manohar G, Elakkiya V, Stanley P & Sudha R (2013). Neural network based level control in two tank conical interacting system. 7th International Conference on Intelligent Systems and Control (ISCO), 194-196.

MATLAB (2016). Natick, Massachusetts: The MathWorks, Inc., version 9.0.0.341360.

Medewar P G, Sonawane R R & Munje R K (2017). Two tank non-interacting liquid level control comparison using fuzzy and PSO controller. National Conference on Emerging Trends in Engineering & Technology (NCETET17), IOSR Journal of Electrical and Electronics Engineering (IOSR-JEEE), 1(5), 24-31.

Mekhanet M, Mokrani L, Ameur A & Attia Y (2016). Adaptive fuzzy gain of power system stabilizer to improve the global stability. Bulletin of Electrical Engineering and Informatics, 5(4), 421-429. DOI: 10.11591/eei.v5i4.576

Nandhinipriyanka G, Ishwarya S, Janakiraman S, Thana C S & Vaishali P (2018). Design of model reference adaptive controller for cylinder tank system. International Journal of Pure and Applied Mathematics, 118(20), 2007-2013.

Narayan Y & Srivastava S (2013). Response of flow rate of non-interacting tanks using NCS and fuzzy controller. 2013 International Conference on Emerging Trends in Communication, Control, Signal Processing & Computing (C2SPCA), 1-4.

Nasar A, Jaffar N E & Kochummen S A (2015). Lyapunov rule based model reference adaptive controller designs for steam turbine speed. International Journal of Electrical Engineering & Technology (IJEET), 6(7), 13-22.

Pankaj S, Kumar J S & Nema R K (2011). Comparative analysis of MIT rule and Lyapunov rule in model reference adaptive control scheme. Innovative Systems Design and Engineering, 2(4), 154-162.

Parvat B J, Deo S A & Kadu C B (2015). Mathematical modeling of interacting and non interacting system. International Journal of Application or Innovation in Engineering & Management (IJAIEM), 4(1), 86-92.

Reusch B (1997). Computational Intelligence Theory and Applications. Proceedings of International Conference, 5th Fuzzy Days, Dortmund, Germany, Springer. ISBN: 978-3-540-69031-3

Saju S, Revathi R & Suganya K P (2014). Modeling and control of liquid level non-linear interacting and non-interacting system. International Journal of Advanced Research in Electrical, Electronics and Instrumentation Engineering, 3(3), 8003-8013.

Salunkhe S M, Kurode S R & Bhole V B (2015). Robust control of liquid level in coupled tank system using smooth first order sliding modes. 2015 International Conference on Industrial Instrumentation and Control (ICIC), pp. 1647-1650.

Senapati A, Maitra N, Batabyal S & Kashyap A K (2018). Control and performance analysis of three tank flow control system using linear & non-linear controller. International Journal of Innovative Research in Computer and Comunication Engineering, 6(1), 329-340. DOI: 10.15680/IJIRCCE.2018. 0601057

Senthilkumar M & Lincon S A (2012). Design of stabilizing PI controller for coupled tank MIMO process. International Journal of Engineering Research and Development, 3(10), 47-55.

Stellet J E (2011). Influence of adaptation gain and reference model parameters on system performance for model reference adaptive control. International Scholarly and Scientific Research & Innovation, 5(12), 1660-1665.

Swarnkar P, Jain S & Nema R K (2011). Effect of adaptation gain in model reference adaptive controlled second order system. Engineering, Technoloy & Applied Science Research, 1(3), 70-75.

Tijani A S, Shehu M A, Alsabari A M, Sambo Y A & Tanko N L (2017). Performance analysis for coupled-tank system liquid level control using MPC, PI, PI-plus-feedforward control scheme. Journal of Robotics and Automation, 1(1), 42-53.

Zhang P (2010). Advanced Industrial Control Technology, William Andrew, New York, USA. ISBN-13:978-1-4377-7807-6

Zadeh L A (1975). The concept of a linguistic variable and its application to approximate reasoning – I. Information Sciences, 8, 199-249. DOI: 10.1016/0020-0255(75)90036-5

Turkish Journal of Engineering

https://dergipark.org.tr/en/pub/tuje

e-ISSN 2587-1366

Strength and behaviour assessment of axially loaded concrete filled steel tubular stub columns

Samoel M. Salih [1], **Ihsan Al-abboodi** *[1]

[1]*University of Basrah, College of Engineering, Department of Civil Engineering, Basrah, Iraq*

Keywords
Stub columns
CFST
3D Analysis
ABAQUS

ABSTRACT

As a result of the excellent performance under different loading conditions, concrete-filled steel tubular (CFST) stub columns are extensively used recently. The current study employs a 3D finite element analysis to assess the response of (CFST) stub columns when subjected to axial compression. The effect of some parameters of concrete and the confining steel tube where numerically investigated. The steel was considered as an elastic perfectly plastic material, whereas a damage plasticity behaviour was adopted for the concrete material. Analysis results suggested that the ultimate strength of concrete increases with the increase of its grade. On the other hand, increasing magnitudes of concrete grade caused a reduction in the ductility of the composite columns. Also, the increase in the steel yields stress, and the steel tube wall thickness contributes to an increase in the columns' ultimate strength. However, they reduce the action of the concrete grade that increases the column's ultimate strength. It was also noted that the ductility that the circular CFST stub columns showed is larger than that for square columns. Thus, the use of square CFST columns with high strength concrete, especially in seismically active areas, should be carefully considered.

1. INTRODUCTION

The structural advantages and superior response of the concrete filled steel tubular (CFST) columns qualifies them as one of the essential elements in modern structural construction. The interaction of their components contributes to the resistance of applied loads. The confinement pressure of the steel tube makes the concrete core behaves like a material with a triaxial stress state. Meanwhile, the concrete core itself plays a role in eliminating or mitigating the local buckling that may occur in the steel tube. This interaction behaviour means that CFST columns have demonstrated greater strength against axial compression, a higher energy absorption capacity, a better ductility performance, and lower strength degradation than steel hollow sections and reinforced concrete columns if they used separately. Researchers have experimentally and analytically studied the response of of CFST columns under different loading conditions. These studies have provided an extensive database for several design codes in order to develop their design approaches and practices for composite columns, such as those specified in the Eurocode 4, AISC specification, and ACI code. Due to its ability in simulating different structural element, Finite Element Analysis (FEA) can be considered as an effective tool in modelling the CFST columns. However, the accuracy of the FEA is more impacted by the selection of the material modelling for both steel and concrete compared with the other input parameters (Mallesh et al. 2016). Therefore, different material models were developed in previous studies to improve the prediction accuracy of the FEA. Han et al. (2007) suggested a procedure for the numerical modelling of CFST columns subjected to pure torsion. The analysis was conducted by modelling the concrete material as a damaged plasticity model. An elastic perfect plastic model was adopted to define the response of steel material. They developed formulae to predict the ultimate torsional capacity of such composite columns. Deng et al. (2013) theoretically and numerically investigated the flexural behaviour of CFST composite members using FEA. ANSYS software was adopted for a finite element modelling of the problem. Both theoretical and numerical approaches were validated against published experimental studies. They showed that both analysis procedures have the ability to predict the behavioural stages of CFST members, with more accurate results showed by

---

* **Corresponding Author**

(samoel.saleh@uobasrah.edu.iq) ORCID ID 0000 – 0002 – 3046 – 168X
*(ihsan.qasim@uobasrah.edu.iq) ORCID ID 0000 – 0001 – 9256 – 5073

Cite this article

Salih S M & Al-abboodi I (2021). Strength and behaviour assessment of axially loaded concrete filled steel tubular stub columns. Turkish Journal of Engineering, 5(4); 154-164

Research Article / DOI: XXXXXXXXXXXX

Received: 07/02/2020; Accepted: 25/05/2020

theoretical analysis. Yang et al. (2013) developed a finite element model to simulate ultra-high strength concrete-filled steel tubes under compression using ABAQUS software. They validated their model by comparing the simulation results with the data of some experimental tests. Bagherinejad et al. (2015) numerically studied the effect of eccentric loading on the buckling behaviour of rectangular CFST columns using ABAQUS software. Zhao et al. (2018) used experimental and numerical analyses to investigate the behavior of large-scale circular CFST columns under axial compression. They concluded that the horizontal stiffener has a significant constraining effect on the external deformation at the surface of steel tube, whereas the vertical stiffeners may improve the bending resistance and initial stiffness of the column. Al-Kutti (2018) investigated the possibility of using the Drucker Prager model in the simulation of concrete material for the finite element modelling of concrete CFST members. He suggested empirical formulae to evaluate the material model parameters for confined concrete under compression with a compressive strength that ranged from 25 to 100 MPa. Also, in 2018, Ouyang and Kwan (2018) developed a numerical model to study the performance of square CFST columns taking into account the triaxial behaviour and lateral expansion of the concrete core. They found that the increase of corner radius of steel sections improves the post-peak response of columns with square sections. Nguyen et al. (2019) employed a nonlinear finite element analysis to study the effect of tie and slip models in the representation of steel concrete interaction on the flexural resistance of the compact CFST columns. The comparison with some experimental data showed that the tie model provided higher accurate results compared with those predicted by the slip model.

It can be noted from the previous literature review that the interaction in the behaviour of the steel and concrete materials and the configuration of CFST column section may represent the major factors that must be considered in more details with the analysis of such members. However, most of the previous research studied the effect of some parameters in the analysis of CFST columns without considering the variation of other parameters that may lead to significant changes in the strength and behaviour of such structural members. In the present work, a three-dimensional, nonlinear FEA was conducted using ABAQUS software to assess the strength and behaviour of CFST stub columns under axial compression. The effects of the concrete strength (grade of concrete), the steel yield stress, the steel tube wall thickness, and the section shape (circular and square) were examined. This assessment may help to understand the parameters that could play a major role in the axial compressive strength of such composite columns.

2. FINITE ELEMENT MODELLING AND VERIFICATION

2.1. General

In the current study, ABAQUS software has been employed in the finite element analysis. Eight-noded brick elements (C3D8R) were employed to simulate the structural elements (concrete and steel tube) of the CFST columns. To determine an optimal finite element mesh that gives a low computational time with a relatively accurate solution, mesh convergence studies were investigated. The element size was chosen as 5% of the overall diameter (circle) or width (square) for column cross-sections. The adopted finite element mesh for both shapes of CFST columns is presented in Fig. 1.

The concept of surface-to-surface contact, presented by Tao et al. (2011), has been used to simulate the interaction between the concrete and steel. As per this method, a coefficient of friction of 0.6 in a direction tangent to the interaction face was adopted in the Coulomb friction model. In addition, a hard contact model was used in the normal direction between the two contact surfaces of steel and concrete. This can prevents the penetration of the interface in compression and permits its separation in tension. According to Tao et al. (2013), the initial local imperfections have no important influence on the response of CFST columns. Therefore, it has been ignored in the modelling procedure.

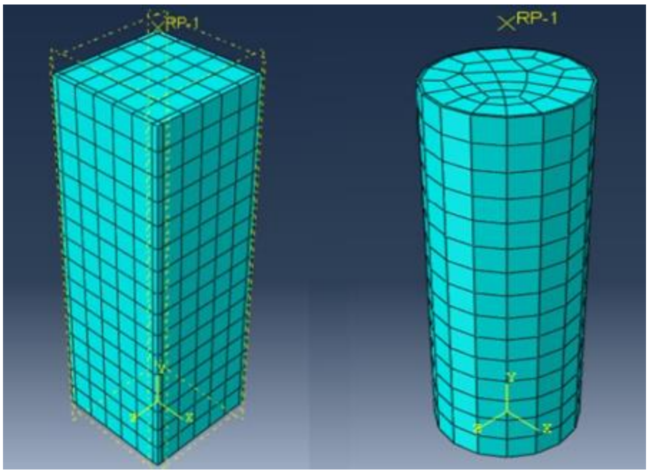

Figure 1. Finite element mesh for the CFST columns used in the analysis

2.2. Material Modelling

In the present study, the constitutive behaviour of the steel was considered as an elastic perfectly plastic material, with a modulus of elasticity equals to 200 GPa and a Poisson's ratio of 0.3. Moreover, Von-Mises yield criterion was used to define the steel material yield surface. The damage plasticity model was adopted to model the concrete material.

As the CFST columns loaded axially, the concrete core expanded laterally and confined by the outside steel tube. Due to this confinement, an increase in the strength and ductility of the concrete could be induced. The constitutive stress strain relationship for the concrete and corresponding parameters of the damage plasticity model were considered as suggested by Tao et al. (2013). Moreover, Poisson's ratio was taken as 0.2, and the value of initial modulus of elasticity was calculated as $4700\sqrt{f_c'}$, as recommended by ACI Committee 318.

2.3. Boundary Conditions and Loading

Most researchers used end plates when testing the CFST stub columns in order to minimize any influences on the end conditions. Therefore, it is suitable to use clamped end conditions for the top and bottom surfaces of the structural member, in which all degrees of freedom will be fixed except the top axial displacement where the load is applied. On the other hand, a displacement control mode was considered to simulate the applied axial compression at the top end of the modelled CFST stub columns.

2.4. Model Verification

In order to check the accuracy and efficiency of the adopted procedure, the predicted behaviour and ultimate compressive strengths were compared with some previous experimental data. The adopted experimental tests specimens were chosen with various dimensions and material properties to cover a wide range of case studies, which have been investigated by different researchers. The dimensions, material properties and values of the predicted ultimate compressive strength (N_{up}) and the experimental test strength (N_{ue}) of the selected specimens for verification are given in Tables 1 and 2. It can be observed that the predicted outputs showed a good agreement with the test results, where mean values of 1.008 and 1.035 for the ratio (N_{ue}/N_{up}) were obtained with standard deviation values of 0.071 and 0.036 for specimens with square and circular cross-sections, respectively. Moreover, Fig. 2 and 3 show a comparison between the numerically predicted and experimentally measured axial load – axial shortening profiles for the analysed members.

3. RESULTS AND DISCUSSION

The verified nonlinear finite element model was used to carry out a parametric study aims to assess the performance of stub columns under different conditions. A total of eighty columns, equally divided into two categories (i.e. square and circular sections), were analyzed under axial compression. The concrete grade (f_c'), the steel yield stress (f_y), the steel tube wall thickness (t), and the section shape (circular and square) were considered the main parameters. All columns were chosen with the same diameter or width (D) (at 125 mm) and with two values of (D/t) ratios (namely 50 and 25). To avoid impacting the end conditions and overall buckling, the length of the analyzed stub columns (L) was chosen as 3D. A summary of the CFST stub columns' details is presented in Tables 3 and 4, whereas the resulting axial load versus the axial shortening relationships are shown in Figs. 4 and 5.

3.1 Strength Assessment

The strength and behaviour of concrete core are largely affected by its grade value. Therefore, five grades of concrete, ranging from 25 to 85 MPa, were considered to cover the behaviour of such structural members with normal and high strength concretes. It can be seen from Table 3 that the ultimate capacity of columns increases as the concrete compressive strength increases. However, the action of this parameter may be reduced with the variation in other parameters. It was noted that, when the concrete grade increased from 25 to 85 MPa for a circular CSFT column, where a D/t ratio of 50 and a steel yield stress of 275 MPa, a double value of the column's ultimate capacity has been obtained. Moreover, for a column with the same properties, excepting the steel yield stress of 500 MPa, the ultimate strength was increased by about 72%. On the other hand, the increase in ultimate strength along with the increase in concrete grade reduced by 20% when the D/t ratio changed from 50 to 25.

Four values of steel yield stresses of 275, 350, 425, and 500 MPa were examined to assess their influence on the ultimate capacity of the considered CFST columns. It was noted that the ultimate capacity of the circular columns with a D/t ratio of 50 and a concrete grade of 25 MPa increased by about 42% when the value of steel yield stress increased from 275 to 500 MPa. However, the increasing percentage was only 20% when the concrete grade value is 85 MPa. Whereas, with the change of (D/t) ratio from 50 to 25 and the same concrete grade of 25 MPa is adopted, the ultimate capacity of the analyzed circular columns increased by 46% and 57% with steel yield stress values of 275 MPa and 500 MPa, respectively. The variation in the columns' strengths with respect to the considered parameters is presented in Table 4 for those CFST columns with square sections. It can be noticed that the effect of each individual parameter is slightly more in the square than that in the circular columns.

To consider the influence of the shape of CFST column cross section on its ultimate capacity, a strength index is adopted to verify the column section strength as $SI = N_{up}/N_{uo}$, where $N_{uo} = A_s f_y + 0.85 A_c f_c'$, as determined by the ACI code for the evaluation of sectional capacity of such composite columns, A_s and A_c are the cross sectional areas of steel and concrete, respectively.

The strength index (SI) is calculated for each individual column, and the results are shown in Tables 3 and 4. Numerical results showed, in general, that SI values for columns with circular section is considerably greater than that for the columns with square sections. In addition, the strength index decreased with the increased concrete grade for circular columns, but increased for square columns. This may be related to the interaction between the concrete core and the surrounding steel tube, which is more efficient in circular columns than in square columns. On the other hand, there is no significant change in the effect of the column shape on the strength index with the change of steel yield stress or steel tube thickness.

3.2 Behaviour Assessment

As can be seen in Figs. 4 and 5, the axial load versus the axial shortening relationships were generally similar in shape until the ultimate load is reached. After that, a difference can be noticed due to the effect of the considered parameters. Nevertheless, in spite of the increase in the steel yield stress, the ductility of the CFST columns reduced with the increase in concrete grade. This is agreed with the engineering expectation since the ductility of concrete reduces with the increase in its strength. On the other hand, it can be clearly noted that the reduction in the values of D/t ratio caused an increase in the ductility of the stub columns. This is mainly due to the increased in concrete confinement provided by the steel tube.

By comparing Figs. 4 and 5, it can be observed that circular columns are more ductile than the square, where the post peak curves of square columns are steeper than those obtained in the circular columns. This may be attributed to the property of the circular shape for the steel tube, which could produce more efficient confinement and then more ductile behaviour to the concrete core than the square steel tubes.

4. CONCLUSIONS

The study adopted a three-dimensional, nonlinear finite element analysis using ABAQUS software to assess the response of CFST stub columns subjected to axial compression. The influence of a number of parameters that could affect the performance of this kind of structural members were investigated. These parameters include the grade of concrete, the steel yield stress, the steel tube wall thickness, and the shape of the column cross-section (circular or square). A total of eighty stub columns divided into two groups depending on their cross-sectional shape were analyzed. Based on the results of the parametric study, a number of conclusions can be drawn:

1. The increase of concrete grade leads to an increase in the ultimate strength of CFST stub columns. On the other hand, a reduction in the ductility has been observed when concrete grade increased.
2. The changes in steel yield stress and D/t ratio have caused a significant influence on the ultimate strength and ductility of columns, in which an increase in their values was observed. The effect of these two parameters may reduce with the increase in concrete grade.
3. The composite interaction of concrete in the presence of the surrounding steel tube plays an important role in determining the strength index, SI, values. The effect of this interaction is more pronounced when circular sections are adopted.
4. CFST columns with circular columns showed higher ductility than that obtained in the case of square section.
5. The ductility of circular CFST stub columns is higher than that of square CFST columns. Thus, the use of square CFST columns with high strength concretes should be carefully considered, especially inseismically active areas.

Table 1. Test data for Square CFST stub columns

No	Specimen Label	Dimensions (mm)			f_c' (MPa)	f_y (MPa)	N_{up} (kN)	N_{ue} (kN)	N_{ue}/N_{up}	Test Source
		D	t	L						
1	A1	120	5.80	360	83.0	300.0	1744	1697	0.973	Liu and Gho (2005)
2	RC2-1	120	2.86	360	50.8	228.0	968	992	1.025	Han (2002)
3	UCFT25	250	2.50	750	50.1	234.3	3390	3230	0.953	Tao et al. (2005)
4	R7-1	106	4.00	320	89.0	495.0	1662	1749	1.052	Liu (2005)
5	SU-040	200	5.00	600	27.2	265.8	2043	2312	1.132	Huang et al. (2002)
6	NS1	186	3.00	540	32.0	300.0	1699	1555	0.915	Uy (2000)
Mean									1.008	
Standard Deviation									0.071	

Table 2. Test data for Circular CFST stub columns

No.	Specimen Label	Dimensions (mm)			f_c' (MPa)	f_y (MPa)	N_{up} (kN)	N_{ue} (kN)	N_{ue}/N_{up}	Test Source
		D	t	L						
1	C4	115	3.99	300	83.9	343.0	1338	1308	0.978	Giakoumelis and Lam (2004)
2	C30-3	100	1.90	300	111.7	404.0	1050	1100	1.048	Yu et al. (2008)
3	D4M4C2	113	2.89	340	32.9	360.0	738	788	1.068	Gupta et al. (2007)
4	CU-040	200	5.00	600	27.2	265.8	1884	2013	1.068	Huang et al. (2002)
5	CC8-C-8	222	6.47	666	77.0	843.0	7237	7304	1.009	Sakino et al. (2004)
6	C1	140	3.00	602	28.2	285.0	849	881	1.038	Schneider (1998)
Mean									1.035	
Standard Deviation									0.036	

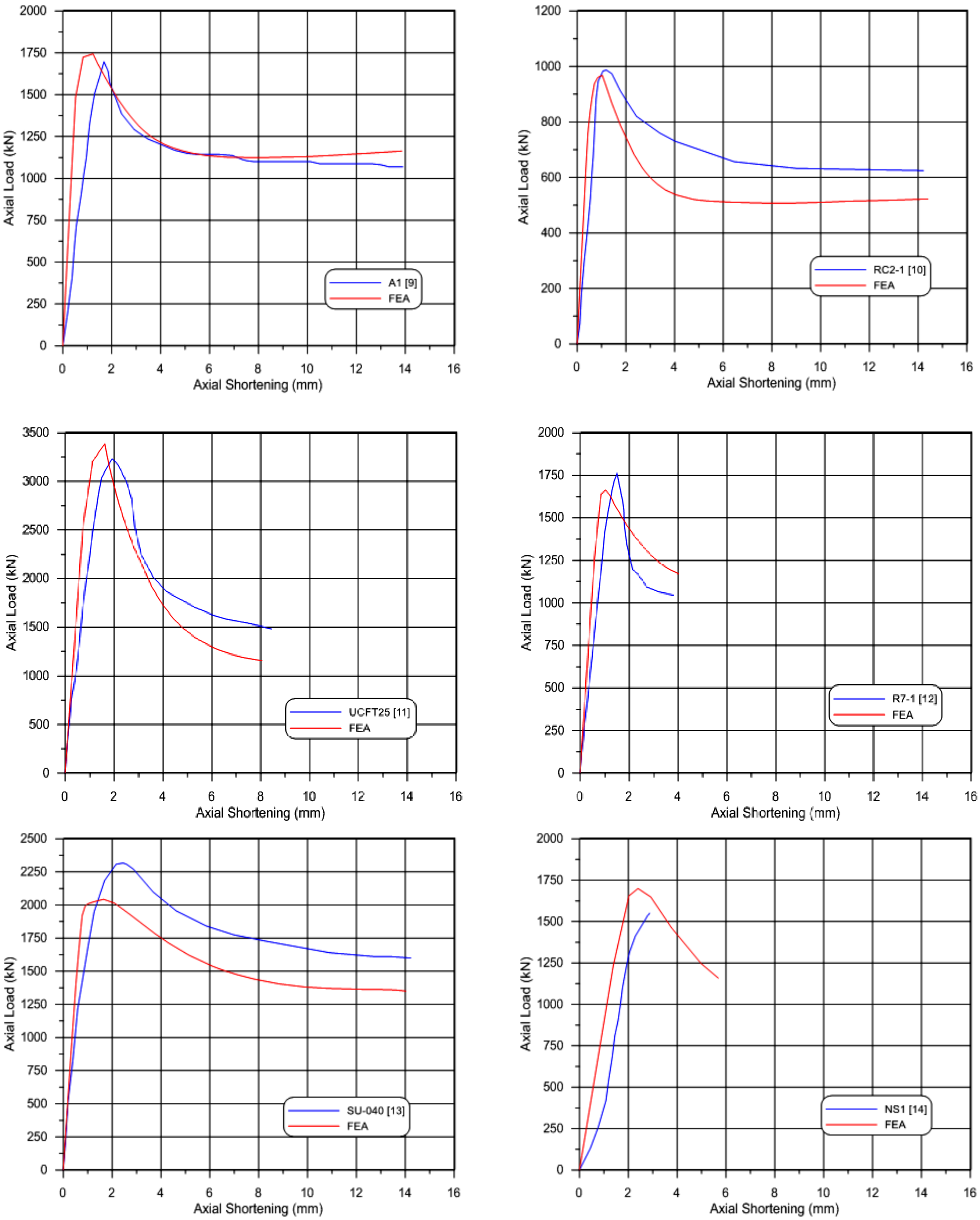

Figure 2. Predicted and measured axial load-axial shortening profiles for square CFST columns

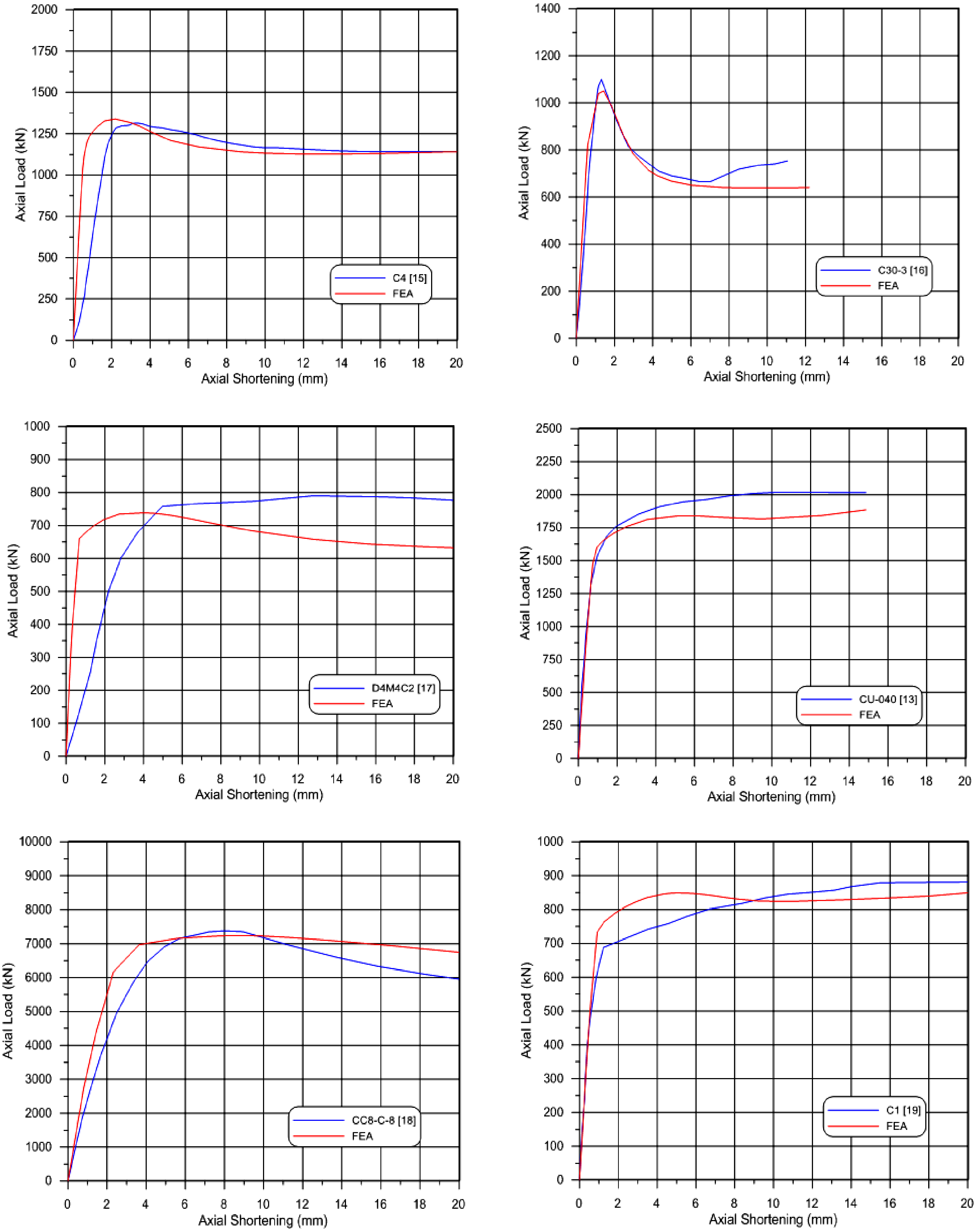

Figure 3. Predicted and measured axial load-axial shortening profiles for Circular CFST columns

Table 3. Details of analyzed circular CFST stub columns

No	D /t	f_y (MPa)	f_c' (MPa)	N_{up} (kN)	N_{uo} (kN)	SI
1	50	275	25	623	505	1.234
2			40	786	649	1.211
3			55	948	793	1.195
4			70	1105	938	1.178
5			85	1271	1082	1.175
6	50	350	25	713	577	1.235
7			40	876	721	1.215
8			55	1031	865	1.191
9			70	1205	1010	1.194
10			85	1371	1154	1.188
11	50	425	25	800	649	1.232
12			40	970	793	1.222
13			55	1118	938	1.192
14			70	1275	1082	1.179
15			85	1449	1226	1.182
16	50	500	25	887	721	1.229
17			40	1059	866	1.223
18			55	1221	1010	1.209
19			70	1368	1154	1.185
20			85	1523	1298	1.173
21	25	275	25	911	739	1.233
22			40	1072	872	1.230
23			55	1222	1004	1.217
24			70	1363	1136	1.199
25			85	1488	1269	1.173
26	25	350	25	1073	880	1.219
27			40	1237	1013	1.221
28			55	1393	1145	1.216
29			70	1538	1278	1.204
30			85	1671	1410	1.185
31	25	425	25	1235	1022	1.208
32			40	1404	1154	1.216
33			55	1565	1287	1.216
34			70	1709	1419	1.204
35			85	1850	1552	1.192
36	25	500	25	1391	1163	1.196
37			40	1568	1296	1.210
38			55	1729	1428	1.211
39			70	1877	1560	1.203
40			85	2024	1693	1.195

Table 4. Details of analyzed square CFST stub columns

No.	D /t	f_y (MPa)	f_c' (MPa)	N_{up} (kN)	N_{uo} (kN)	SI
1	50	275	25	705	643	1.097
2			40	912	826	1.104
3			55	1115	1010	1.104
4			70	1333	1194	1.117
5			85	1538	1377	1.117
6	50	350	25	804	735	1.095
7			40	1006	918	1.095
8			55	1211	1102	1.099
9			70	1433	1286	1.114
10			85	1635	1469	1.113
11	50	425	25	896	827	1.084
12			40	1100	1010	1.088
13			55	1320	1194	1.106
14			70	1526	1377	1.108
15			85	1731	1561	1.109
16	50	500	25	994	919	1.082
17			40	1204	1102	1.093
18			55	1414	1286	1.100
19			70	1627	1469	1.107
20			85	1836	1653	1.111
21	25	275	25	1008	941	1.071
22			40	1202	1110	1.083
23			55	1391	1278	1.088
24			70	1586	1447	1.096
25			85	1768	1616	1.094
26	25	350	25	1193	1121	1.064
27			40	1389	1290	1.077
28			55	1574	1458	1.079
29			70	1767	1627	1.086
30			85	1962	1796	1.093
31	25	425	25	1376	1301	1.057
32			40	1571	1470	1.069
33			55	1764	1638	1.076
34			70	1953	1807	1.081
35			85	2140	1976	1.083
36	25	500	25	1557	1481	1.051
37			40	1746	1650	1.058
38			55	1941	1818	1.068
39			70	2138	1987	1.076
40			85	2327	2156	1.079

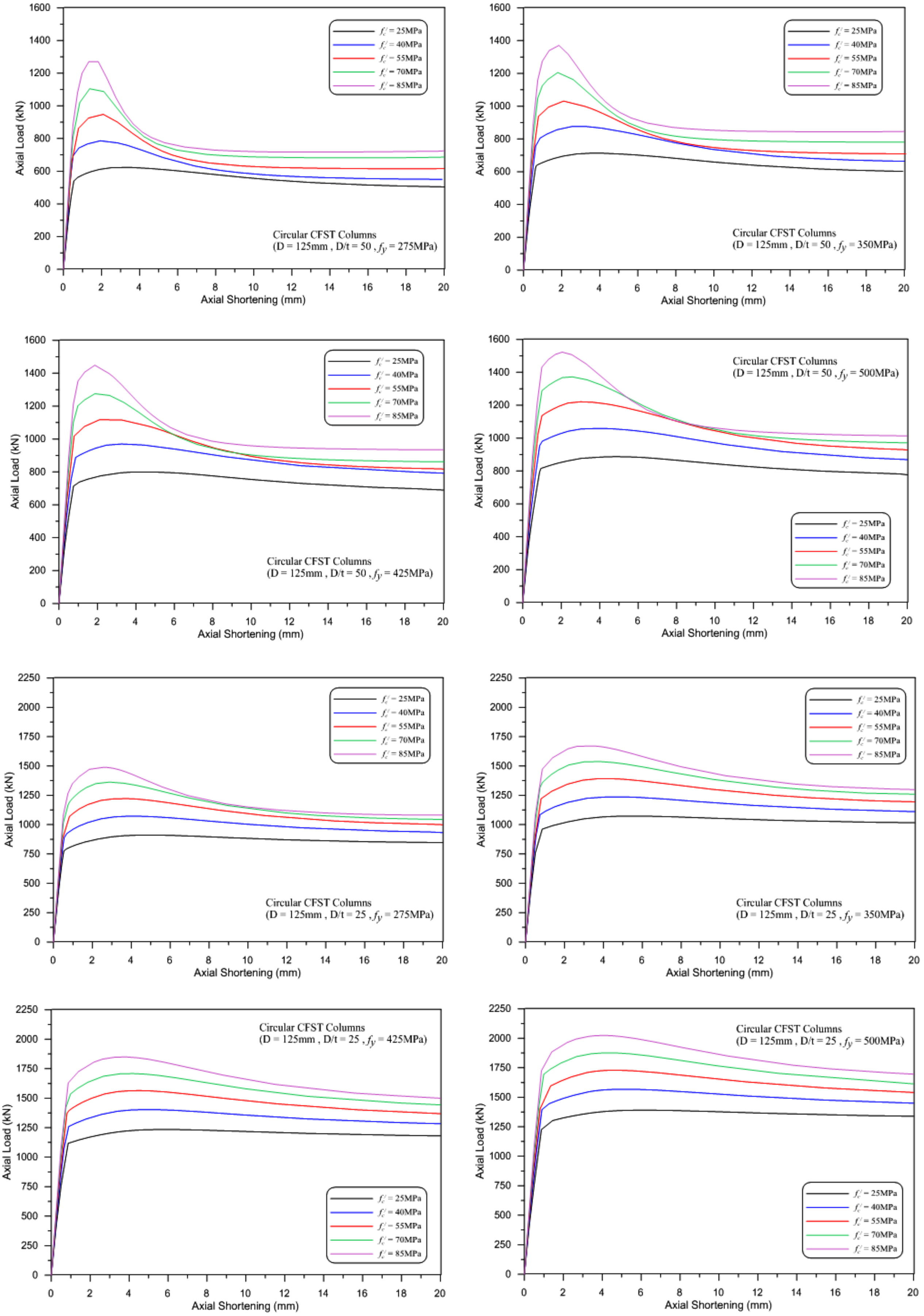

Figure 4. Axial load – axial shortening relationships for analyzed circular CFST Stub columns

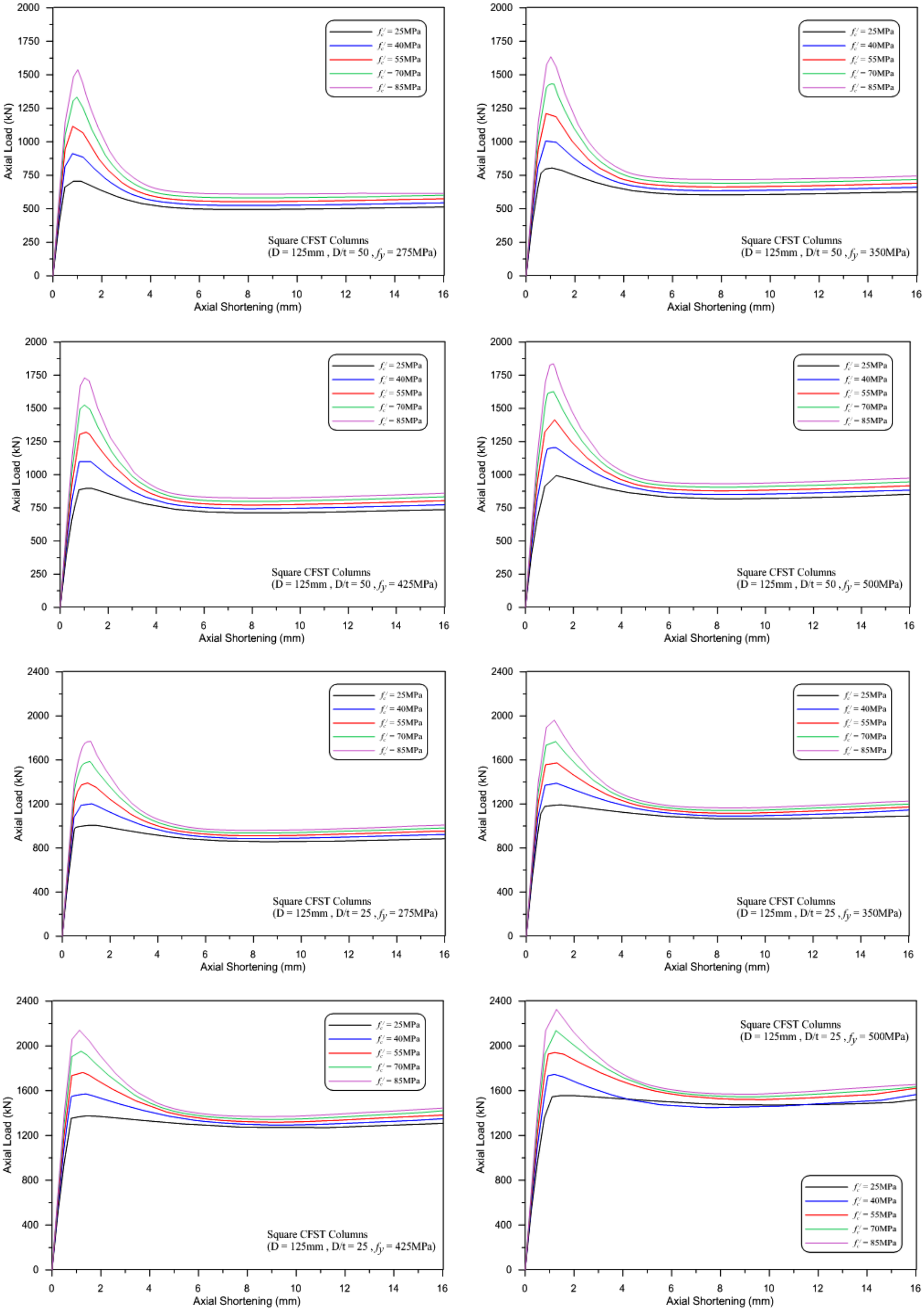

Figure 5. Axial load – axial shortening relationships for analyzed square CFST Stub columns

REFERENCES

ABAQUS (2011). Abaqus Theory Manual. ABAQUS version 6.11. Dassault Systèmes Simulia Corp, USA.

ACI Committee (2014). Building code requirements for structural concrete (ACI 318-14) and commentary (ACI 318R-14). American Concrete Institute, Farmington Hills (MI), Detroit, USA.

Al-Kutti W A (2018). Parameters estimation of Drucker-Prager plasticity criteria for steel confined circular concrete columns in compression. MATEC Web of Conferences, 149, 01048. DOI: 10.1051/matecconf/201814901048

Bagherinejad K, Hosseinpour E & Hosseini S H (2015). Evaluation of rectangular concrete filled steel hollow section beam-columns. Journal of Asian Scientific Research, 5(1), 46–59. DOI: 10.18488/journal.2/2015.5.1/2.1.46.59

Deng Y, Norton T R & Tuan C Y (2013). Numerical analysis of concrete filled circular steel tubes. Structures and Buildings, 166(1), 3–14. DOI: 10.1680/stbu.11.00001

Giakoumelis G & Lam D (2004). Axial capacity of circular concrete-filled tube columns. Journal of Constructional Steel Research, 60(7), 1049–1068. DOI: 10.1016/j.jcsr.2003.10.001

Gupta P K, Sarda S M & Kumar M S (2007). Experimental and computational study of concrete filled steel tubular columns under axial loads. Journal of Constructional Steel Research, 63(2), 182–193. DOI: 10.1016/j.jcsr.2006.04.004

Han L H (2002). Tests on stub columns of concrete-filled RHS sections. Journal of Constructional Steel Research, 58(3), 353–372. DOI: 10.1016/S0143-974X(01)00059-1

Han L H, Yao G H & Tao Z (2007). Performance of concrete-filled thin-walled steel tubes under pure torsion. Thin-Walled Structures, 45(1), 24–36. DOI: 10.1016/j.tws.2007.01.008

Huang C S, Yeh Y K, Liu G Y, Hu H T, Tsai K C, Weng Y T, Wang S H & Wu M H (2002). Axial load behavior of stiffened concrete-filled steel columns. Journal of Structural Engineering, 128(9), 1222–1230. DOI: 10.1061/(ASCE)0733-9445(2002)128:9(1222)

Liu D & Gho W M (2005). Axial load behavior of high-strength rectangular concrete-filled steel tubular stub columns. Thin-Walled Structures, 43(8), 1131–1142. DOI: 10.1016/j.tws.2005.03.007

Liu D (2005). Tests on high-strength rectangular concrete-filled steel hollow section stub columns. Journal of Constructional Steel Research, 61(7), 902–911. DOI: 10.1016/j.jcsr.2005.01.001

Mallesh M, Asif M & Sreyas G G (2016). Nonlinear analysis of concrete filled stainless steel tubular column. International Research Journal of Engineering and Technology, 3(8), 1108–1111.

Nguyen D H, Hong W K, Ko H J & Kim S K (2019). Finite element model for the interface between steel and concrete of CFST (concrete-filled steel tube). Engineering Structures, 185, 141–158. DOI: 10.1016/j.engstruct.2019.01.068

Ouyang Y & Kwan A K H (2018). Finite element analysis of square concrete-filled steel tube (CFST) columns under axial compressive load. Engineering Structures, 156, 443–459. DOI: 10.1016/j.engstruct.2017.11.055

Sakino K, Nakahara H, Morino S & Nishiyama I (2004). Behavior of Centrally loaded concrete filled steel tube short columns. Journal of Structural Engineering, 130(2), 180–188. DOI: 10.1061/(ASCE)0733-9445(2004)130:2(180)

Schneider S P (1998). Axially loaded concrete filled steel tubes. Journal of Structural Engineering, 124(10), 1125–1138. DOI: 10.1061/(ASCE)0733-9445(1998)124:10(1125)

Tao Z, Han L H & Wang Z B (2005). Experimental behavior of stiffened concrete-filled thin-walled hollow steel structural (HSS) stub columns. Journal of Constructional Steel Research, 61(7), 962–983. DOI: 10.1016/j.jcsr.2004.12.003

Tao Z, Uy B, Liao F Y & Han L H (2011). Nonlinear analysis of concrete-filled square stainless steel stub columns under axial compression. Journal of Constructional Steel Research, 67(11), 1719–1732. DOI: 10.1016/j.jcsr.2011.04.012

Tao Z, Wang Z B & Yu Q (2013). Finite element modelling of concrete-filled steel stub columns under axial compression. Journal of Constructional Steel Research, 89, 121–131. DOI: 10.1016/j.jcsr.2013.07.001

Uy B (2000). Strength of concrete filled steel box columns incorporating local buckling. Journal of Structural Engineering, 126(3), 341–352. DOI: 10.1061/(ASCE)0733-9445(2000)126:3(341)

Yang Z, Zhang Y, Chen M & Chen G (2013). Numerical simulation of ultra-strength concrete filled steel columns. Engineering Review, 33(3), 211–217.

Yu Q, Tao Z & Wu Y X (2008). Experimental behavior of high performance concrete-filled steel tubular columns. Thin-Walled Structures, 46(4), 362–370. DOI: 10.1016/j.tws.2007.10.001

Zhao L, Cao W, Guo H, Zhao Y, Song Y & Yang Z (2018). Experimental and numerical analysis of large scale circular concrete-filled steel tubular columns with various constructional measures under high axial load ratios. Applied Sciences, 8(10), 1894. DOI: 10.3390/app8101894

Turkish Journal of Engineering

https://dergipark.org.tr/en/pub/tuje

e-ISSN 2587-1366

Investigation of high temperature effects in different mineral additive light mortars

Behcet Dündar *1, **Emriye Çınar**1

1Osmaniye Korkut Ata University, Engineering Faculty, Civil Engineering Department, Osmaniye, Turkey

Keywords
Light mortar
Pumice
Mineral additive
High temperature

ABSTRACT

In this study, physical and mechanical properties of light mortars produced with Fly Ash (FA) contributed pumice aggregates, Colemanite (K), Blast Furnace Slag (BFS), Marble powder (MP) were investigated under high temperature. Mortar samples were produced in the dimensions of 40x40x160 mm. At the preparation of mortars, pumice (0-4mm) as a fine aggregate and CEM I 42.5R Portland Cement were replaced with. 1%, 2% and 3% by weight of K respectively and 10%, 20% and 30% of YFC, MT and UK were replaced with cement in light mortars mixture. The produced mortar samples were removed from the mold after 24-hour setting and subjected to a cure at a temperature of 20±2°C in the standard cure pool for 28 days. The flexural and compressive strength of the mortar samples filling the 7th day were determined. Physical properties such as water absorption, porosity and unit volume weight of 28 days cured mortars were determined and flexural and compressive strengths were calculated. At the end of 28th day samples, which were reached its final strength, were exposed to 200 ^{0}C, 400 ^{0}C, 600 ^{0}C and 800 ^{0}C heats in High Temperature Oven. It is observed that with increasing temperature, weight loss increases, flexural and compressive strengths decrease in all samples. With the use of mineral additives, it was observed that both the weight losses and the losses in flexural and compressive strengths decreased and the mortars became more resistant to temperature.

1. INTRODUCTION

As a result of population growth and land restriction, the need for high-rise buildings and underground constructions is rapidly increasing to solve housing and transportation problems effectively. In such civil engineering structures, it is faced that large amounts of fire damage during construction and service. It is known that fires, which are frequently encountered worldwide in recent years, seriously threaten personal and property security. It is known that high temperature causes a decrease in the mechanical strength of the concrete and creates harmful effects at the structural level due to the high temperature exposure of the reinforcement (Seshu and Pratusha 2013; Heikal et al. 2013).

The effect of high temperature on the strength of mortar and concrete is generally grouped as material and environmental factors. Material factors include aggregate, aggregate-cement paste interface, thermal mismatch of composite components and properties of cement paste (Khaliq et al. 2015). On the other hand, environmental factors include heating speed, exposure time to maximum temperature, cooling rate, loading conditions and humidity, which are important when examining the behavior of mortar and concrete samples at high temperatures. Previous studies have shown that the strength and elasticity module of cement-based mortar and concrete samples decrease with the increase in temperature (Li et al. 2018; Pan et al. 2018).

It is the decomposition of hydration products that cause concrete to lead to loss of strength at high temperatures. The researchers stated that the decomposition of the cementitious matrix started above 105 ° C. The first step of chemical and physical decomposition is to release the water in the pores and chemically bound water in the structure of calcium silicate hydrate (C-S-H) gels (Arioz 2007). At this step, other hydrates and ettringite also begin to decompose. Also, aggregate may start to be affected according to its origin and type (Gawin et al. 2004). Approximately 300-400 °C, chemically bound intermediate layer water in the C-S-H gel evaporates. Also, the first microcracks begin to appear in the $Ca(OH)_2$ and anhydrite cement areas. At this stage, $Ca(OH)_2$ decomposes into CaO and H_2O. However, in the cooling process, CaO can rehydrate to $Ca(OH)_2$, and this rehydration creates a significant

---

* **Corresponding Author**

*(behcetdundar@osmaniye.edu.tr) ORCID ID 0000 – 0003 – 0724 – 9469
(emriyecinar@osmaniye.edu.tr) ORCID ID 0000 – 0002 – 9435 – 2968

Cite this article

Dündar B & Çınar E (2021). Investigation of high temperature effects in different mineral additive light mortars. Turkish Journal of Engineering, 5(4), 165-170

Research Article / DOI: XXXXXXXXXXXX

Received: 27/02/2020; Accepted: 08/05/2020

volume expansion of about 44%. This volumetric expansion increases the number of cracks. It is known that the use of mineral additives in cement based materials consumes $Ca(OH)_2$ (Lin et al. 1996; Mendes et al. 2011).

However, in recent years, interest in consuming substitute materials such as solid wastes in the construction industry has increased steadily. The consumption of waste materials is compatible with basic environmental approaches in terms of preventing waste, reusing waste materials, reducing storage areas, reducing energy from waste and saving natural resources (Dimitriou et al. 2018; Juan-Vandes et al. 2018).

Although alternative materials such as wastes are used in many application areas, their technical characteristics, financial aspects and environmental effects should be taken into consideration. In the construction industry, the idea of sustainability and green production promotes the use of various waste materials instead of raw materials such as cement and aggregates (Tam et al. 2018; Huseien et al. 2019). Therefore, it leads to the production of an environmentally friendly structure with the use of waste materials (Mohammadhosseini et al. 2018).

Portland cement is the most widely used binder in the construction industry. On the other hand, Portland cement consumption has been discussed for many years due to approximately 1.5 billion tons of CO_2 emission per year and 36% of global energy consumption (Andrew 2018; Kermeli et al. 2019).

Many researches are conducted on both fire resistance and the evaluation of waste products. In recent years, mineral additives have been used in mixtures to provide high temperature resistance. Among them, fly ash, blast furnace slag and silica fume are the most common (Akca and Özyurt 2018; Liang et al. 2018).

The effects of high temperature on the hardened properties of blended mortars containing pumice and fly ash powder were investigated. The produced mortars were exposed to 300 °C, 600 °C and 900 °C for 3 hours in mixtures containing 0%, 20%, 40% and 60% FA. Experimental results showed that pumice mortar containing 60% FA performs better, especially at 900 °C (Aydın and Baradan 2007).

In this study, the use of mineral additives was investigated in order to evaluate the waste products and to increase the durability of cement-based materials against the fire disaster that can be encountered today. In this context, 1%, 2% and 3% by weight of cement, K, 10%, 20% and 30% of BFS, MP and FA were replaced by light mortars. After curing the mortar samples for 7 days, their mechanical properties such as flexural and compressive strengths were determined, and after 28 days of curing, their physical properties such as water absorption and porosity were determined. Mortar samples were exposed to 200, 400, 600 and 800 ^{0}C temperatures after 28 days. Weight losses, flexural and compressive strengths were determined after the applied heat.

2. MATERIALS AND METHODS

2.1. Materials

The cement, which is among the components of the mortar used in the production of test samples, is CEM I 42,5 R type cement produced in accordance with TS EN 197-1 (2012). Fly ash (FA), Blast Furnace Slag (BFS), Colemanite (K) and Marble Powder (MP) are used as mineral additives and their physical and chemical properties were given together cement in Table 1. Mineral additives were used by replacing with cement at the rates specified by weight. While mineral additives K were used at 1%, 2%, 3% rates, BF, AS and BF were used at 10%, 20%, 30% rates. In the experimental study, city water of Osmaniye Province, which complies with TS EN 1008 was used (2003).

Pumice aggregate with 0-4 mm grain size was used in the mortar samples produced within the scope of the study. It contains numerous pores from macro scale to micro scale due to sudden cooling of the gases in the body and sudden cooling during pumice formation. It is light, can float in water for a long time, has low permeability and is highly insulated since it is generally interconnected between pores. Chemical content of silica can be up to 75%. The SiO_2 ratio of the rock gives the rock an abrasive feature. Al_2O_3 composition provides high resistance to fire and heat. Pumice deposits in Turkey, Urgup Avanos and Kayseri Talas- Tomarza-Develi and concentrated in Osmaniye (Yasar and Erdogan 2005). In this study, pumice aggregate, whose chemical properties are given in table 2, which has the basic character obtained from Osmaniye Province, was used.

Table 1. Chemical and physical analysis results of CEM I 42,5 R Portland cement, fly ash (FA), Blast Furnace Slag (BFS), Colemanite (K) and Marble Powder (MP)

Chemical Analysis	CEM I 42,5/R	FA	BFS	K	MP
B_2O_3	-	-		39,85	-
SiO_2	19,33	47,4	32,8	5,60	4,67
Al_2O_3	4,74	19,8	11,8	0,15	0,08
Fe_2O_3	2,72	11,8	1,45	0,03	0,03
CaO	63,20	6,66	39,8	27,24	51,80
MgO	0,98	4,76	4,15	2,84	18,38
Na_2O	0,12	0,57	0,51	0,10	0,05
Ignition Loss	3,94	2,76	2,2	24,06	45,98
Specific Surface (cm^2/g)	3983	3126	4982	3839	6740
Specific Weight (g/cm^3)	3,12	1,99	2,8	2,50	2,63

Table 2. Chemical analysis of basaltic pumice

Chemical Analysis	Pumice (%)
SiO_2	45,95
Al_2O_3	19,95
Fe_2O_3	7,53
CaO	13,23
MgO	6,24
Na_20+K_2O	6,69
Diğer	0,41
Total	100

2.2 Methods

The amount of materials used in the samples produced in the experimental study are given in Table 3. Reference sample consists the mixture of pumice aggregate, cement and water. In other samples, FA, BFS, K and MP were used and the difference was observed. 10%, 20%, 30% FA, BFS, MP and 1%, 2%, 3% K mineral additives were replaced by weight of cement. After making the mortar mixture, the lubricated molds were placed on the cement shaking table and the concrete mortar was poured into the molds in two stages. The mortar samples, which completed the set in the mold for 24 hours, were removed from the molds and cured in standard curing pools for 7 and 28 days. The flexural strength determination in accordance with TS EN 196-1 (2016) standard and compressive strength in accordance with TS EN 12390-4 (2002) were determined for the mortar samples filling the 7th day. It was calculated in accordance with TS EN 1170-6 (1999) standard with the help of the Archimedes principle in order to determine the physical properties of the mortar samples filling the 28th day, such as water absorption and porosity. High temperature application was carried out in accordance with the principles specified in TS EN 13501-1 (2019) standard.

According to the standards, real fire occurs between 20-1000 °C and within 15-300 minutes. Mortar samples were applied at a temperature of 200 °C, 400 °C, 600 °C and 800 °C with a temperature increase rate of 10 °C / min in a 1800 ºC laboratory type oven and kept in the oven for 60 minutes at all temperatures. Then it was left to cool until it reached the temperature of the laboratory conditions. Samples subjected to high temperature, flexural, compressive tests and weight losses were determined after cooling.

3. RESULTS AND DISCUSSION

The water absorption (%) values by weight of the mortar samples are given in Figure 1 and porosity (%) values are given in Figure 2. A decrease in water absorption and porosity rates was observed in 30% of all mineral additives and in all ratios of K. With the use of FA, water absorption and porosity values increased up to 20% compared to the reference sample, while its use decreased by 30%. In the use of BFS, it was observed that the water absorption and porosity rates decreased with the increase of BFS rate and low water absorption and porosity values in all ratios compared to the reference sample. In case of using 1% and 3% of K, water absorption and porosity values decrease according to the reference, while 2% increase has been observed. With the use of MP 10%, water absorption and porosity values reached their highest value and a decrease was observed with the increase in the rate. The lowest water absorption value was obtained with the use of 30% BFS with the rate of 5.91% and the lowest water absorption with the ratio of 9.01% in mortars where 10% MP was used. The highest porosity value was obtained in mortars using 10% MP with a rate of 17,30%, and the highest water absorption was achieved with the use of 30% BFS with a rate of 11,97%. With the increase of mineral additives in the mortar, the amount of fine material increases. The need for water increases as the surface area increases with the increase of the fine substance. Settlement difficulties due to the need for water reveals difficulties and causes it to settle more porous, in this case, it causes an increase in water absorption and porosity values.

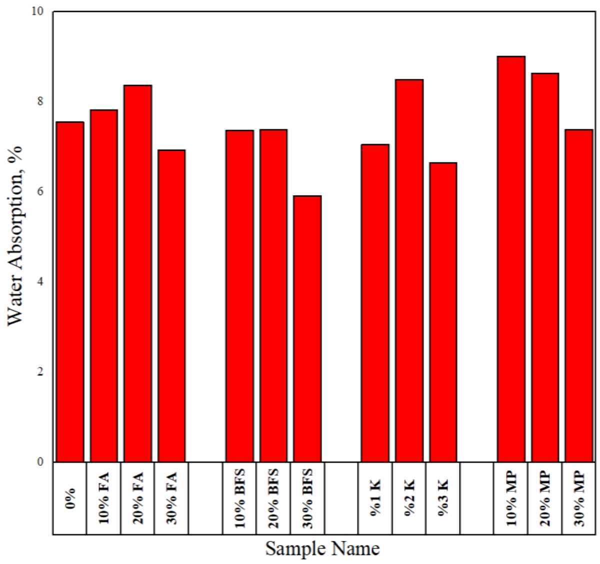

Figure 1. Water absorption values by weight (%)

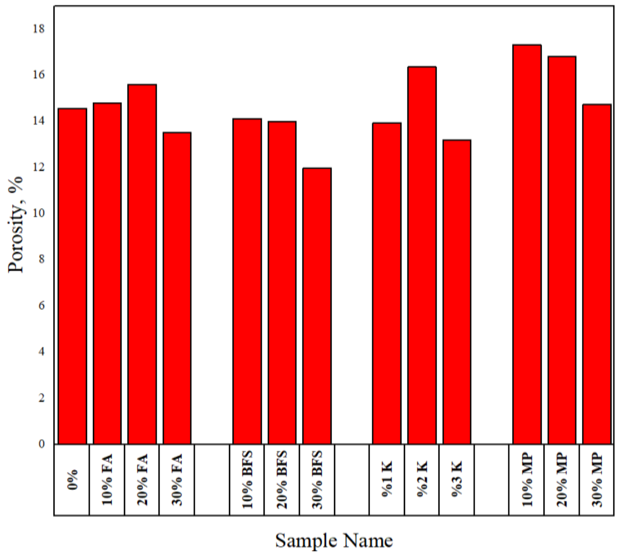

Figure 2. Porosity values by weight (%)

The compressive strengths of the mortar samples are given in Figure 3 and the flexural strengths are given in Figure 4. A decrease in compressive strength was observed in all mineral additive types except for mortar samples used by 10% of MT. With the increase in the rate of mineral additives, there was a decrease in compressive strength in general. However, in case of rising the FA rate to 20%, an increase in compressive strength is observed, while a 30% decrease is observed. 7-day compressive strength was observed in the reference sample with the highest 53.48 MPa, while the lowest with 39.93 MPa in case of using 30% BFS. The 28-day compressive strength was observed in the sample using the highest 62.15 MPa and 10% MP, while the lowest 30.50 MPa and 30% MP were used. In case the rate of MP increased from 10% to

30%, the compressive resistance decreased by approximately 50%. A decrease in flexural strength was observed in all mineral additive types except MP and FA's 10% used mortar samples. With the increase in the ratio of mineral additives, there was a general decrease in flexural strength. 7-day flexural strength was observed in the samples with the highest 6,99 MPa and 10% FA, while the lowest was 4.76 MPa and 30% MP. The 28-day flexural strength was observed in the sample with the highest 8.99 MPa and 1% K, while the lowest was 5.79 MPa and 30% MP.

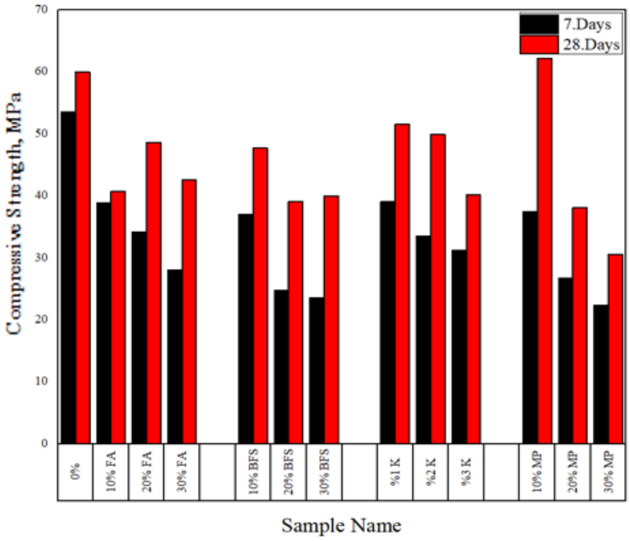

Figure 3. 7 and 28 days Compressive Strength of mortar samples

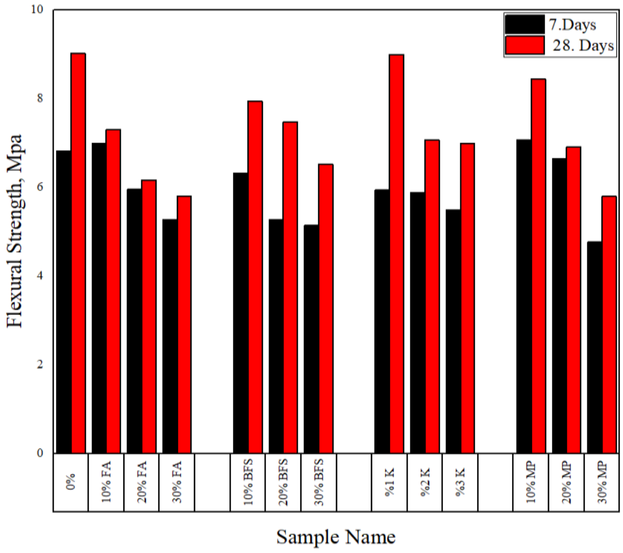

Figure 4. 7 and 28 days Flexural Strength of mortar samples

After applying high temperature, the weight losses of the samples were given in Figure 5. With the increase in temperature, weight losses have increased. With the use of mineral additives, weight losses after high temperature are decreased. The reference sample showed a 2.78% weight loss in 200°C, weight loss increased at 800°C, which increased to 8.52%.The lowest weight losses were observed in 200°C with a value of 1.14% for 10% MP-additive, 2.34% in 400°C and 30% MPa additive, 2.83% in 600°C and 3% K additive, 7.40% in 800°C and 30% MP additive. The highest weight loss at all temperature values was seen in reference samples.

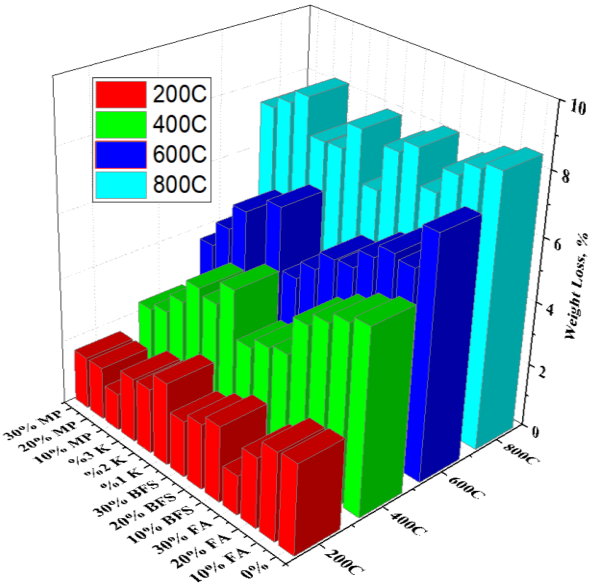

Figure 5. Weight loss before and after high temperature (%)

Compressive strengths of 28 days samples before and after temperatures are given in Figure 6 and flexural strengths are given in Figure 7. Along with the increase in temperature, Compressive and flexural strengths decreased in high rates. As the temperature increases more, the shrinkage that will occur with the loss of this water increases the strength of the concrete, and the vapor pressure that appears in the concrete may cause the concrete cover to crack and break off. Another component in the cement paste next to C-S-H is Ca(OH)2 (calcium hydroxide). The chemical water and gel water of C-S-H start to disappear from 300 °C and turn into CaO by losing $Ca(OH)_2$ water around 530 °C (Khoury 1996). Damages occurring at some temperatures cause the strength of concrete to decrease significantly (Poon et al. 2001).The flexural and compressive strength losses occurring in the reference sample for all temperatures are higher than the mortars that have mineral additives in mixture. It has been observed that with the use of mineral additives, mechanical losses caused by high temperature are reduced. When the compressive strengths are examined, a 78.68% reduction in compressive strength is observed in the reference sample with the temperature rising to 800 ^{0}C. The lowest compressive strength loss in FA mineral admixed mortars is 61.34% in FA use, 20% in BFS mineral admixture mortars, 57.87% in BFS use, 1% in K mineral admixture mortars, 60.26% in K use, and MP mineral admixture 63.2% of the mortars are used in 10% MP usage.

When the flexural strengths are examined, a 75.14% reduction in the compressive strength is observed with the temperature rising to 800 ^{0}C in the reference sample. The lowest flexural strength loss in FA mineral admixed mortars is 69.04% in 20% FA use, 20% in BFS mineral admixed mortars, 67.87% in BFS used, 61.9% in 1% use with K mineral admixture mortars, 61.9% in MP used and

56.2% occurred when the mortars are used in 10% MP used. It is observed that 20.81% decrease in flexural strength and 21.77% decrease in flexural strength occurred with the use of mineral additives. It has been observed that the use of mineral additives increases the resistance of mortars to high temperature.

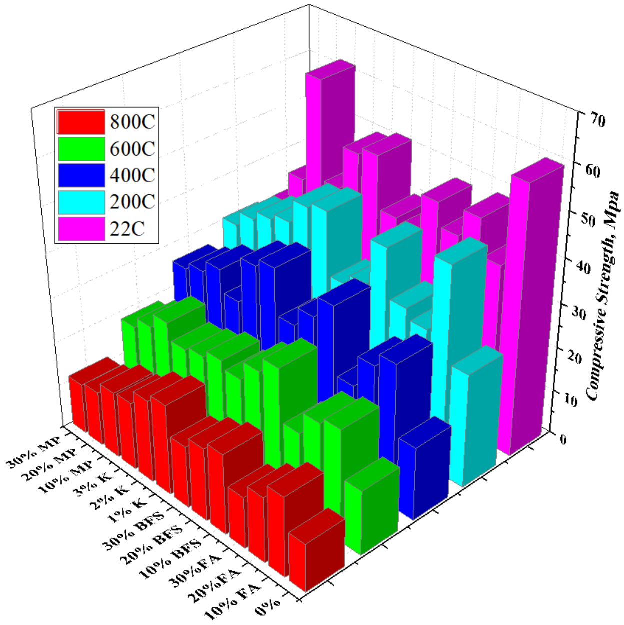

Figure 6. Compressive strengths before and after high temperature (MPa)

4. CONCLUSION

- A decrease in water absorption and porosity rates was observed in 30% of all mineral additives and in all ratios of K.
- The lowest water absorption value was obtained with the use of %30 BFS with a ratio of 5,91 % and the highest water absorption with the use of 10% MP with a ratio of 11,97%.
- The lowest porosity value was obtained with the use of 10% BFS with 11,97 % and the highest porosity with the use of %10 MP with 17,30%.
- With the increase of mineral additives in the mortar, the amount of fine material increases. The need for water increases as the surface area increases with the increase of the fine substance. Settlement difficulties due to the need for water reveals difficulties and causes it to settle more porous, in this case, it causes an increase in water absorption and porosity values.
- With the increase in the ratio of mineral additives, there was a general decrease in compressive and flexural strengths. However, when using MPE rate increase in the compressive strength observed at 10%, it was observed with increasing reduction rate of the MPA.
- 7-day flexural strength was observed in the sample with the highest 6,99 MPa and 10% FA, while the lowest was 4.76 MPa and 30% MP. The 28-day flexural strength was observed in the sample with the highest 8.99 MPa and 1% K, while the lowest was 5.79 MPa and 30% MP.
- It was observed that weight losses increased with increasing temperature. With the use of mineral additives, it is observed that weight losses decrease after temperature. The highest weight loss reference sample is seen for all temperatures.
- The lowest weight losses in mortars with 10% MP with a value of 1.14% at 200 ^{0}C, with a value of 2.34% at 400 ^{0}C and 30% with MP additive, 3% at 600 ^{0}C with a value of 2.83% It was observed in mortars with 30% MP additives with a value of 7.40% at 800 ^{0}C.
- With the increase of temperature, high rates of compressive and flexural strengths decreased. The flexural and compressive strength losses occurring in the reference sample for all temperatures are higher than the mortars that have in mineral additives in mixture. It has been observed that with the use of mineral additives, mechanical losses caused by high temperature are reduced.
- It is observed that with increasing temperature, weight loss increases, flexural and compressive strengths decrease in all samples. With the use of mineral additives, it was observed that both the weight losses and the losses in flexural and compressive strengths decreased and the mortars became more resistant to high temperature.

REFERENCES

Akca A H & Özyurt N (2018). Effects of re-curing on microstructure of concrete after high temperature exposure. Construction and Building Materials, 168, 431-441. DOI: 10.1016/j.conbuildmat.2018.02.122

Andrew R M (2018). Global CO$_2$ emissions from cement production. Earth System Science Data, 10(1), 195-217. DOI: 10.5194/essd-10-195-2018

Arioz O (2007). Effects of elevated temperatures on properties of concrete. Fire Safety Journal, 42(8), 516-522. DOI: 10.1016/j.firesaf.2007.01.003

Aydın S & Baradan B (2007). Effect of pumice and fly ash incorporation on high temperature resistance of cement based mortars. Cement and Concrete Research, 37(6), 988-995. DOI: 10.1016/j.cemconres.2007.02.005

Dimitriou G, Savva P & Petrou M F (2018). Enhancing mechanical and durability properties of recycled aggregate concrete. Construction and Building Materials, 158, 228-235. DOI: 10.1016/j.conbuildmat.2017.09.137

Gawin D, Pesavento F & Schrefler A (2004). Modelling of deformations of high strength concrete at elevated temperatures. Materials and Structures, 37, 218-236.

Heikal M, El-Didamony H, Sokkary T M & Ahmed I A (2013). Behavior of composite cement pastes containing microsilica and fly ash at elevated temperature. Construction and Building Materials, 38, 1180-1190. DOI: 10.1016/j.conbuildmat.2012.09.069

Huseien G F, Sam A R M, Shah K W, Mirza J & Tahir M M (2019). Evaluation of alkaliactivated mortars containing high volume waste ceramic powder and fly ash replacing GBFS. Construction and Building

Materials, 210, 78-92. DOI: 10.1016/j.conbuildmat.2019.03.194

Juan-Valdés A, Rodríguez-Robles D, García-González J, Guerra-Romero M I, Morán-del Pozo J M (2018). Mechanical and microstructural characterization of nonstructural precast concrete made with recycled mixed ceramic aggregates from construction and demolition wastes. Journal of Cleaner Production, 180, 482-493. DOI: 10.1016/j.jclepro.2018.01.191

Kermeli K, Edelenbosch O Y, Crijns-Graus W, Van Ruijven B J, Mima S, Van Vuuren D P & Worrell E (2019). The scope for better industry representation in longterm energy models: modeling the cement industry. Applied Energy, 240, 964-985. DOI: 10.1016/j.apenergy.2019.01.252

Khaliq W & Khan H A (2015). High temperature material properties of calcium aluminate cement concrete. Construction and Building Materials, 94, 475-487. DOI: 10.1016/j.conbuildmat.2015.07.023

Khoury G A (1996). Performance of Heated Concrete-Mechanical Properties. Contract NUC/56/3604A with Nuclear Installations Inspectorate, Imperial College, London, United Kingdom, August.

Li L, Wang Q, Zhang G, Shi L, Dong J, Jia P (2018). A method of detecting the cracks of concrete undergo high-temperature. Construction and Building Materials, 162, 345-358. DOI: 10.1016/j.conbuildmat.2017.12.010

Liang X, Wu C, Su Y, Chen Z & Li Z (2018). Development of ultra-high performance concrete with high fire resistance", Construction and Building Materials, 179, 400-412. DOI: 10.1016/j.conbuildmat.2018.05.241

Lin W M, Lin T D & Powers L J (1996). Microstructures of fire-damaged concrete. ACI Materials Journal, 93(3), 199-205.

Mendes A, Sanjayan J G & Collins F (2011). Effects of slag and cooling method on the progressive deterioration of concrete after exposure to elevated temperatures as in a fire event. Materials and Structures, 44, 709-718. DOI: 10.1617/s11527-010-9660-2

Mohammadhosseini H, Tahir M M & Sam A R M (2018). The feasibility of improving impact resistance and strength properties of sustainable concrete composites by adding waste metalized plastic fibres. Construction and Building Materials, 169, 223-236. DOI: 10.1016/j.conbuildmat.2018.02.210

Pan Z, Tao Z, Cao Y F, Wuhrer R & Murphy T (2018). Compressive strength and microstructure of alkali-activated fly ash/slag binders at high temperature. Cement and Concrete Composites, 86, 9-18. DOI: 10.1016/j.cemconcomp.2017.09.011

Poon C S, Azhar S, Anson M & Wong Y L (2001). Comparison of the strength and durability performance of normal- and high-strength pozzolanic concretes at elevated temperatures. Cement and Concrete Research, 31(9), 1291-1300. DOI: 10.1016/S0008-8846(01)00580-4

Seshu D R & Pratusha A (2013). Study on compressive strength behaviour of normal concrete and self-compacting concrete subjected to elevated temperatures. Magazine of Concrete Research, 65(7), 415-421. DOI: 10.1680/macr.12.00108

Tam V W Y, Soomro M & Evangelista A C J (2018). "A review of recycled aggregate in concrete applications (2000–2017). Construction and Building Materials, 172, 272-292. DOI: 10.1016/j.conbuildmat.2018.03.240

TS EN 1008 (2003). Mixing water for concrete - Specifications for sampling, testing and assessing the suitability of water, including water recovered from processes in the concrete industry, as mixing water for concrete. Turkish Standard Institute, Ankara Turkey.

TS EN 1170-6 (1999). Precast concrete products-test method for glass fibre reinforced cement-part 6: determination of the absorption of water by immersion and determination of the dry density. Turkish Standard Institute, Ankara, Turkey.

TS EN 12390-4 (2002). Testing hardened concrete - Part 4: Compressive strength - Specification for testing machines. Turkish Standard Institute, Ankara, Turkey.

TS EN 13501-1+A1 (2019). Fire classification of construction products and building elements - Part 1: Classification using data from reaction to fire tests. Turkish Standard Institute, Ankara, Turkey.

TS EN 196-1 (2016). Methods of testing cement - Part 1: Determination of strength. Turkish Standard Institute, Ankara, Turkey.

TS EN 197-1 (2012). Cement- Stage 1: General cements–component. Turkish Standard Institute, Ankara Turkey.

Yaşar E & Erdoğan Y (2005). Investigation of Engineering Properties of Building Materials Made With Acidic and Alcaline Pumic. Turkey 19. Uluslararant Mining Congress and Expo, 409-413.

Turkish Journal of Engineering

https://dergipark.org.tr/en/pub/tuje

e-ISSN 2587-1366

Electrospinning of Gelatin Nanofibers: Effect of gelatin concentration on chemical, morphological and degradation characteristics

Esra Ekiz [1], Didem Demir [1], Nimet Bölgen[1]

[1]*Mersin University, Engineering Faculty, Chemical Engineering Department, Mersin, Turkey*

Keywords
Gelatin
Electrospinning
Nanofiber
Scaffold
Tissue engineering

ABSTRACT

Electrospinning is a well-known technique that produces polymeric nanofibers using an electrically driven jet of a polymer solution. Due to unique properties such as high surface area, porosity, tensile strength and extensibility of the materials produced by electrospinning, several applications of them in protective clothing, space technology, filtration and tissue engineering have been proposed and investigated. In this study; we prepared gelatin nanofibrous scaffolds by using the electrospinning method for tissue engineering applications. The beads-free, smooth and uniform gelatin nanofibers were successfully fabricated. The blend solutions at different weight ratios were prepared by dissolving gelatin in a solvent mixture containing formic acid, dichloromethane and acetic acid. The fabricated nanofibers were chemically crosslinked by glutaraldehyde vapor. The crosslinked nanofibrous scaffolds were characterized by chemical and morphological analysis. The morphology and size distribution curves of nanofibers were determined by Scanning electron microscopy (SEM). The chemical structure of nanofibers was investigated by Fourier transform infrared spectroscopy (FTIR) analysis. The strategy based on electrospinning of gelatin nanofibers can be used to develop new biomimetic materials for tissue engineering applications.

1. INTRODUCTION

Tissue engineering/regenerative medicine is an emerging and interdisciplinary field that aims to maintain, improve or restore damaged tissues or whole organs using a combination of cells, scaffolds and bioactive molecules with the principles of biology, materials science and engineering (Langer and Vacanti 1993). The tissue engineering strategy includes the use of three-dimensional (3D) scaffold materials to provide a suitable microenvironment for the regeneration of tissues and organs (O'Brien 2011). The scaffolds seeded with cells assist a 3D support for cell migration, attachment and proliferation by mimicking the features of native extracellular matrix (ECM) architecture (Wang et al. 2013). The ECM in tissues and organs provides a physicochemical environment for cells and bioactive agents required for tissue morphogenesis, differentiation and homeostasis (Wu et al. 2014). Hence, the ideal scaffold should possess a similar structure to ECM.

Scaffolds can be manufactured from metals, polymers, ceramics or composite biomaterials to simulate the properties of tissues and organs. In addition, different techniques have been used to fabricate various types of scaffolds such as electrospinning (Chahal et al. 2015), freeze-drying (Al-Munajjed et al. 2009), casting/solvent evaporation (Liao and Ho 2010), foam replication technique (Reiter et al. 2019) and 3D printing (Soundrapandian et al. 2010). Among them, electrospinning is a well-known, attractive and simple technique for processing polymers into fibers with diameters ranging from several nanometers to a few micrometers (Demir et al. 2018). Electrospun nanofibrous 3D scaffolds have attracted great interest in the field of tissue engineering mainly due to their large surface area-to-volume ratio, high porosity, mechanical properties and morphology similar to the ECM of natural tissues.

A variety of natural and synthetic polymers has been used to fabricate the electrospun scaffolds. In this study, the composition of the electrospun scaffold is designed to

---

* **Corresponding Author**

*(esrayikar@hotmail.com) ORCID ID 0000 – 0002 – 8198 – 8078
(didemdemr@gmail.com) ORCID ID 0000 – 0002 – 2977 – 2077
(nimetbolgen@yahoo.com) ORCID ID 0000 – 0003 – 3162 – 0803

Cite this article

Ekiz E, Demir D & Bölgen N (2021). Electrospinning of Gelatin Nanofibers: Effect of gelatin concentration on chemical, morphological and degradation characteristics. Turkish Journal of Engineering, 5(4), 171-176

Research Article / DOI: XXXXXXXXXXXX

Received: 16/03/2020; Accepted: 11/06/2020

simulate the natural tissue. Thus, gelatin, as a natural polymer, which is a denatured form of collagen, was selected for the preparation of nanofibers (Echave et al. 2017). Gelatin is an excellent material for tissue engineering applications due to its unique features such as biodegradability, biocompatibility, promoting cell adhesion and proliferation, and low immunogenicity (Tondera et al. 2016; Echave et al. 2017). Therefore, the use of gelatin as a natural polymer in tissue engineering has attracted many interests and is also widely used in clinics as wound dressings, pharmaceuticals and adhesives (Maleknia and Majdi 2014). Electrospinning is an attractive option for fabricating gelatin nanofibrous scaffolds in high surface area, physically stable and controllable thickness in different forms including thick nanofiber sheet (Huang et al. 2004) and tubular structure (Shalumon et al. 2015). Previous studies showed that electrospun gelatin scaffolds were biocompatible and have been used in a variety of biomedical applications such as bone tissue engineering (Meng et al. 2013), wound healing (Yao et al. 2017) and drug delivery (Kamble et al. 2018).

In this study, we produced nanofibrous scaffolds with different weight ratios of gelatin via electrospinning and revealed the effect of gelatin concentration on chemical, morphological and degradation properties. Gelatin scaffolds prepared by electrospinning were crosslinked by glutaraldehyde vapor for stability in aqueous media and mechanical strength. The morphological observations of nanofibers before and after crosslinking were studied in detail using Scanning electron microscopy (SEM). The fiber size distributions and average fiber diameters of nanofibers were determined. The chemical composition and molecular bonds of the scaffolds were analyzed by Fourier Transform Infrared Spectroscopy (FTIR). Degradation of electrospun scaffolds was studied gravimetrically. The findings of this study showed that morphological structure and degradation profile of gelatin nanofibers can be adjusted by changing the polymer concentration in the initial electrospinning solution. The nanofibrous scaffolds could be used as biomaterials for potential tissue engineering applications.

2. MATERIALS AND METHODS

2.1. Reagents

Gelatin as a natural polymer and glutaraldehyde solution (25%, v/v) as a crosslinking agent were received from Merck, Germany. Glacial acetic acid (100%, v/v) as a solvent was obtained from Sigma-Aldrich, USA. Formic acid and dichloromethane as solvents were purchased from PanReac (Spain) and Carlo Erba Reagents (France), respectively. All the chemicals were used as received.

2.2. Electrospinning of gelatin nanofibers

The electrospinning apparatus consists of a high voltage power supply (Gamma High Voltage, ES40P, USA), a syringe pump (New Era, NE-300), a 2.5 ml of a plastic syringe, a stainless steel needle connected to the power supply electrode and a grounded collector. A vertically positioned metal sheet covered with aluminum foil was used as the collector. Solutions with concentrations of 15, 20, 25 and 30% (w/v) (15% Gel, 20% Gel, 25%Gel, 30% Gel) were prepared by dissolving gelatin in a solvent mixture containing formic acid, dichloromethane and acetic acid with a volumetric ratio of 70:20:10, respectively. The prepared solutions were loaded into a 2.5 ml syringe with a stainless steel needle and 13 kV voltage was applied to the solutions. The tip-to-collector distance was 10 cm. The feeding rate of the gelatin solutions was 0.3 ml/h. The schematic illustration of electrospinning set-up is demonstrated in Figure 1A.

2.3. Crosslinking of Electrospun Nanofibers

To prevent the dissolution of the electrospun nanofibers, the prepared scaffolds were crosslinked under glutaraldehyde vapor in a glass chamber for 3 days as illustrated in Figure 1B. The crosslinked electrospun nanofibrous materials were called 15% Gel-GA, 20% Gel-GA, 25% Gel-GA and 30% Gel-GA. The reaction scheme between gelatin and glutaraldehyde is also reported in Figure 1B.

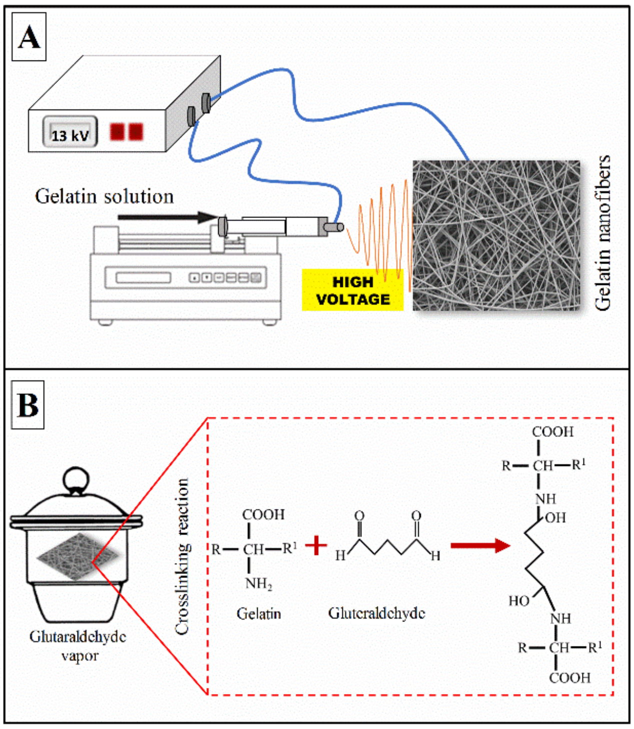

Figure 1. A) The schematic illustration of the electrospinning set-up and B) reaction mechanism of crosslinking between gelatin and glutaraldehyde

2.4. Characterization studies of the electrospun nanofibers

FTIR spectrometer (Perkin-Elmer Spectrum 1000, USA) was used to determine the chemical compositions of the produced materials. The spectra in the range of 475-4000 cm^{-1} with automatic signal gain were collected in 10 scans at a resolution of 4 cm^{-1}.

The morphology of the nanofibrous structure of the scaffolds before and after crosslinking was investigated by SEM (SEM, Quanta 400F Field Emission, Supra 55, Zeiss) at an accelerating voltage of 5 kV. The specimens were coated with platinum using a sputter coater before SEM analysis.

The fiber diameters of the nanofibers were identified from SEM images by using Lucia 32G image analysis software. The average nanofiber diameter was calculated by measuring the diameter of 80 nanofibers. The fiber size distribution curve of scaffolds was created using a histogram graph in OriginPro.

The *in-vitro* degradation studies of electrospun nanofibrous scaffolds after crosslinking with glutaraldehyde were performed by first recording the initial dry weight of the scaffolds. Then the samples were transferred to the falcon tubes filled with distilled water. The tubes were placed into a shaking water bath (Daihan Scientific Co. Ltd., WiseBath WB-22, Korea) at 37°C. At pre-determined time intervals (1, 6, 12, 18 and 21 days), samples were withdrawn, dried and weighed. Each value was the average of the result of three parallel measurements. The percentage of degradation (D, %) was calculated by the following Eq. (1):

$$D, \% = \frac{(Mi - Mt)}{Mi} \times 100 \qquad (1)$$

where Mi is the initial dry weight of samples, Mt is the final dry weight at pre-determined time intervals.

The degradation data were analyzed by using analysis of variance, ANOVA, by Origin Pro 2016 software and expressed as mean value and standard deviation, compared using the Tukey test. Differences were considered statistically significant at ($p<0.05$).

3. RESULTS AND DISCUSSION

3.1. Chemical structure of the electrospun nanofibers before and after crosslinking

The produced gelatin nanofiber scaffolds can easily dissolve or lose their fibrous structure when coming into contact with an aqueous medium or exposure to high ambient humidity because of the water solubility of gelatin (Oraby et al. 2013). The crosslinking of these nanofibers is necessary to extend their use in various applications. Glutaraldehyde is the most frequently used crosslinking agent which is a bifunctional, water-soluble and economical crosslinker to resist both enzymatic degradation and hydrolysis of gelatin nanofibers (Lee et al. 2017). Therefore, the samples were chemically crosslinked under vapor of glutaraldehyde solution (Figure 1B). The crosslinking mechanism between gelatin and glutaraldehyde can be explained by the reaction of the aldehyde groups of glutaraldehyde with nonprotonated ε-amino groups ($-NH_2$) of lysine or hydroxylysine amino acids present in gelatin (Farris et al. 2010).

To compare the change in the chemical structure before and after crosslinking, the FTIR spectrum of nanofibers was provided. The FTIR spectra of gelatin nanofibers fabricated at 15, 20, 25 and 30% concentration (labeled as 15% Gel, 20% Gel, 25% Gel and 30% Gel, respectively) is shown in Figure 2A. After crosslinking, the samples were named 15% Gel-GA, 20% Gel-GA, 25% Gel-GA and 30% Gel-GA, respectively and their spectra is presented in Figure 2B.

As can be seen, all spectra are similar and exhibit the characteristic peaks of gelatin. The typical bands of gelatin are Amides I (C-O stretching at 1650 cm-1), Amides II (N=H bending at 1540 cm-1) and Amides III (N=H bending at 1235 cm-1) and their intensity were observed relatively decreasing after crosslinking (Erencia et al. 2015).

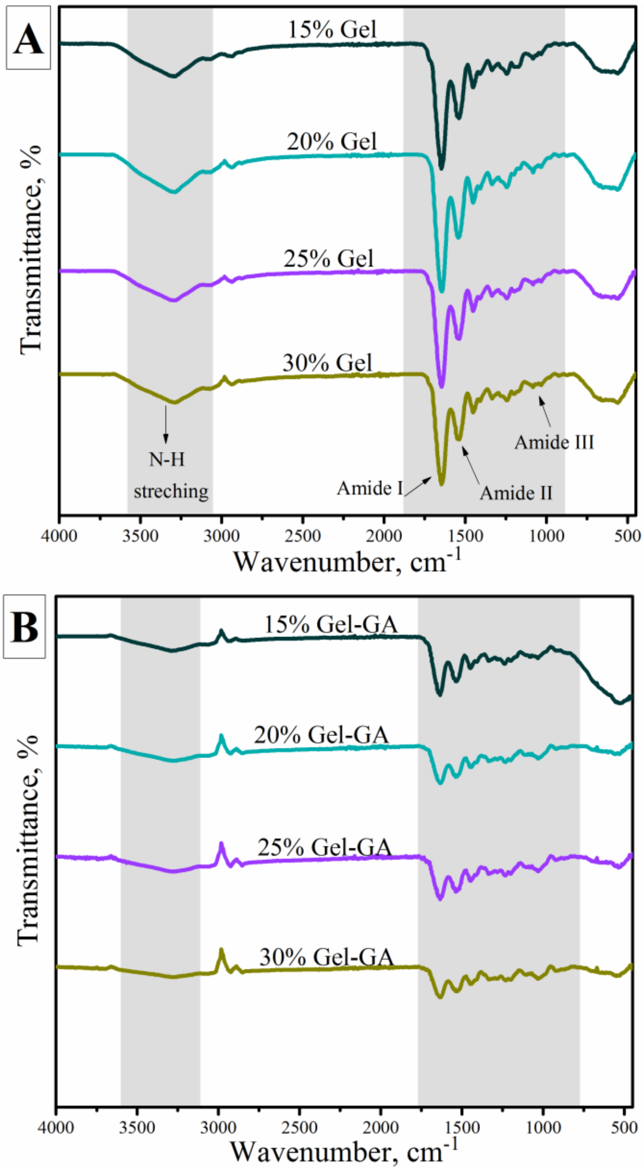

Figure 2. The FTIR spectrum of nanofibers before and after crosslinking with glutaraldehyde

3.2. Morphological observations of the electrospun nanofibers before and after crosslinking

Beads-free and smooth gelatin nanofibrous scaffolds were fabricated by electrospinning. The SEM images at different magnifications (700KX and 6000KX) and fiber size distribution curves of the electrospun scaffolds which were fabricated from different concentrations of gelatin solutions (15, 20, 25 and 30%, w/v) are presented in Figure 3 and Figure 4, respectively. From the SEM images in Figure 3, it is clearly observed that beads-free and uniform nanofibers were produced with an average diameter ranging from 142.47 to 451.64 nm. The average fiber diameters of the scaffolds were significantly different from each other because of the increased gelatin concentration.

With increasing the polymer concentration, fibers with larger diameters were obtained due to the increase in viscosity of the gelatin solution (Soundrapandian et al. 2010). In addition to fiber diameter, the size of the pores between fibers has an important role in the ability of the cells to infiltrate into the electrospun scaffold. It was observed that the porosity of the electrospun gelatin scaffold changed depending on the fiber diameter. Lower pore size was obtained in scaffolds with smaller sized fiber diameters.

The effect of concentration on the diameter of gelatin nanofibers can also be examined from the fiber diameter distributions showed in Figure 4A, B, C and D.

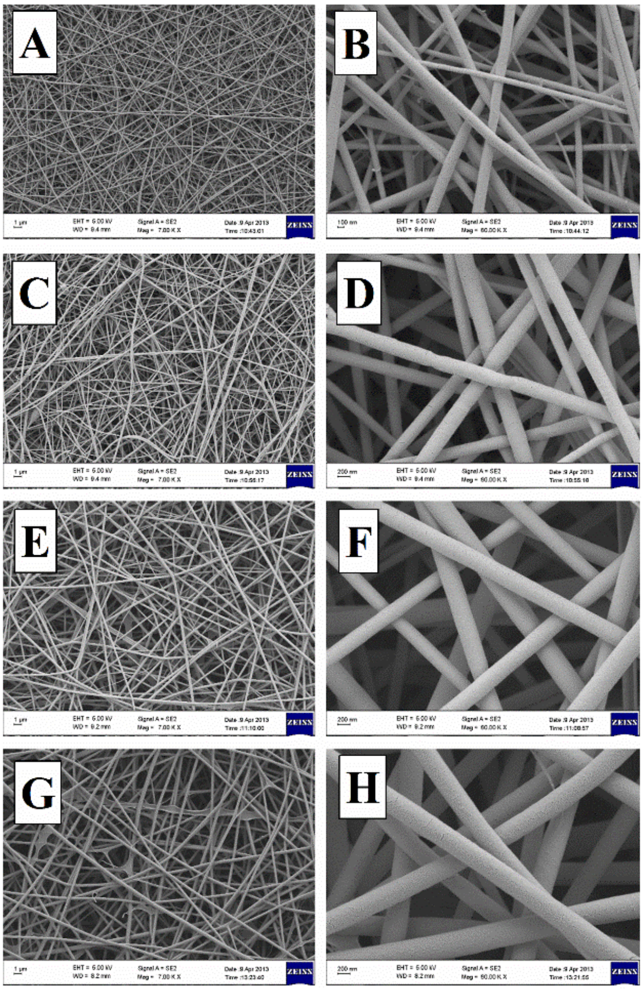

Figure 3. SEM microphotographs of electrospun gelatin scaffolds before crosslinking with glutaraldehyde. A, B: 15% Gel; C, D: 20% Gel; E, F: 25% Gel and G, H: 30% Gel

The morphology of the crosslinked nanofibers at different gelatin concentrations with a constant amount of glutaraldehyde are shown in Figure 5. Compared with Figure 3, although the nanofibrous form had been completely preserved for all samples, the pore size of the scaffolds formed between nanofibers was changed due to the junctions at connection points of nanofibers. This can be explained by the partial dissolution of gelatin fiber segments due to the interaction of water molecules in glutaraldehyde vapor (Laha et al. 2016).

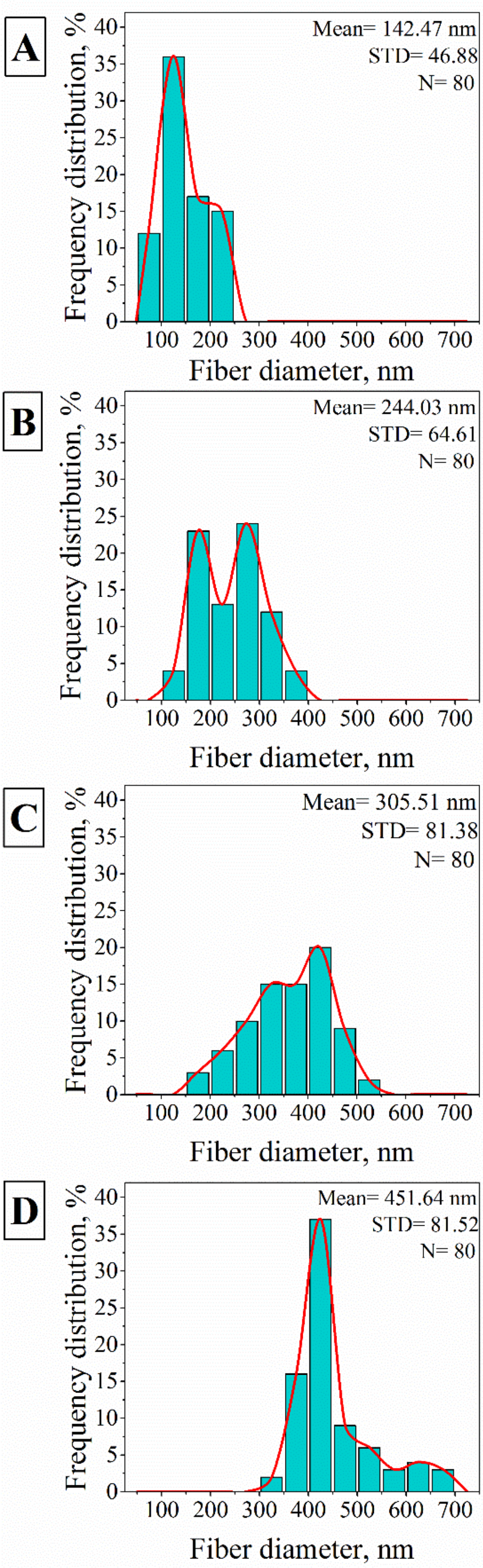

Figure 4. Fiber size distribution curves of electrospun gelatin scaffolds before crosslinking with glutaraldehyde. A: 15% Gel; B: 20% Gel; C: 25% Gel and D: 30% Gel

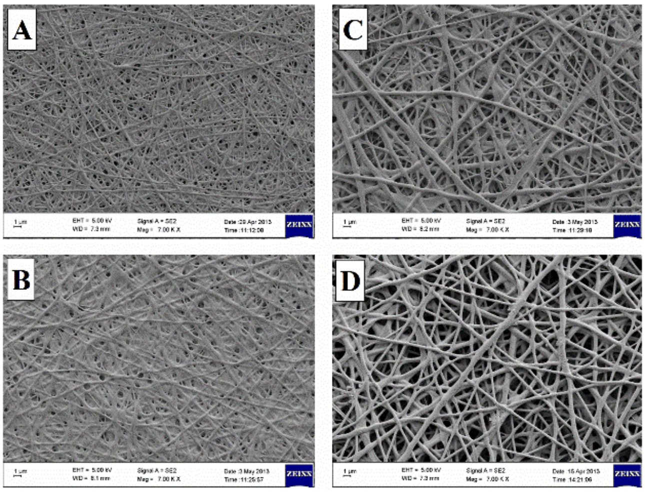

Figure 5. SEM microphotographs of electrospun gelatin scaffolds after crosslinking with glutaraldehyde. A: 15% Gel-GA; B: 20% Gel-GA; C: 25% Gel-GA and D: 30% Gel-GA

3.3. Degradation studies of nanofibers after crosslinking with glutaraldehyde

The degradation profile of the scaffolds is a crucial factor for tissue engineering applications. The degradation of the electrospun gelatin scaffolds after crosslinking was determined by gravimetric analysis as seen in Figure 6. These studies were performed in order to simulate degradation behavior of the fibrous scaffolds *in-vitro*. According to the examined degradation results, it is observed that as the gelatin concentration increases, the degradation decreases. 30% Gel-GA nanofibrous scaffold incubated for 21 days did not lose much mass, indicating minimal solubilization of the nanofibers in the distilled water over the time of the experiment. This can be explained by the increasing fiber diameter with increasing gelatin concentration. As the nanofiber diameter increased, the total surface area decreased and as a result, the degradation also decreased. When nanofibers prepared in low gelatin concentration are examined, it is seen that the degradation increases with decreasing gelatin concentration. The significant differences are found in the degradation between the low (15% Gel) and high (30% Gel) concentrations of nanofibrous scaffolds ($p<0.05$). The reason for the fast degradation of 15% Gel scaffold could be that the thin nanofibers have a higher ratio of surface-to-volume than fibers with larger dimensions. Similarly, Jeong et al. 2005 showed that the degradation of electrospun poly (butylene succinate) fibers was faster for ultrafine fiber diameters. In addition, the weight loss of the scaffolds increased with increasing incubation time.

4. CONCLUSIONS

Electrospinning is an efficient method to fabricate nano-sized fibers from both natural and synthetic polymers for tissue engineering applications. In this study, we electrospun nanofibrous scaffolds from different amounts of gelatin as a natural polymer. The beads free and smooth nanofibers were successfully fabricated. The nanofibers were then crosslinked with glutaraldehyde vapor to prevent the dissolution of scaffolds in aqueous media. The fabricated scaffolds before and after crosslinking were characterized by chemical and morphological analyzes. The morphological structure of the nanofibers changed depending on the gelatin ratio. The fabricated gelatin scaffolds have the potential to have wide applicability in a large number of tissue engineering applications due to their high surface area.

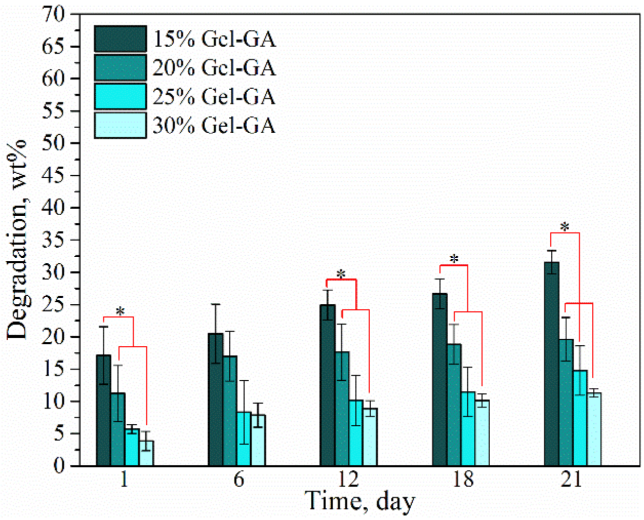

Figure 6. The degradation profile of the crosslinked gelatin nanofibers. (n=3). Data are presented as mean=SD. *$p<0.05$ compared to cryogels by days with an increase in gelatin concentration

ACKNOWLEDGEMENT

This work was supported by the Scientific Research Projects Unit of Mersin University (BAP FBE KM (EY) 2011-4 YL). On behalf of all authors, the corresponding author states that there is no conflict of interest.

REFERENCES

Al-Munajjed A A, Plunkett N A, Gleeson J P, Weber T, Jungreuthmayer C, Levingstone T, Hammer J & O'Brien F J (2009). Development of a biomimetic collagen-hydroxyapatite scaffold for bone tissue engineering using a SBF immersion technique. Journal of Biomedical Materials Research - Part B: Applied Biomaterials, 90(2), 584–591.

Chahal S, Jahir Hussain F S, Kumar A, Yusoff M M, Rasad, M S B A (2015). Electrospun hydroxyethyl cellulose nanofibers functionalized with calcium phosphate coating for bone tissue engineering. RSC Advances, 5(37), 29497–29504.

Demir D, Güreş D, Tecim T, Genç R, Bölgen N (2018). Magnetic nanoparticle-loaded electrospun poly (ε-caprolactone) nanofibers for drug delivery applications. Applied Nanoscience, 8, 1461–1469.

Echave M C, Burgo L S, Pedraz J L, Orive G (2017). Gelatin as biomaterial for tissue engineering. Current Pharmaceutical Design, 23(24), 3567–3584.

Erencia M, Cano F, Tornero J A, Fernandes M M, Tzanov T, Macanás J & Carrillo F (2015). Electrospinning of gelatin fibers using solutions with low acetic acid concentration: Effect of solvent composition on both diameter of electrospun fibers and cytotoxicity. Journal of Applied Polymer Science, 132, 1–11.

Farris S, Song J & Huang Q (2010). Alternative reaction mechanism for the cross-linking of gelatin with glutaraldehyde. Journal of Agricultural and Food Chemistry, 58(2), 998–1003. DOI: 10.1021/jf9031603

Huang Z M, Zhang Y Z, Ramakrishna S, Lim C T (2004). Electrospinning and mechanical characterization of gelatin nanofibers. Polymer, 45(15), 5361–5368. DOI: 10.1016/j.polymer.2004.04.005

Jeong E H, Im S S & Youk J H (2005). Electrospinning and structural characterization of ultrafinepoly (butylene succinate) fibers. Polymer, 46(23), 9538–9543. DOI: 10.1016/j.polymer.2005.07.100

Kamble A, Shetty V, Shendokar S M, Chavan S S & Kaul-Ghanekar R (2018). Synthesis, characterization and antibacterial activity of ciprofloxacin loaded electrospun gelatin nanofibers. Journal of Bionanoscience, 12(5), 715-720. DOI: 10.1166/jbns.2018.1574

Laha A, Yadav S, Majumdar S, Sharma C S (2016). In-vitro release study of hydrophobic drug using electrospun cross-linked gelatin nanofibers. Biochemical Engineering Journal, 105, 481–488. DOI: 10.1016/j.bej.2015.11.001

Langer R & Vacanti J P (1993). Tissue engineering. Science, 260(5110), 920–926.

Lee J B, Ko Y G, Cho D, Park W H & Kwon O H (2017). Modification and optimization of electrospun gelatin sheets by electronbeam irradiation for soft tissue engineering. Biomaterials Research, 21, 1–9. DOI: 10.1186/s40824-017-0100-z

Liao C-T & Ho M-H (2010). The fabrication of biomimetic chitosan scaffolds by using sbf treatment with different crosslinking agents. Membranes, 1(1), 3–12. DOI: 10.3390/membranes1010003

Maleknia L & Majdi Z R (2014). Electrospinning of gelatin nanofiber for biomedical application. Oriental Journal of Chemistry, 30(4), 2043–2048.

Meng Z X, Li H F, Sun Z Z, Zheng W & Zheng Y F (2013). Fabrication of mineralized electrospun PLGA and PLGA/gelatin nanofibers and their potential in bone tissue engineering. Materials Science and Engineering C, 33(1), 699-706. DOI: 10.1016/j.msec.2012.10.021

O'Brien F J (2011). Biomaterials and scaffolds for tissue engineering. Materials Today, 14(3), 88–95. DOI: 10.1016/S1369-7021(11)70058-X

Oraby M A, Waley A I, El-dewany A I, Saad E A, El-hady, M. A. (2013). Electrospun gelatin nanofibers : effect of gelatin concentration on morphology and fiber diameters. Journal of Applied Sciences Research, 9(1), 534–540.

Reiter T, Panick T, Schuhladen K, Roether J A, Hum J, Boccaccini A R (2019). Bioactive glass based scaffolds coated with gelatin for the sustained release of icariin. Bioactive Materials, 4(1), 1–7. DOI: 10.1016/j.bioactmat.2018.10.001

Shalumon K T, Deepthi S, Anupama M S, Nair S V, Jayakumar R & Chennazhi K P (2015). Fabrication of poly (l-lactic acid)/gelatin composite tubular scaffolds for vascular tissue engineering. International Journal of Biological Macromolecules, 72, 1048-1055. DOI: 10.1016/j.ijbiomac.2014.09.058

Soundrapandian C, Datta S, Kundu B, Basu D & Sa B (2010). Porous bioactive glass scaffolds for local drug delivery in osteomyelitis: development and in vitro characterization. AAPS PharmSciTech, 11(4), 1675–1683. DOI: 10.1208/s12249-010-9550-5

Tondera C, Hauser S, Krüger-Genge A, Jung F, Neffe A T, Lendlein A, Klopfleisch R, Steinbach J, Neuber C, Pietzsch J & Dresden-Rossendorf H-Z (2016). Gelatin-based hydrogel degradation and tissue interaction in vivo: insights from multimodal preclinical imaging in immunocompetent nude mice. Theranostics, 6(12), 2114–2128. DOI: 10.7150/thno.16614

Wang X, Ding B & Li B (2013). Biomimetic electrospun nanofibrous structures for tissue engineering. Materials Today, 16, 229–241. DOI: 10.1016/j.mattod.2013.06.005

Wu S, Liu X, Yeung K W K, Liu C & Yang X (2014). Biomimetic porous scaffolds for bone tissue engineering. Materials Science and Engineering: R: Reports, 80, 1–36. DOI: 10.1016/j.mser.2014.04.001

Yao C H, Yeh J Y, Chen Y S, Li M H & Huang C H (2017). Wound-healing effect of electrospun gelatin nanofibres containing Centella asiatica extract in a rat model. Journal of Tissue Engineering and Regenerative Medicine, 11(3), 905-915. DOI: 10.1002/term.1992

Turkish Journal of Engineering – 2021; 5(4); 177-182

Turkish Journal of Engineering

https://dergipark.org.tr/en/pub/tuje

e-ISSN 2587-1366

Research on A1 irregularity status in different spectral acceleration coefficients on reinforced concrete structures

Abdülkerim İlgün [1], **Ahmet Mesut Yorulmaz** *[2]

[1]*Kto Karatay University, Faculty of Engineering, Department of Civil Engineering, Konya, Turkey*
[2]*Konya Technical University, Faculty of Engineering, Department of Civil Engineering, Konya, Turkey*

Keywords
Torsional irregularity
Reinforced concrete structure
Structural behavior
Geometric form

ABSTRACT

Most of the building damages in our country are caused by earthquakes. As known, the properties of the building are determinant in the magnitude of the earthquake forces that cause these damages. Thus, selection of the structural system is crucial in the design process. In case of any irregularity in the building, load transfer will not be provided safely. In the Turkish Earthquake Code, related irregularities are analysed under two groups. Group A indicates the irregularities in the plan, and Group B represents vertical irregularities. Irregularities in the plan include A1 Torsional Irregularities; A2 Floor Discontinuities; and A3 Bulges in the Plan. In this study, A1 irregularity status in the reinforced concrete structure was analysed for different spectral acceleration coefficients. The purpose of the study is to understand the change of torsional irregularity coefficient in different spectral acceleration coefficients. As a result, in a typical building with the same geometric and stiffness properties, the torsional irregularity coefficient is not changed for different earthquake zones. Also, the importance of the location of the shear wall elements in the plan was once again emphasized.

1. INTRODUCTION

In general, the construction is designed considering the necessity of being economical, aesthetic, and safe. Therefore, it is more important than other issues to ensure the safety of the structure, that is, to provide reliability in the event of collapse, except for displacement and section cracks under the characteristic loads. Such displacements are manifested by inertial forces in the event of an earthquake. All this led to the development of contemporary earthquake regulations. In general, all International earthquake regulations are aimed at ensuring that the structure can easily be repaired in relatively less severe earthquakes and that the structure does not collapse in severe earthquakes and that there is no loss of life.

One of the most striking issues in regulations is Torsional Irregularity. The relevant regulations have brought some limitations to irregularities. These are issues such as increasing eccentricity or performing dynamic analysis if the specified limits are exceeded.

(Yön and Sayın 2009) in order to examine the changes in the total torsional moment of different floor classes in a structure with torsional irregularity, a multi-storey reinforced concrete building with shear wall-frame according to the torsional irregularity specified in the Turkish Earthquake Regulation (TDY-2007) was designed and the results of the analysis were evaluated.

(Erdem 2016) in case construction's structural systems are not selected in line with the principles of earthquake-resistant structural systems selection, the impacts of torsional irregularities caused by not having overlapped the mass and stiffness of the structures are analyzed by changing the column sizes and forming structural systems with different eccentricity and stiffness.

(Özmen 2004), analyzed the conditions required for the torsional irregularity coefficient to exceed the upper limit of 2.00 using a parametric research method, 8 typical building groups with shear walls in different positions were selected and their behaviors under earthquake loads were evaluated.

(Demir and Dönmez 2008), factors affecting torsional irregularities, according to the conditions of the "Regulation on Buildings to be Made in Earthquake Zones", of six types of structures with different

---

* **Corresponding Author**

(kerim.ilgun@karatay.edu.tr) ORCID ID 0000 – 0002 – 9784 – 460X
*(mstyrlmz@hotmail.com) ORCID ID 0000 – 0001 – 7155 – 3399

Cite this article

İlgün A & Yorulmaz A M (2021). Research on A1 irregularity status in different spectral acceleration coefficients on reinforced concrete structures. Turkish Journal of Engineering, 5(4), 177-182

Research Article / DOI: XXXXXXXXXXXX

Received: xx/xx/xxxx; Accepted: xx/xx/xxxx

geometrical plans and shear wall layouts and four local floor classes were examined.

(Özmen 2012), in order to examine the validity of the torsional irregularity coefficients in regulations, six groups of typical structures with different shear wall positions were selected. The number of axles for these structures was changed between 5, 6 and 7, and the number of floors was changed between 1, 2, 4, 6, 8 and 10, and the variation of the torsional irregularity coefficients was examined.

(Doğan and Er 2010) torsional irregularity changes, due to the live load distribution is not evenly spread in the floor plane in residential buildings, were analysed.

(Demir et al. 2011), analysed the change in torsional behaviour of different floor classes of an existing reinforced concrete hospital building with the Equivalent Earthquake Load, Mode Combination and Calculation in Time history methods mentioned in Turkish Earthquake Regulation-2007 for four different local floor classes and studied the effect of scaled earthquake records on various behaviours of the building.

(Özmen 2001), in order to ensure that there is no geometrical irregularity effect, rectangle plan geometry was selected and analysed in all typical structures with regular and irregular stiffness distribution where earthquake calculation and dimension results are dealt with.

Döndüren et al. 2007, torsional irregularity conditions in symmetrical and non-symmetrical structures in terms of plan geometry and stiffness distribution and their behaviours under earthquake effects were analysed considering multi-storey structures in seven different types with 15-storey triangle, ellipse, square, rectangle, circular, L and T-shaped geometry.

(Soyluk and Yavuz 2009) (Özmen 2000) analysed the impact of plan geometry on torsional irregularity. (Özmen 2000) analysed the impact of plan geometry on torsional irregularity. (Uçar and Merter 2009) analyzed the impact of shear wall placement on the earthquake behaviour of the reinforced shear wall-framed buildings by considering torsional irregularity coefficients.

(Yorulmaz 2018), in his master thesis study, analyzed the change of the torsional irregularity coefficient for different earthquake zones in reinforced concrete structures according to TDY-2007 and as a conclusion, it was shown that the differentiation of the earthquake zones did not change the torsional irregularity coefficient.

2. A1 TORSİONAL IRREGULARITY

Torsional Irregularity, for any of the two earthquake directions perpendicular to each other in TBDY-2018, is expressed as the ratio of the largest relative floor displacement in any floor to the average relative displacement in that direction.

With a simple approach, designing buildings solely according to earthquake forces does not fully serve the purpose. The irregularities in the plan of the structure create additional torsional moments. This is shown in Figure 1 and Figure 2 below.

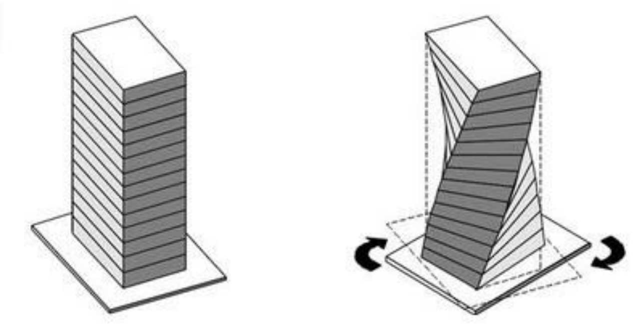

Figure 1. Representation of the torsional moment in the structure

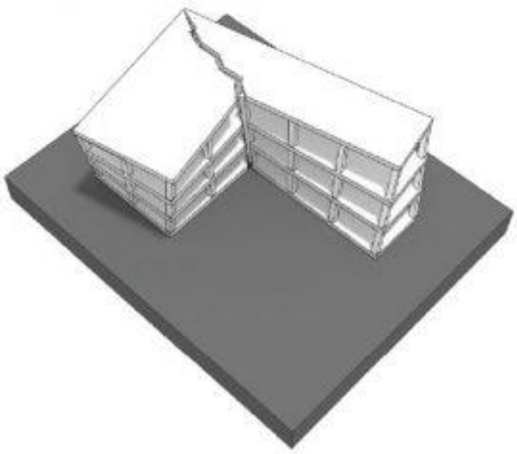

Figure 2. Representation of the torsional moment in the structure

2.1. Torsional Irregularity Calculation

Inertial forces occurring during the earthquake affecting the structure's centre of gravity. The structure tries to spin around the stiffness centre. Since the centre of gravity and stiffness do not coincide, a torsional moment occurs in the structure (Figure 3). Therefore, the stiffness centres of shear walls and columns, which are among the elements with relatively high stiffness, should be positioned as close to the centre of gravity of structure as possible. Especially, shear wall elements should be positioned outside the structure.

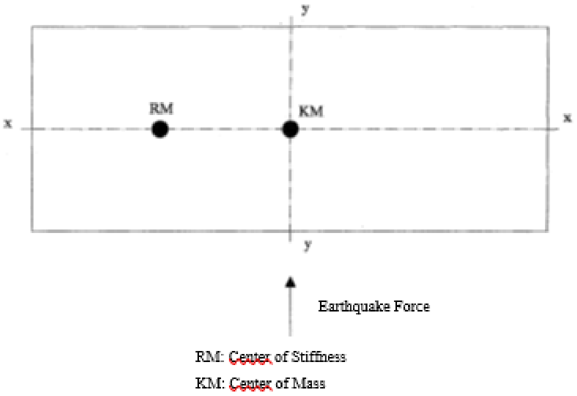

Figure 3. Representation of stiffness centre and mass centre

When international earthquake regulations are analysed, it is seen that one of the most frequently considered irregularity is Torsional Irregularity. Torsional irregularity depends on the torsional irregularity coefficient calculated as the ratio of maximum relative displacement to the average relative displacement of the floor under consideration.

For any of the two earthquake directions perpendicular to each other in TBDY-2018, the Torsional Irregularity Coefficient η_{bi} which represent the ratio of the largest relative floor displacement in one floor to the average relative displacement in that same direction is greater than 1.2 torsional irregularity should be taken into consideration.

$$\eta bi=(\Delta_i)_{max}/(\Delta_i)_{ort>1.2} \quad (1)$$

$$(\Delta_i)_{max=}(d_i)_{max\text{-}}(d_i\text{-}1)_{max} \quad (2)$$

$$(\Delta_i)_{min} = (d_i)_{min} - (d_i\text{-}1)_{min} \quad (3)$$

$$(\Delta_i)_{ort} = ((\Delta_i)_{max}+(\Delta_i)_{min}))/2 \quad (4)$$

d_i = Displacement calculated according to earthquake loads on floor "i" of the building.
$(\Delta_i)_{max}$ = Maximum relative floor displacement on floor i of the building.

The relative floor displacement that causes the torsional irregularity below (Figure 4) is shown as shown in TBDY-2018.

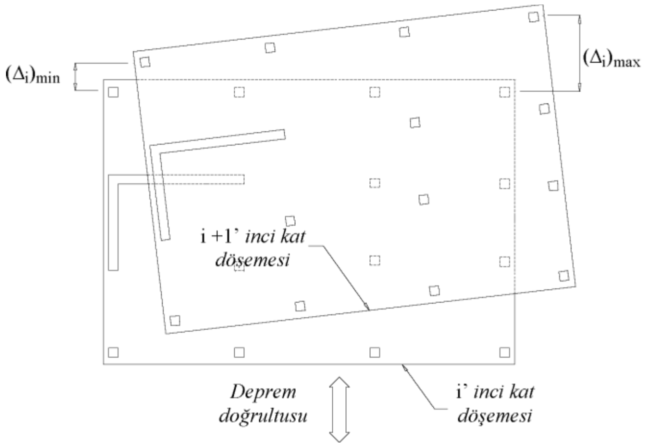

Figure 4. Relative floor displacement

If the torsional coefficient is greater than 1.2 on any floor as a result of the analysis, as stated in Article 4.7.4 of TBDY-2018, on condition that $1.2 < \eta_{bi} \leq 2.0$ is greater than 2.0, ±5% additional eccentricity applied on this floor will be magnified by multiplying with the coefficient D_i for both earthquake directions (eq. 5).

$$Di=(\frac{\eta bi}{1,2}) \quad (5)$$

In cases where the torsional coefficient exceeds the limit of 2.00 one of the dynamic analysis methods stated in the related regulation should be applied.

2.2. The Effect of Plan Geometry and Stiffness Distribution on Torsion

Ideally, the most suitable structures are the square type structures that are symmetrical in plan and cross-section. In such structures, the structure's centre of gravity and centre of stiffness is almost at the same place. However, this is often not possible due to architectural reasons. Torsional moment occurring in such structures with different geometries causes additional shear forces in the structures. In this regard, the stiffness distribution is more important than geometry. In cases where geometric figures cannot be avoided, stiffness distribution should be taken into account in order to prevent structure torsion. In addition, torsion can also be observed in structures that are symmetrical in terms of plan geometry and stiffness distribution, or where the centre of gravity and stiffness centre coincide. The reason for torsion here is that the stiffness of the elements in outer axles is relatively lower. The fact that the elevator shear walls are mostly planned in the core can be the best example of this.

The results of plan geometry and stiffness distribution can be listed as follows (Özmen 2001),

-In structures with irregularities in terms of stiffness distribution, torsional irregularity can be very high.

-Even in the most unfavorable structures in terms of torsion, η_{bi} the torsional irregularity coefficients remain below 2.00, which is the limit value for the equivalent seismic load application.

-The torsional irregularity can mostly be improved with the arrangements to be made on the weak axes of such structures in the carrier elements.

-The most effective method to improve torsional irregularities is to place shear walls on weak axes, albeit in limited numbers and sizes.

-Increasing the column or beam dimensions in weak axes is also beneficial decreasing torsional irregularity.

-Even in the structures with high torsional irregularities, no significant negativity is experienced in terms of sizing. It can be argued that amendments should be made in the measures for the foreseen torsional irregularities in the regulations.

-It can be said that stiffness distribution is a more important factor in terms of torsional irregularity than geometry.

3. ANALYSIS ON TORSIONAL IRREGULARITY FOR DIFFERENT SPECTRAL ACCELERATION COEFFICIENTS

3.1. Examined Structure Type

In order to interpret the torsional irregularity coefficients in the structures for different spectral acceleration coefficients, the structure was examined separately by selecting 3 different locations on Turkey Earthquake Hazard Maps Interactive Web Application (Table 2), on condition that geometric and stiffness values remain the same for the specific structure (Figure 5 and Figure 6). All analyses of the structure were made using the Etabs 18.1.1 program, and the information about the structure and the selected location are given in Table 1.

Table 1. Information about the structure

Information	Value
Total Structure Height	30m
Number of Floors	10
Building Importance Coefficient(I)	1
Behaviour Coefficient (R)	7
Overstrength Coefficient (D)	2.5
Local Floor Class	ZB
Column Size	50cm*50 cm
Beam Size	30cm*60 cm
Shear Wall Width	30 cm
Floor Thickness	20 cm
Coating Load	2 kN/m²
Live Load	2 kN/m²
Concrete Class	C30
Reinforcement Class	S420

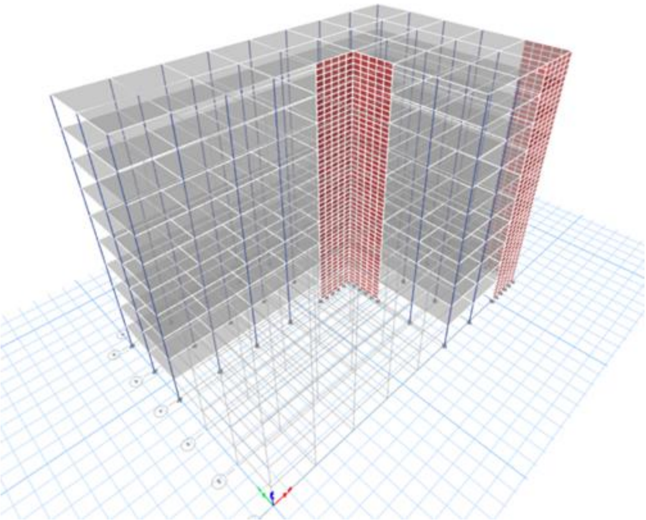

Figure 5. 3D view of the studied structure

Table 2. Location acceleration data

	Latitude	Longitude	S_S	S_1	S_{DS}	S_{D1}	PGA	PGV
Location-1	37.169372°	33.226919°	0.235	0.059	0.211	0.047	0.104	5.219
Location-2	37.269234°	29.615972°	0.894	0.218	0.805	0.174	0.386	20.442
Location-3	40.618555°	29.991237°	1.506	0.414	1.355	0.331	0.613	38.118

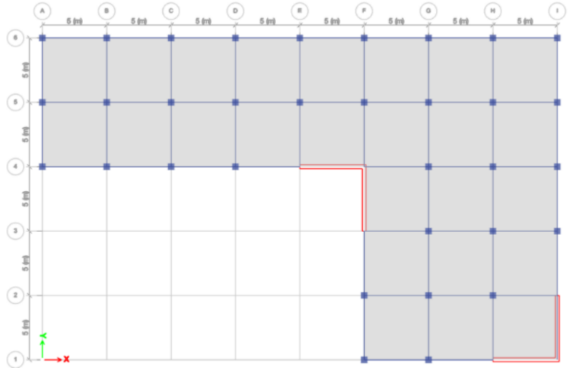

Figure 6. Plan of studied structure

3.2. Analysis Results of the Studied Structure

As a result of the analysis of the structure, the graphs of the torsional irregularity coefficient in figures 7 and 8 were obtained. As seen in related figures, torsional irregularities exist in both directions of the structures.

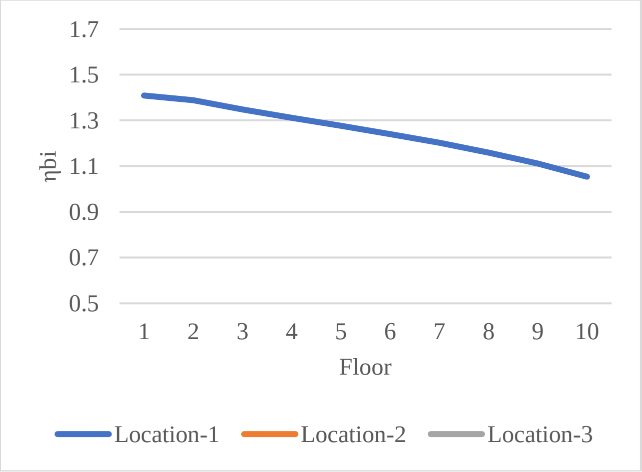

Figure 7. Comparison of torsional irregularity coefficient in X direction for different spectral acceleration coefficients

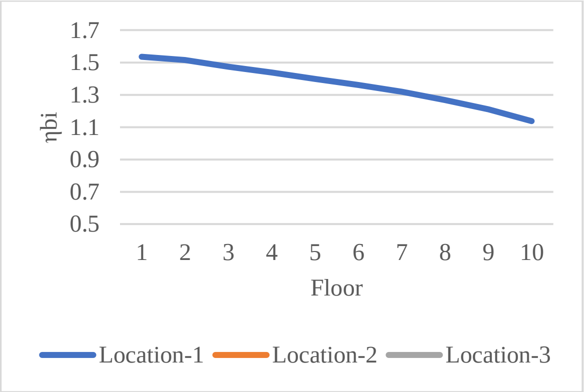

Figure 8. Comparison of torsional irregularity coefficient in Y direction for different spectral acceleration coefficients

3.3. Solution Proposal and Results for Torsional Irregularity in the Analysed Structure

In addition to the results of the analysed structure, in order to draw attention to the importance of the location of the shear wall elements, the structure was analysed again only by changing the location without changing the shear wall widths and number (Figure 9 and Figure 10), and the torsional irregularity coefficient was examined.

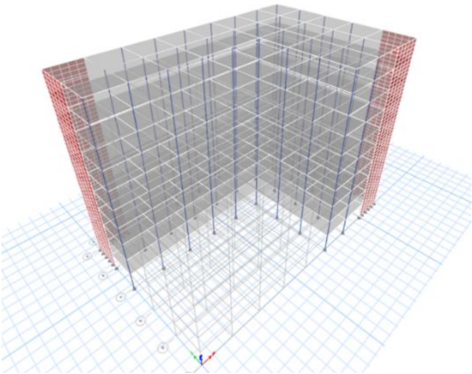

Figure 9. 3D View of the structure with stiffness adjustment

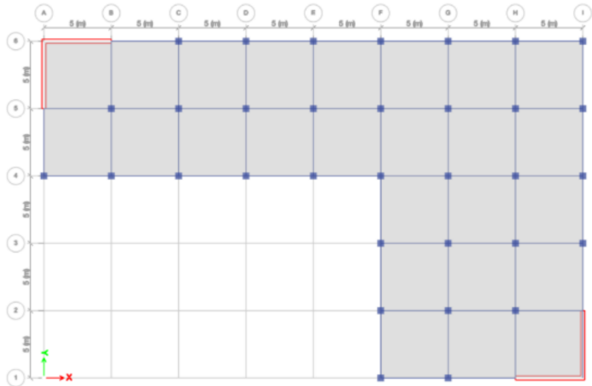

Figure 10. Plan of the structure with stiffness arrangement

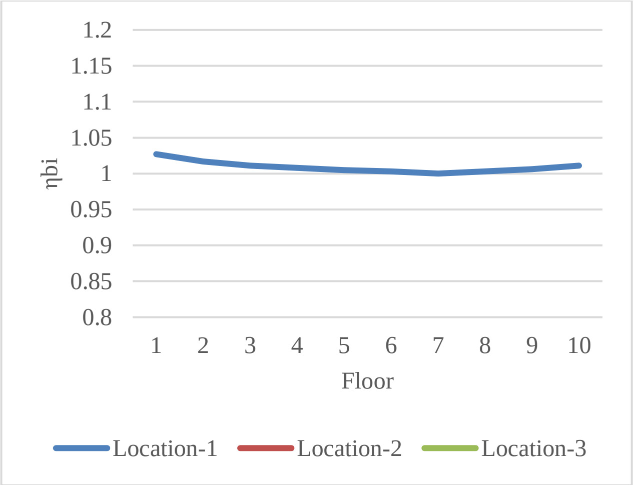

Figure 11. Comparison of torsional irregularity coefficient in X direction for different spectral acceleration coefficients of the adjusted structure

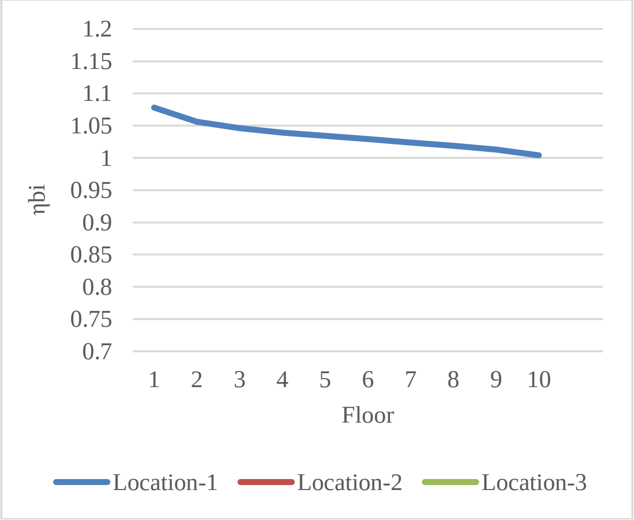

Figure 12. Comparison of torsional irregularity 4coefficient in Y direction for different spectral acceleration coefficients of the adjusted structure

4. RESULTS AND RECOMMENDATIONS

The most important result of the study is that the analysis of the same structure for different spectral acceleration coefficients, without changing the structure plan geometry and stiffness distribution, does not change the torsional irregularity coefficient.

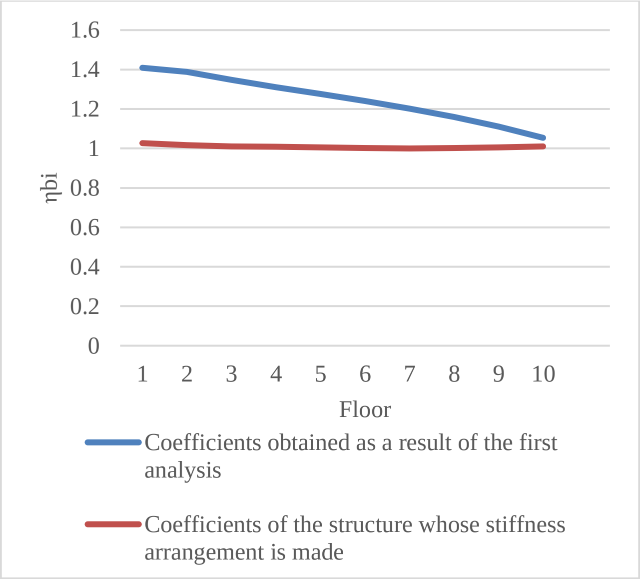

Figure 13. Comparison of torsion irregularity coefficients in the X Direction

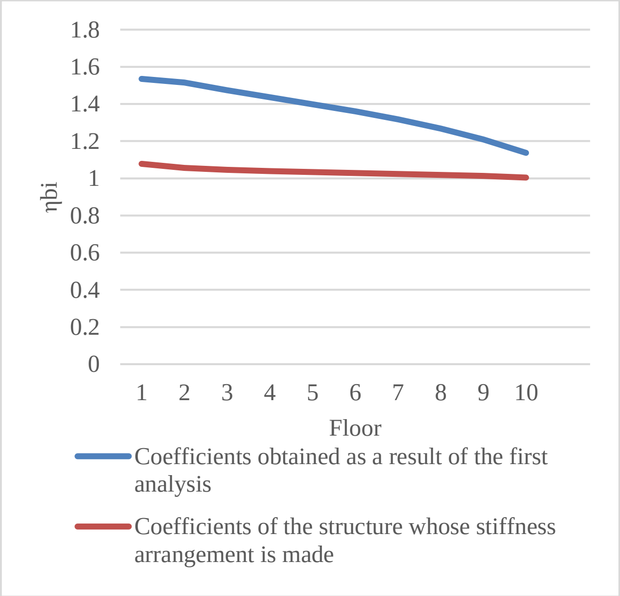

Figure 14. Comparison of torsion irregularity coefficients in the Y direction

Although different displacements and different torsional moments are obtained in the analysis results, the change in ground class and differentiation of static or dynamic loading states will not change the torsional irregularity coefficient. The torsional irregularity coefficient is ultimately a ratio, which is associated with the structure plan geometry and stiffness distribution (Yorulmaz 2018).

In Section 3.3, in order to draw attention to the position of the shear wall elements in terms of Civil Engineering discipline, it was seen that the torsional irregularity coefficient was reduced to reasonable levels by changing the positions only, without changing the number and size of the existing shear wall elements (Figure 13 and Figure 14).

When Figure 11 and Figure 12 are analyzed, the torsional irregularity coefficient of the structure, where the stiffness adjustment is made, is lower than 1.2, that's why lower stresses will occur in the elements and sections compared to other solutions.

Studies in the literature and the analyses done by us have once again shown that being able to model buildings in regular form is more important than the material and site environment in designing structures. Even though all the construction is done in accordance with the technique, placing the elements with insufficient and irregular stiffness in the unsuitable places will extremely force the structure at the time of the earthquake. It should not be forgotten that irregularities are extremely important for structure safety.

REFERENCES

Demir A & Dönmez D (2008). The factors affecting torsional irregularity in multi-storey structures. Celal Bayar University Journal of Science, 4(1), 31-36.

Demir A, Bağcı M & Demir D D (2011). Torsional behavior of an existing hospital building in different site classes. Celal Bayar University Journal of Science, 7(1), 17-27.

Doğan O & Er Ş B (2010). Live load distribution investigation of the impact on torsional irregularity. International Journal of Engineering Research and Development, 2(2), 57-60.

Döndüren M S, Karaduman A, Çöğürcü M T & Altın M (2007). Torsional irregularity in the structures. Journal of Selcuk-Technic, 6(1), 42-52.

Erdem H (2016). Effects of torsional irregularity on reinforced concrete behaviour. Çukurova University Journal of the Faculty of Engineering and Architecture, 31(1), 459-468.

Özmen G (2000). The effect of plan geometry on torsional irregularity. Turkey Engineering News, 410(6), 37-41.

Özmen G (2001). Effect of stiffness distribution on torsional irregularity. Turkey Engineering News, 411(1), 37-40.

Özmen G (2004). Excessive torsional irregularity in multi-story structures. Technical Journal, 15(1), 3131-3144.

Özmen G (2012). Torsional irregularity conditions in earthquake regulations. Turkey engineering news, 57 (2), 52-64.

Soyluk K & Yavuz İ Y (2009). Effect of Basement Retaining Walls to torsional irregularity in frame type. İmo technical journal, 20(97), 4654-4673.

Uçar T & Merter O (2009). Effect of configuration of shear walls at floor plan to earthquake behavior of shear wall-frame reinforced concrete buildings. Deu journal of Engineering Science, 11(2), 11-18.

Yorulmaz A M (2018). Investigation of A1 irregularity in reinforced concrete for different earthquake zone, MS Thesis, University of Kto Karatay, Konya, Turkey.

Yön B & Sayın E (2009). Investigation of effect of local site classes to columns behavior on structures with torsional irregularity. e-journal of New World Science Academy, 4(2), 126-135.

Turkish Journal of Engineering – 2021; 5(4); 183-192

Turkish Journal of Engineering

https://dergipark.org.tr/en/pub/tuje

e-ISSN 2587-1366

Optimal synthesis of function-generating slider-crank mechanism based on a closed-form solution using five design parameters

Hüseyin Mutlu*[1], **Ali Magdi Sayed Soliman**[1], **Gökhan Karapınarlı**[2]

[1]*Mersin University, Engineering Faculty, Mechanical Engineering Department, Mersin, Turkey*
[2]*Akyürek Makine Sanayi ve Tic. A.Ş, Mersin, Turkey*

Keywords
Kinematic Synthesis
Function Generation
Slider-Crank Mechanism
Closed-Form Solution

ABSTRACT

Kinematic dimensional synthesis is one of the essential steps during the process of design. It is classified into three tasks: function generation, path generation, and motion generation. In this paper, a design method is presented to solve the synthesis of the slider-crank mechanism for function generation based on a closed-form solution with five design parameters. The success criterion of a method used for function generation depends on the structural error function within an operational domain of the slider-crank mechanism. The structural error reduction is related to the number of design parameters utilized in mechanism synthesis, and the effective maximum number of design parameters for the slider-crank mechanism is five. In this study, the closed-form synthesis is found using three methods: precision point method, sub-domain method, and galerkin method. The system of equations is reduced to a twelfth-degree univariate polynomial equation, and thus all the available solutions are obtained. The effectiveness of this design method is tested with some examples of commonly used test functions, namely e^x, sin(x), tan(x) and ln(x), using a developed computer program. This design method gives lower structural error than traditional methods in kinematics literature.

1. INTRODUCTION

In kinematic synthesis, the shape and size of mechanical elements are determined to develop a flow of power through the system between the input and the output links, according to the desired performance (McCarthy and Joskowicz 2009; Söylemez 1985). The motion equation of the output link is to be a function of the input link's motion or a function of time, and it is formed from nonlinear algebraic and/or high order equations (Dhingra et al. 2000a; Wampler et al. 1990; Wampler et al. 1992; Almadi et al. 1996; Dhingra et al. 2001a; Dhingra et al. 2000b; Dhingra et al. 2001b; Akçalı 1984). These mathematical relationships between the input and output links are so complex; hence, graphical approaches are commonly utilized in solving such problems (Shigley 1961). However, graphical approaches are time-consuming and lack accuracy.

With the evolution of computers, many analytical methods have been developed, and they approximately express the desired function. Therefore, the structural error function which is the difference between the desired function and the function produced by a mechanism is taken into account and minimized using mathematical approaches depending on iteration such as the precision point method (Akçalı and Dittrich 1989), sub-domain method (Dhingra et al. 2000a), galerkin method (Hartenberg and Denavit 1964) and the least-squares method (Nolle 1997; Singh et al. 2005). Here, the most important factor in minimizing the structural error is the excess number of unknown parameters of a mechanism.

However, since the aforementioned methods are based on iteration, the excess number of unknown parameters causes great difficulties, and thus the solution may be impossible. For instance, in the solution of the precision point method of synthesis applied to nine positions in reference (Almadi et al. 1995), the Newton-Raphson technique was used in a solution strategy called 'Bootstrap.' And, due to the complexity of the equation,

---

* **Corresponding Author**

*(hmutlu@mersin.edu.tr) ORCID ID 0000 – 0002 – 4770 – 2873
(ali.magdi.sarhan@gmail.com) ORCID ID 0000 – 0003 – 1903 – 1141
(g.karapinarli@akyurekltd.com) ORCID ID 0000 – 0002 – 4641 – 8512

Cite this article

Mutlu H, Soliman A M S & Karapınarlı G (2021). Optimal synthesis of function-generating slider-crank mechanism based on a closed-form solution using five design parameters. Turkish Journal of Engineering, 5(4), 183-192

Research Article / DOI: XXXXXXXXXXXX

Received: 19/05/2020; Accepted: 16/07/2020

the drawing for each initial value does not exist. Even if a solution exists, different results are obtained from different initial values.

For kinematic synthesis problems, the precision point method and the least-squares method are extensively used to minimize the structural error (Singh et al. 2005; Tinubu and Gupta 1984). In this way, the structural error is zero at the given precision points while, at the mean values, it is small as possible. When the number of precision points increases, the structural error decreases at the mean values. The number of points that can be selected depends on the number of kinematic dimensions of the active mechanism in the design. However, when the number of parameters used in the design increases, it becomes difficult to obtain a closed-form solution. And if the number of unknown parameters exceeds five, the direct application of closed-form solutions to mechanism designs will probably lead to undesirable results (Akçalı 1984; Özkul and Mutlu 2018).

In this study, given five design parameters as a maximum, the design of the slider-crank mechanism for function generation with minimum error has been presented. The system of equations has been reduced to a twelfth-degree univariate polynomial equation, and in this way, all the possible solutions have been obtained. Because three methods (precision point method, sub-domain method, and galerkin method) are used in the solution, the designer has been provided with alternative solutions. Additionally, the effectiveness of the presented mathematical model is tested on some commonly used test functions by using a developed computer program. Accordingly, we found that our design method gives lower structural error than traditional methods in kinematics literature.

2. FUNCTION-GENERATING SLIDER-CRANK MECHANISM

For creating a required function using the sliding-crank mechanism, first, Fig. 1, which shows the mechanism's design parameters, is given. Here, x_1 is the crank length, x_2 is the connecting rod length, and x_3 is the vertical distance (AO_1).$\psi_0$is the angle when the crank starts rotating and s_n is the distance (AC), vertical on the AO_1 line, at the starting position when the angle ψ_0 occurs. While designing a function-generating slider-crank mechanism, two different functional relationships can be considered. The first functional relationship is between the crank rotation angle (ψ) and the linear horizontal displacement of the piston (s). The second functional relationship is between the crank rotation angle (ψ) and the angle of the connecting rod with the horizontal line (δ).

If the ψ-s functional relation is taken into consideration, the vector expression written from the closed-loop AO_1BC in Fig. 1 is squared and added side by side, and the angle of the connecting rod with the horizontal line (δ) is eliminated, the following motion equation, Eq. (1), is generated.

$$x_1^2 - 2sx_1\mathrm{Cos}\psi + 2x_1x_3\mathrm{Sin}\psi + x_3^2 + s^2 - x_2^2 = 0 \quad (1)$$

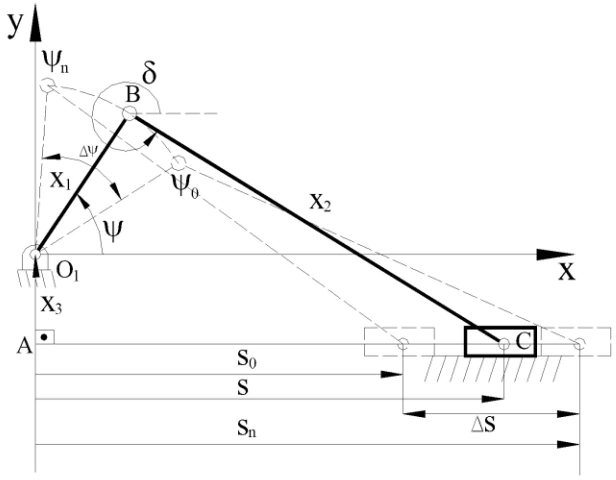

Figure 1. The design parameters of a function-generating slider-crank mechanism

Also, the following linear relations of the slider-crank mechanism, the angle (ψ) with the independent variable (x) of the desired function and the piston displacement (s) with the function's dependent variable (y), can be established as in expressions (2) and (3), respectively.

$$\psi = \psi_0 + \psi' \\ \psi' = R_x(x - x_0) \\ R_x = \frac{\Delta\psi}{\Delta x} \quad (2)$$

$$s = s_0 + s' \\ s' = R_y(y - y_0) \\ R_y = \frac{\Delta s}{\Delta y} \quad (3)$$

Here, the operational domains of the crank link and piston, determined by the designer, are($\Delta\psi = \psi_n - \psi_0$)and($\Delta s = s_n - s_0$), respectively. Also, the change amounts of the independent variable and dependent variable of the generated function are ($\Delta x = x_n - x_0$) and($\Delta y = y_n - y_0$), respectively. If Eq. (2) and Eq. (3) are written in Eq. (1), the motion equation can be obtained in the shape of $G(s_0, \psi_0, x_1, x_2, x_3, x, y) = 0$ as shown in Eq. (4).

$$\begin{aligned} 2s's_0 + s'^2 + Z_3(&sin\psi_0 cos\psi' + cos\psi_0 sin\psi') \\ &+ Z_1(-s_0 cos\psi_0 cos\psi' \\ &+ s_0 sin\psi_0 sin\psi' \\ &- s' cos\psi_0 \, cos\psi' \\ &+ s' sin\psi_0 sin\psi') + Z_2 = 0 \end{aligned} \quad (4)$$

where,

$$Z_1 = 2x_1 \\ Z_2 = {x_1}^2 + {x_3}^2 + {s_0}^2 - {x_2}^2 \\ Z_3 = 2x_1x_3$$

For solving the unknown parameters $(s_0, \psi_0, x_1, x_2, x_3)$ in Eq. (4), a nonlinear equation with five unknowns is obtained as shown in Eq. (5).

$$\begin{aligned}(a_i s_0 + g_i) + Z_3(c_i Sin\psi_0 + b_i Cos\psi_0)&\\ + Z_1(-c_i s_0 Cos\psi_0 + b_i s_0 Sin\psi_0&\\ - d_i Cos\psi_0 + e_i Sin\psi_0 + f_i Z_2&\\ = 0 \; i = 1,2,3,4,5&\end{aligned} \tag{5}$$

The coefficients (a_i, b_i, c_i, d_i, e_i, f_i, g_i) in Eq.(5) can be solved using the three methods: precision point method, sub-domain method, and galerkin method.

Precision Point Method:

$$\begin{gathered} a_i = 2s'_i \\ b_i = Sin\psi'_i \\ c_i = Cos\psi'_i \\ d_i = s' Cos\psi'_i \\ e_i = s'_i Sin\psi'_0 \\ f_i = 1 \\ g_i = s'^2_i \\ i = 1,2,3,4,5 \end{gathered} \tag{6}$$

Sub-domain Method:

$$\left.\begin{aligned} a_i &= 2\int_{x_{i-1}}^{x_i} s' dx \\ b_i &= \int_{x_{i-1}}^{x_i} Sin\psi' dx \\ c_i &= \int_{x_{i-1}}^{x_i} Cos\psi' dx \\ d_i &= \int_{x_{i-1}}^{x_i} s' Cos\psi' dx \\ e_i &= \int_{x_{i-1}}^{x_i} s' Sin\psi' dx \\ f_i &= \int_{x_{i-1}}^{x_i} dx \\ g_i &= \int_{x_{i-1}}^{x_i} s'^2 dx \end{aligned}\right\} i = 1,2,3,4,5 \tag{7}$$

Galerkin Method:

$$\left.\begin{aligned} a_i &= 2\int_{x_0}^{x_n} s' w_i(x) dx \\ b_i &= \int_{x_0}^{x_n} Sin\psi' w_i(x) dx \\ c_i &= \int_{x_0}^{x_n} Cos\psi' w_i(x) dx \\ d_i &= \int_{x_0}^{x_n} s' Cos\psi' w_i(x) dx \\ e_i &= \int_{x_0}^{x_n} s' Sin\psi' w_i(x) dx \\ f_i &= \int_{x_0}^{x_n} w_i(x) dx \\ g_i &= \int_{x_0}^{x_n} s'^2 w_i(x) dx \end{aligned}\right\} i = 1,2,3,4,5 \tag{8}$$

To achieve the closed-form solution, if Z_2, Z_3 and $Z_1$are eliminated from Eq. (5) and the equation is rearranged, two nonlinear equations depending on the unknown parameters tan(ψ$_0$) and $s_0$are obtained, as in Eq. (9).

$$\begin{aligned} a_{pk} s_0^2 + (b_{pk} + c_{pk} \cos 2\psi_0 + d_{pk} \sin 2\psi_0) s_0&\\ + e_{pk} + f_{pk} \cos 2\psi_0&\\ + g_{pk} \sin 2\psi_0) = 0&\\ k = 1,2&\end{aligned} \tag{9}$$

The computable coefficients in Eq. (9) are given below in Appendix A in Eqs. (10-16). If the term (s_0) is removed using the intersection function mentioned in (Akçalı et al. 2006), the 12th-degree univariate polynomial equation dependent on t can be obtained as in Eq. (17).

$$\begin{aligned} w_0 + w_1 t + w_2 t^2 + w_3 t^3 + w_4 t^4 + w_5 t^5&\\ + w_6 t^6 - w_5 t^7 + w_4 t^8 - w_3 t^9&\\ + w_2 t^{10} - w_1 t^{11} + w_0 t^{12} = 0&\end{aligned} \tag{17}$$

$$\text{where, } t = \tan \frac{\psi_0}{2} \tag{18}$$

The coefficients of Eq. (17) are given also in Appendix A in Eqs. (19-25). As a result of finding all the roots of Eq. (17), a set of 12 solutions (real or complex) for the ψ_0 angle is found as given in Eq. (26).

$$\psi_{oi} = 2 \;\; arctan \;\; t_i; \;\; i = 1,2.\ldots,12 \tag{26}$$

For calculating the other kinematic quantities (s_0, x_1, x_2, x_3) of the function-generating slider-crank mechanism, firstly, if the term s_0^2 is removed from Eq. (9), s_0 will be found as in Eq. (27).

$$s_{oi} = -\frac{\begin{gathered} a_{p1}e_{p2} - a_{p2}e_{p1} + \\ (a_{p1}f_{p2} - a_{p2}f_{p1}) \cos 2\psi_{0i} + \\ (a_{p1}g_{p2} - a_{p2}g_{p1}) \sin 2\psi_{0i} \end{gathered}}{\begin{gathered} a_{p1}b_{p2} - a_{p2}b_{p1} + \\ (a_{p1}c_{p2} - a_{p2}c_{p1}) \cos 2\psi_{0i} + \\ (a_{p1}d_{p2} - a_{p2}d_{p1}) \sin 2\psi_{0i} \end{gathered}}$$

$$i = 1,\ldots.,12 \tag{27}$$

And, for calculating the other three dimensional parameters (x_1, x_2 and x_3), the following path in Eqs. (28-33) is followed.

$$Z_{3i} = -\frac{\begin{Bmatrix} 2\cos\psi_{0i}\,(-d_k f_2 g_1 + d_2 f_k g_1 + d_k f_1 g_2 - \\ d_1 f_k g_2 - d_2 f_1 g_k + d_1 f_2 g_k) + \\ 2\sin\psi_{0i}\,(e_k f_2 g_1 - e_2 f_k g_1 - e_k f_1 g_2 + \\ e_1 f_k g_2 + e_2 f_1 g_k - e_1 f_2 g_k) + \\ s_0(2\sin\psi_{0i}\,(a_k e_2 f_1 - a_2 e_k f_1 - a_k e_1 f_2 + \\ a_1 e_k f_2 + a_2 e_1 f_k - a_1 e_2 f_k + \\ b_k f_2 g_1 - b_2 f_k g_1 - b_k f_1 g_2 + b_1 f_k g_2 + \\ b_2 f_1 g_k - b_1 f_2 g_k) + \\ 2\cos\psi_{0i}\,(-a_k d_2 f_1 + a_2 d_k f_1 + a_k d_1 f_2 - \\ a_1 d_k f_2 - a_2 d_1 f_k + a_1 d_2 f_k - \\ c_k f_2 g_1 + c_2 f_k g_1 + c_k f_1 g_2 - c_1 f_k g_2 - \\ c_2 f_1 g_k + c_1 f_2 g_k)) + \\ s_0^2(2\sin\psi_{0i}\,(a_k b_2 f_1 - a_2 b_k f_1 - a_k b_1 f_2 + \\ a_1 b_k f_2 + a_2 b_1 f_k - a_1 b_2 f_k) + \\ 2\cos\psi_{0i}\,(-a_k c_2 f_1 + a_2 c_k f_1 + a_k c_1 f_2 - \\ a_1 c_k f_2 - a_2 c_1 f_k + a_1 c_2 f_k)) + \end{Bmatrix}}{\begin{Bmatrix} -b_k d_2 f_1 + b_2 d_k f_1 + c_k e_2 f_1 - c_2 e_k f_1 + \\ b_k d_1 f_2 - b_1 d_k f_2 - c_k e_1 f_2 + \\ c_1 e_k f_2 - b_2 d_1 f_k + b_1 d_2 f_k + c_2 e_1 f_k - c_1 e_2 f_k + \\ \sin 2\psi_{0i}(-c_k d_2 f_1 + c_2 d_k f_1 + b_k e_2 f_1 - \\ b_2 e_k f_1 + c_k d_1 f_2 - c_1 d_k f_2 - b_k e_1 f_2 + \\ b_1 e_k f_2 - c_2 d_1 f_k + c_1 \mathrm{d}_2 f_k + b_2 e_1 f_k - b_1 e_2 f_k) + \\ \cos 2\psi_{0i}(-b_k d_2 f_1 + b_2 d_k f_1 - c_k e_2 f_1 + \\ c_2 e_k f_1 + b_k d_1 f_2 - b_1 d_k f_2 + c_k e_1 f_2 - \\ c_1 e_k f_2 - b_2 d_1 f_k + b_1 d_2 f_k - c_2 e_1 f_k + c_1 e_2 f_k) + \\ 2s_{0i}(-b_k c_2 f_1 + b_2 c_k f_1 + b_k c_1 \mathrm{f}_2 - \\ b_1 c_k f_2 - b_2 c_1 f_k + b_1 c_2 f_k) \end{Bmatrix}}$$

$$\begin{gathered} i = 1,..,12 \\ k = 3,4,5 \end{gathered} \tag{28}$$

$$Z_{1i} = -\frac{\left\{\begin{matrix} f_1 g_k - f_k g_1 + s_{0i}(a_k f_1 - a_1 f_k) + \\ Z_{3i} \cos\psi_{0i}(b_k f_1 - b_1 f_k) + \\ Z_{3i} \sin\psi_{0i}(c_k f_1 - c_1 f_k) \end{matrix}\right\}}{\left\{\begin{matrix} \cos\psi_{0i}(s_{0i}(c_1 f_k - c_k f_1) + \\ d_1 f_k - d_k f_1) + \\ \sin\psi_{0i}(s_{0i}(b_k f_1 - b_1 f_k) + \\ e_k f_1 - e_1 f_k) \end{matrix}\right\}} \qquad (29)$$

$$i = 1,..,12$$
$$k = 1,2,3,4,5 \qquad (30)$$

$$x_{1i} = \frac{Z_{1i}}{2} \quad i = 1,2,....,12 \qquad (31)$$

$$x_{3i} = \frac{Z_{3i}}{2x_{1i}} \quad i = 1,2,...,12 \qquad (32)$$

$$x_{2i} = \sqrt{x_{1i}^2 + x_{3i}^2 + s_{0i}^2 - Z_{2i}} \quad i = 1,2,..,12 \qquad (33)$$

The structural error (e) is given in Eq. (34) to determine the accuracy of the actual solutions (x_{1j}, x_{2j}, x_{3j}, s_{0j}, ψ_{0j}), j=1, 2, ..., 12, in the solution set.

$$e = s_{th} - s_{ac} \qquad (34)$$

where s_{th} is the theoretical piston displacement calculated in Eq. (3), and s_{ac} represents the actual piston displacement calculated from Eq. (35) below. Finally only one solution from Eq. (35) will correspond to the desired function.

$$s_{ac\pm} = \frac{2x_1 \cos(\psi_0 + \psi') \pm \sqrt{\begin{matrix}(2x_1 \cos(\psi_0 + \psi'))^2 - \\ 4\begin{pmatrix} x_1^2 + x_3^2 - x_2^2 + \\ 2x_1 x_3 \sin(\psi_0 + \psi') \end{pmatrix}\end{matrix}}}{2} \qquad (35)$$

The compatibility of the designed slider-crank mechanism to the desired function is determined by the distribution of the structural error function in Eq. (34).

3. NUMERICAL EXAMPLES

The above-mentioned design approaches were employed using a developed computer program for generating commonly used functions such as e^x, sin(x), tan(x), and ln(x) by the slider-crank mechanism. Taking into consideration the structural error values of the real solutions from among the various solutions obtained as well as the compatibility of the aspect ratios with manufacturing, the structural error functions of the three approaches are presented. Here, four examples of test functions generated by the slider-crank mechanism are given.

3.1. Example A

In this example, the desired function is $y=e^x$ over $0 \leq x \leq 1$. The design results of the slider-crank mechanism that produces this function while the input link rotates $\Delta\psi = 90^0$ and the output link moves $\Delta s = -1.0$ (dimensionless, as a scale) have been obtained according to the three different methods as shown in Table 1.

Table 1. The design results for $y=e^x$ over $0 \leq x \leq 1$ using three methods

Precision Point Method	
Precision points	x_{pi}, (i=1, ..., 5) = 0.0, 0.2, 0.5, 0.8, 1.0
Mechanism dimensions	x_1= -1.241043 x_2= 2.123150 x_3= -0.814295 ψ_0= 150.324° s_0= -0.492244
Maximum absolute error	0.00027071
Sub-domain Method	
Sub-domains	x_{si}, (i=1, ..., 6) = 0.0, 0.2, 0.4, 0.6, 0.8, 1.0
Mechanism dimensions	x_1= -1.223522 x_2= 2.119717 x_3= -0.820609 ψ_0= 150.6590° s_0= -0.506569
Maximum absolute error	-0.00069492
Galerkin Method	
Weighting functions	w_i, (i=1, ..., 5)= 1, x, x^2, x^3, x^4
Mechanism dimensions	x_1= -1.240452 x_2= 2.137685 x_3= -0.824552 ψ_0= 149.7941° s_0= -0.499602
Maximum absolute error	-0.00037269

The structural error distribution for this example is shown in Fig. (2).

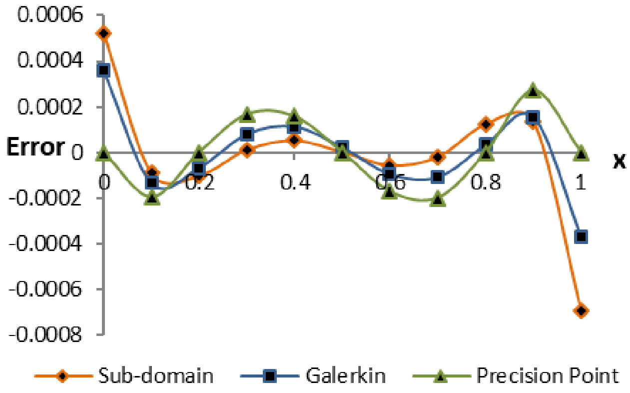

Figure 2. Structural error curve for e^x

3.2. Example B

The desired function of this example is y=sin(x) over $0° \leq x \leq 90°$.The design results of the slider-crank mechanism that produces this function while the input link rotates$\Delta\psi = 80^{\circ}$ and the output link moves $\Delta s = -1.0$ have been obtained according to the three different methods as shown in Table 2.

The structural error distribution for this example is as shown in Fig. (3).

Table 2. The design results for y=sin(x) over 0° ≤ x ≤ 90° using three methods

Precision Point Method	
Precision points	x_{pi}, (i=1, ..., 5) = 0.000, 0.436, 0.873, 1.309, 1.571
Mechanism dimensions	x_1= -1.086305 x_2= 7.310604 x_3= 0.917419 ψ_0= -73.7607° s_0= -7.346641
Maximum absolute error	-0.00014533
Sub-domain Method	
Sub-domains	x_{si}, (i=1, ..., 6) = 0.000, 0.349, 0.698, 1.047, 1.396, 1.571
Mechanism dimensions	x_1= -1.088700 x_2= 7.504273 x_3= 0.941629 ψ_0= -73.7607° s_0= -7.541173
Maximum absolute error	0.00025793
Galerkin Method	
Weighting functions	w_i, (i=1, ..., 5) =1, x, x^2, x^3, x^4
Mechanism dimensions	x_1= -1.077320 x_2= 7.185135 x_3= 1.089057 ψ_0= -72.5057° s_0= -7.190281
Maximum absolute error	-0.00010383

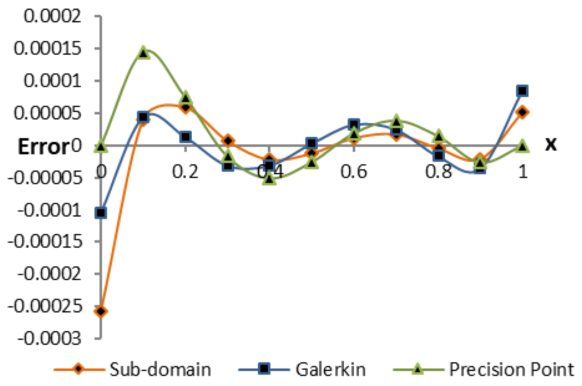

Figure 3. Structural error curve for sin(x)

3.3. Example C

In this example, the desired function is y=tan(x) over 0° ≤ x ≤ 45°.The design results of the slider-crank mechanism that produces this function while the input link rotates $\Delta\psi = 80^{\circ}$ and the output link moves $\Delta s = -0.5$ have been obtained according to the three different methods as shown below in Table 3.

The structural error distribution for this example is as shown in Fig. (4).

Table 3. The design results for y = tan(x) over 0° ≤ x ≤ 45° using three methods

Precision Point Method	
Precision points	x_{pi}, (i=1, ..., 5) = 0.000, 0.175, 0.349, 0.524, 0.785
Mechanism dimensions	x_1= 3.002218 x_2= 2.470431 x_3= -0.531810 ψ_0= 92.8363° s_0= -0.013371
Maximum absolute error	-0.00011431
Sub-domain Method	
Sub-domains	x_{si}, (i=1, ..., 6) = 0.000, 0.175, 0.349, 0.524, 0.698, 0.785
Mechanism dimensions	x_1= 3.458880 x_2= 2.928213 x_3= -0.530865 ψ_0= 94.2682° s_0= -0.019198
Maximum absolute error	-0.00102642
Galerkin Method	
Weighting functions	w_i, (i=1, ..., 5) =1, x, x^2, x^3, x^4
Mechanism dimensions	x_1= 3.278928 x_2= 2.747495 x_3= -0.531536 ψ_0= 93.7131° s_0= -0.017070
Maximum absolute error	-0.00053734

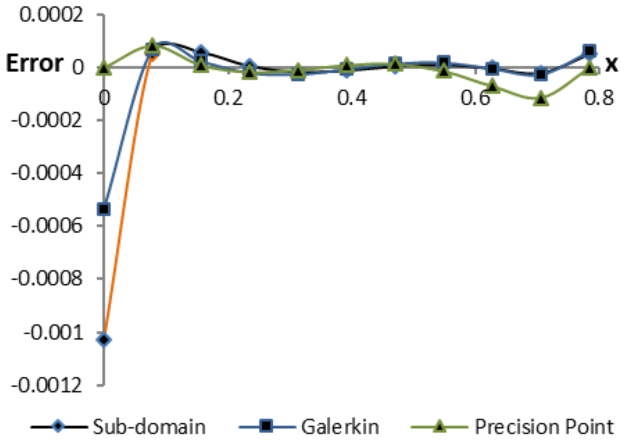

Figure 4. Structural error curve for tan(x)

3.4. Example D

Finally, in this example, the desired function is y=ln(x) over 1≤x≤2. The design results of the slider-crank mechanism that produces this function while the input link rotates $\Delta\psi = 90^{\circ}$ and the output link moves $\Delta s = -0.1$ have been obtained according to the following three different methods shown in Table 4.

The structural error distribution for this example is as shown in Fig. (5).

Table 4. The design results for y=ln(x) over 1≤ x ≤2 using three methods

Precision Point Method	
Precision points	x_{pi}, (i=1, ..., 5) = 1.00, 1.20, 1.50, 1.80, 2.00
Mechanism dimensions	x_1= 1.505762 x_2= 2.608397 x_3= -1.094561 ψ_0= 151.2138° s_0= 1.262414
Maximum absolute error	0.00025632
Sub-domain Method	
Sub-domains	x_{si}, (i=1, ..., 6) = 1.00, 1.200, 1.40, 1.60, 1.80, 2.00
Mechanism dimensions	x_1= 1.475092 x_2=2.590246 x_3= -1.105152 ψ_0=151.1454° s_0= 1.268790
Maximum absolute error	-0.00080016
Galerkin Method	
Weighting functions	w_i, (i=1, ..., 5) =1, x, x^2, x^3, x^4
Mechanism dimensions	x_1= 1.507783 x_2=2.620459 x_3= -1.103462 ψ_0=151.8690° s_0=1.261505
Maximum absolute error	-0.00055926

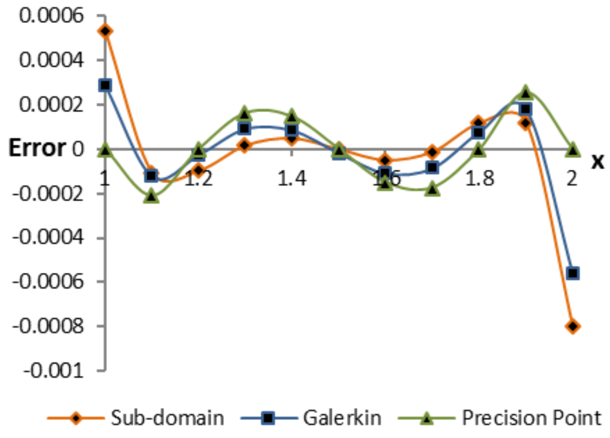

Figure 5. Structural error curve for ln(x)

4. DISCUSSION AND CONCLUSION

During the examination of the abovementioned examples, the achieved maximum values in the structural error distributions of the three methods (precision point method, sub-domain method, and galerkin method) are compared with the results discussed in kinematics literature as given in Appendix B. Accordingly, our results demonstrated in this paper were found to be much better.

The structural error distributions of the three methods are given as shown in Figs. (2-5) and, accordingly, it can be said that there is no clear superiority of one method over the others. However, in the sub-domain and the precision point methods, the structural error distribution is greatly influenced by the arbitrarily selected sub-domains and precision points, whereas in the galerkin method, the error distribution is not affected by the weighting functions selected arbitrarily. In this case, the galerkin method has superiority over the other two methods. Finally, the design algorithm discussed in this study can be applied to different types of mechanisms and also for path and motion synthesis, as well.

FUNDING: This research received no financial support for the research, authorship, and/or publication of this article.

CONFLICTS OF INTEREST: The authors declare that they have no conflict of interest.

REFERENCES

Akçalı I D (1984). Mekanizma tekniğinde yörünge ve fonksiyon sentezine çeşitli yaklaşımların gözden geçirilmesi. Doğa, 8(1), 1-12.

Akçalı I D & Dittrich G (1989). Function generation by Galerkin's method. Mechanism and Machine Theory, 24(1), 39-43. https://doi.org/10.1016/0094-114X(89)90081-5

Akçalı I D & Mutlu H (2006). A novel approach in the direct kinematics of Stewart platform mechanisms with planar platforms. Journal of Mechanical Design, 128(1), 252-263. https://doi.org/10.1115/1.1864114

Almadi A N, Dhingra A K & Kohli D (1996). Closed-form displacement analysis of SDOF 8-link mechanisms. Proceedings of ASME Design Engineering Technology Conference, Irvine, California.

Almadi A N, Dhingra A K & Kohli D (1995). Displacement analysis of ten-link kinematic chains using homotopy. Proceedings of 9th World Congress on the Theory of Machines and Mechanisms, Milan, Italy, 90-94.

Dhingra A K, Almadi A N & Kohli D (2000a). Closed-form approach to coupler-curves of multi-loop mechanisms. ASME Journal of Mechanical Design, 122(4), 464-471. https://doi.org/10.1115/1.1290394

Dhingra A K, Almadi A N & Kohli D (2000b). Closed-form displacement analysis of 8, 9 and 10-link mechanisms: Part-II: 9-link 2-DOF and 10-link 3-DOF mechanisms. Mechanisms and Machine Theory, 35(6), 851-869. https://doi.org/10.1016/S0094-114X(99)00033-6

Dhingra A K, Almadi A N & Kohli D (2001a). Closed-form displacement analysis of 10-link mechanisms: Part-I. Mechanisms and Machine Theory, 36(1), 29-56. https://doi.org/10.1016/S0094-114X(00)00040-9

Dhingra A K, Almadi A N and Kohli D (2001b). Closed-form displacement analysis of 10-link mechanisms: Part-II: polynomial solutions. Mechanisms and Machine Theory, 36(1), 57-75. https://doi.org/10.1016/S0094-114X(00)00039-2

Hartenberg R S & Denavit J (1964). Kinematics synthesis of linkages, McGraw-Hill, New York, USA.

Jaiswal A & Jawale H P (2018). Synthesis and optimization of four bar mechanism with six design parameters. AIP Conference Proceedings, 1943(1). https://doi.org/10.1063/1.5029590

McCarthy J M & Joskowicz L (2009). Kinematic synthesis, Cambridge University Press.

Mehar K, Singh S & Mehar R (2015). Optimal synthesis of four-bar mechanism for function generation with five accuracy points. Inverse Problems in Science and Engineering, 23(7), 1222-1236. https://doi.org/10.1080/17415977.2014.993982

Nolle H (1997). Linkage coupler curve synthesis: a historical review-III spatial synthesis and optimization. Mechanism and Machine Theory, 10(1), 41-55.

Özkul İ & Mutlu H (2018). Modular approach to the design of path generating planar mechanisms. Turkish Journal of Engineering, 2(2), 60-72. DOI: 10.31127/tuje.345153

Shigley J E (1961). Theory of Machines, McGraw-Hill, New York, USA.

Singh V P, Sharma S & Thakur B S (2005). Kinematic synthesis and optimization of four-bar linkage. Journal of the Institution of Engineers (India), Part MC, Mechanical Engineering Division, 85, 199-205.

Söylemez E (1985). Mechanisms. Ankara Üniversitesi Basım evi, Ankara, Turkey (in Turkish).

Tinubu S O & Gupta K C (1984). Optimal synthesis of function generators without the branch defect. ASME, 106(3), 348-354. https://doi.org/10.1115/1.3267418

Wampler C W, Morgan A P & Sommese A J (1990). Numerical continuation methods for solving polynomial systems arising in kinematics. ASME Journal of Mechanical Design, 112(1), 59-68. https://doi.org/10.1115/1.2912579

Wampler C W, Morgan A P & Sommese A J (1992). Complete solutions of the nine-point path synthesis problem for four-bar linkages. ASME Journal of Mechanical Design, 114(1), 153-159. https://doi.org/10.1115/1.2916909

APPENDIX A. Computed coefficients of the abovementioned equations

$$a_{pi}= 2a_kb_3c_2f_1- 2a_3b_kc_2f_1- 2a_kb_2c_3f_1+ 2a_2b_kc_3f_1+ 2a_3b_2c_kf_1- 2a_2b_3c_kf_1- 2a_kb_3c_1f_2+ 2a_3b_kc_1f_2+ 2a_kb_1c_3f_2- 2a_1b_kc_3f_2- 2a_3b_1c_kf_2+ 2a_1b_3c_kf_2+ 2a_kb_2c_1f_3- 2a_2b_kc_1f_3- 2a_kb_1c_2f_3+ 2a_1b_kc_2f_3+ 2a_2b_1c_kf_3- 2a_1b_2c_kf_3- 2a_3b_2c_1f_k+ 2a_2b_3c_1f_k+ 2a_3b_1c_2f_k- 2a_1b_3c_2f_k- 2a_2b_1c_3f_k+ 2a_1b_2c_3f_k$$

$$i=1, 2 \quad k=i+1 \tag{10}$$

$$b_{pi} =a_kb_3d_2f_1- a_3b_kd_2f_1- a_kb_2d_3f_1+ a_2b_kd_3f_1+ a_3b_2d_kf_1- a_2b_3d_kf_1- a_kc_3e_2f_1+ a_3c_ke_2f_1+ a_kc_2e_3f_1- a_2c_ke_3f_1- a_3c_2e_kf_1+ a_2c_3e_kf_1- a_kb_3d_1f_2+ a_3b_kd_1f_2+ a_kb_1d_3f_2- a_1b_kd_3f_2- a_3b_1d_kf_2+ a_1b_3d_kf_2+ a_kc_3e_1f_2- a_3c_ke_1f_2- a_kc_1e_3f_2+ a_1c_ke_3f_2+ a_3c_1e_kf_2- a_1c_3e_kf_2+ a_kb_2d_1f_3- a_2b_kd_1f_3- a_kb_1d_2f_3+ a_1b_kd_2f_3+ a_2b_1d_kf_3- a_1b_2d_kf_3- a_kc_2e_1f_3+ a_2c_ke_1f_3+ a_kc_1e_2f_3- a_1c_ke_2f_3- a_2c_1e_kf_3+ a_1c_2e_kf_3- a_3b_2d_1f_k+ a_2b_3d_1f_k+ a_3b_1d_2f_k- a_1b_3d_2f_k- a_2b_1d_3f_k+ a_1b_2d_3f_k+ a_3c_2e_1f_k- a_2c_3e_1f_k- a_3c_1e_2f_k+ a_1c_3e_2f_k+ a_2c_1e_3f_k- a_1c_2e_3f_k- 2b_kc_3f_2g_1+ 2b_3c_kf_2g_1+ 2b_kc_2f_3g_1- 2b_2c_kf_3g_1- 2b_3c_2f_kg_1+ 2b_2c_3f_kg_1+ 2b_kc_3f_1g_2- 2b_3c_kf_1g_2- 2b_kc_1f_3g_2+ 2b_1c_kf_3g_2+ 2b_3c_1f_kg_2- 2b_1c_3f_kg_2- 2b_kc_2f_1g_3+ 2b_2c_kf_1g_3+ 2b_kc_1f_2g_3- 2b_1c_kf_2g_3- 2b_2c_1f_kg_3+ 2b_1c_2f_kg_3+ 2b_3c_2f_1g_k- 2b_2c_3f_1g_k- 2b_3c_1f_2g_k+ 2b_1c_3f_2g_k+ 2b_2c_1f_3g_k- 2b_1c_2f_3g_k$$

$$i=1, 2 \quad k=i+1 \tag{11}$$

$$c_{pi}=a_kb_3d_2f_1- a_3b_kd_2f_1- a_kb_2d_3f_1+ a_2b_kd_3f_1+ a_3b_2d_kf_1- a_2b_3d_kf_1+ a_kc_3e_2f_1- a_3c_ke_2f_1- a_kc_2e_3f_1+ a_2c_ke_3f_1+ a_3c_2e_kf_1- a_2c_3e_kf_1- a_kb_3d_1f_2+ a_3b_kd_1f_2+ a_kb_1d_3f_2- a_1b_kd_3f_2- a_3b_1d_kf_2+ a_1b_3d_kf_2- a_kc_3e_1f_2+ a_3c_ke_1f_2+ a_kc_1e_3f_2- a_1c_ke_3f_2- a_3c_1e_kf_2+ a_1c_3e_kf_2+ a_kb_2d_1f_3- a_2b_kd_1f_3- a_kb_1d_2f_3+ a_1b_kd_2f_3+ a_2b_1d_kf_3- a_1b_2d_kf_3+ a_kc_2e_1f_3- a_2c_ke_1f_3- a_kc_1e_2f_3+ a_1c_ke_2f_3+ a_2c_1e_kf_3- a_1c_2e_kf_3- a_3b_2d_1f_k+ a_2b_3d_1f_k+ a_3b_1d_2f_k- a_1b_3d_2f_k- a_2b_1d_3f_k+ a_1b_2d_3f_k- a_3c_2e_1f_k+ a_2c_3e_1f_k+ a_3c_1e_2f_k- a_1c_3e_2f_k- a_2c_1e_3f_k+ a_1c_2e_3f_k$$

$$i=1, 2 \quad k=i+1 \tag{12}$$

$$d_{pi} =a_kc_3d_2f_1- a_3c_kd_2f_1- a_kc_2d_3f_1+ a_2c_kd_3f_1+ a_3c_2dkf_1- a_2c_3d_kf_1- a_kb_3e_2f_1+ a_3b_ke_2f_1+ a_kb_2e_3f_1- a_2b_ke_3f_1- a_3b_2e_kf_1+ a_2b_3e_kf_1- a_kc_3d_1f_2+ a_3c_kd_1f_2+ a_kc_1d_3f_2- a_1c_kd_3f_2- a_3c_1d_kf_2+ a_1c_3d_kf_2+ a_kb_3e_1f_2- a_3b_ke_1f_2- a_kb_1e_3f_2+ a_1b_ke_3f_2+ a_3b_1e_kf_2- a_1b_3e_kf_2+ a_kc_2d_1f_3- a_2c_kd_1f_3- a_kc_1d_2f_3+ a_1c_kd_2f_3+ a_2c_1d_kf_3- a_1c_2d_kf_3- a_kb_2e_1f_3+ a_2b_ke_1f_3+ a_kb_1e_2f_3- a_1b_ke_2f_3- a_2b_1e_kf_3+ a_1b_2e_kf_3- a_3c_2d_1f_k+ a_2c_3d_1f_k+ a_3c_1d_2f_k- a_1c_3d_2f_k- a_2c_1d_3f_k+ a_1c_2d_3f_k+ a_3b_2e_1f_k- a_2b_3e_1f_k- a_3b_1e_2f_k+ a_1b_3e_2f_k+ a_2b_1e_3f_k- a_1b_2e_3f_k$$

$$i=1, 2 \quad k=i+1 \tag{13}$$

$$e_{pi} =-b_kd_3f_2g_1+ b_3d_kf_2g_1+ c_ke_3f_2g_1- c_3e_kf_2g_1+ b_kd_2f_3g_1- b_2d_kf_3g_1- c_ke_2f_3g_1+ c_2e_kf_3g_1- b_3d_2f_kg_1+ b_2d_3f_kg_1+ c_3e_2f_kg_1- c_2e_3f_kg_1+ b_kd_3f_1g_2- b_3d_kf_1g_2- c_ke_3f_1g_2+ c_3e_kf_1g_2- b_kd_1f_3g_2+ b_1d_kf_3g_2+ c_ke_1f_3g_2- c_1e_kf_3g_2+ b_3d_1f_kg_2- b_1d_3f_kg_2- c_3e_1f_kg_2+ c_1e_3f_kg_2- b_kd_2f_1g_3+ b_2d_kf_1g_3+ c_ke_2f_1g_3- c_2e_kf_1g_3+ b_kd_1f_2g_3- b_1d_kf_2g_3- c_ke_1f_2g_3+ c_1e_kf_2g_3- b_2d_1f_kg_3+ b_1d_2f_kg_3+ c_2e_1f_kg_3- c_1e_2f_kg_3+ b_3d_2f_1g_k- b_2d_3f_1g_k- c_3e_2f_1g_k+ c_2e_3f_1g_k- b_3d_1f_2g_k+ b_1d_3f_2g_k+ c_3e_1f_2g_k- c_1e_3f_2g_k+ b_2d_1f_3g_k- b_1d_2f_3g_k- c_2e_1f_3g_k+ c_1e_2f_3g_k$$

$$i=1, 2 \quad k=i+1 \tag{14}$$

$$f_{pi}=-b_kd_3f_2g_1+ b_3d_kf_2g_1- c_ke_3f_2g_1+ c_3e_kf_2g_1+ b_kd_2f_3g_1- b_2d_kf_3g_1+ c_ke_2f_3g_1- c_2e_kf_3g_1- b_3d_2f_kg_1+ b_2d_3f_kg_1- c_3e_2f_kg_1+ c_2e_3f_kg_1+ b_kd_3f_1g_2- b_3d_kf_1g_2+ c_ke_3f_1g_2- c_3e_kf_1g_2- b_kd_1f_3g_2+ b_1d_kf_3g_2- c_ke_1f_3g_2+ c_1e_kf_3g_2+ b_3d_1f_kg_2- b_1d_3f_kg_2+ c_3e_1f_kg_2- c_1e_3f_kg_2- b_kd_2f_1g_3+ b_2d_kf_1g_3- c_ke_2f_1g_3+ c_2e_kf_1g_3+ b_kd_1f_2g_3- b_1d_kf_2g_3+ c_ke_1f_2g_3- c_1e_kf_2g_3- b_2d_1f_kg_3+ b_1d_2f_kg_3- c_2e_1f_kg_3+ c_1e_2f_kg_3+ b_3d_2f_1g_k- b_2d_3f_1g_k+ c_3e_2f_1g_k- c_2e_3f_1g_k- b_3d_1f_2g_k+ b_1d_3f_2g_k- c_3e_1f_2g_k+ c_1e_3f_2g_k+ b_2d_1f_3g_k- b_1d_2f_3g_k+ c_2e_1f_3g_k- c_1e_2f_3g_k$$

$$i=1, 2 \quad k=i+1 \tag{15}$$

$$g_{pi}=-c_kd_3f_2g_1+ c_3d_kf_2g_1+ b_ke_3f_2g_1- b_3e_kf_2g_1+ c_kd_2f_3g_1- c_2d_kf_3g_1- b_ke_2f_3g_1+ b_2e_kf_3g_1- c_3d_2f_kg_1+ c_2d_3f_kg_1+ b_3e_2f_kg_1- b_2e_3f_kg_1+ c_kd_3f_1g_2- c_3d_kf_1g_2- b_ke_3f_1g_2+ b_3e_kf_1g_2- c_kd_1f_3g_2+ c_1d_kf_3g_2+ b_ke_1f_3g_2- b_1e_kf_3g_2+ c_3d_1f_kg_2- c_1d_3f_kg_2- b_3e_1f_kg_2+ b_1e_3f_kg_2- c_kd_2f_1g_3+ c_2d_kf_1g_3+ b_ke_2f_1g_3- b_2e_kf_1g_3+ c_kd_1f_2g_3- c_1d_kf_2g_3- b_ke_1f_2g_3+ b_1e_kf_2g_3- c_2d_1f_kg_3+ c_1d_2f_kg_3+ b_2e_1f_kg_3- b_1e_2f_kg_3+ c_3d_2f_1g_k- c_2d_3f_1g_k- b_3e_2f_1g_k+ b_2e_3f_1g_k- c_3d_1f_2g_k+ c_1d_3f_2g_k+ b_3e_1f_2g_k- b_1e_3f_2g_k+ c_2d_1f_3g_k- c_1d_2f_3g_k- b_2e_1f_3g_k+ b_1e_2f_3g_k$$

$$i=1, 2 \quad k=i+1 \tag{16}$$

$$w_0=-4a_{p2}b_{p1}b_{p2}e_{p1} + 4a_{p1}b_{p2}^2e_{p1} - 4a_{p2}b_{p2}c_{p1}e_{p1} - 4a_{p2}b_{p1}c_{p2}e_{p1} + 8a_{p1}b_{p2}c_{p2}e_{p1} - 4a_{p2}c_{p1}c_{p2}e_{p1} + 4a_{p1}c_{p2}^2e_{p1} + 4a_{p2}^2e_{p1}^2 + 4a_{p2}b_{p1}^2e_{p2} - 4a_{p1}b_{p1}b_{p2}e_{p2} + 8a_{p2}b_{p1}c_{p1}e_{p2} - 4a_{p1}b_{p2}c_{p1}e_{p2} + 4a_{p2}c_{p1}^2e_{p2} - 4a_{p1}b_{p1}c_{p2}e_{p2} - 4a_{p1}c_{p1}c_{p2}e_{p2} - 8a_{p1}a_{p2}e_{p1}e_{p2} + 4a_{p1}^2e_{p2}^2 - 4a_{p2}b_{p1}b_{p2}f_{p1} + 4a_{p1}b_{p2}^2f_{p1} - 4a_{p2}b_{p2}c_{p1}f_{p1} - 4a_{p2}b_{p1}c_{p2}f_{p1} + 8a_{p1}b_{p2}c_{p2}f_{p1} - 4a_{p2}c_{p1}c_{p2}f_{p1} + 4a_{p1}c_{p2}^2f_{p1} + 8a_{p2}^2e_{p1}f_{p1} - 8a_{p1}a_{p2}e_{p2}f_{p1} + 4a_{p2}^2f_{p1}^2 + 4a_{p2}b_{p1}^2f_{p2} - 4a_{p1}b_{p1}b_{p2}f_{p2} + 8a_{p2}b_{p1}c_{p1}f_{p2} - 4a_{p1}b_{p2}c_{p1}f_{p2} + 4a_{p2}c_{p1}^2f_{p2} - 4a_{p1}b_{p1}c_{p2}f_{p2} - 4a_{p1}c_{p1}c_{p2}f_{p2} - 8a_{p1}a_{p2}e_{p1}f_{p2} + 8a_{p1}^2e_{p2}f_{p2} - 8a_{p1}a_{p2}f_{p1}f_{p2} + 4a_{p1}^2f_{p2}^2 \tag{19}$$

$$w_1=-16a_{p2}b_{p2}d_{p1}e_{p1} - 16a_{p2}c_{p2}d_{p1}e_{p1} - 16a_{p2}b_{p1}d_{p2}e_{p1} + 32a_{p1}b_{p2}d_{p2}e_{p1} - 16a_{p2}c_{p1}d_{p2}e_{p1} + 32a_{p1}c_{p2}d_{p2}e_{p1} + 32a_{p2}b_{p1}d_{p1}e_{p2} - 16a_{p1}b_{p2}d_{p1}e_{p2} + 32a_{p2}c_{p1}d_{p1}e_{p2} - 16a_{p1}c_{p2}d_{p1}e_{p2} - 16a_{p1}b_{p1}d_{p2}e_{p2} - 16a_{p1}c_{p1}d_{p2}e_{p2} - 16a_{p2}b_{p2}d_{p1}f_{p1} - 16a_{p2}c_{p2}d_{p1}f_{p1} - 16a_{p2}b_{p1}d_{p2}f_{p1} + 32a_{p1}b_{p2}d_{p2}f_{p1} - 16a_{p2}c_{p1}d_{p2}f_{p1} + 32a_{p1}c_{p2}d_{p2}f_{p1} + 32a_{p2}b_{p1}d_{p1}f_{p2} - 16a_{p1}b_{p2}d_{p1}f_{p2} + 32a_{p2}c_{p1}d_{p1}f_{p2} - 16a_{p1}c_{p2}d_{p1}f_{p2} - 16a_{p1}b_{p1}d_{p2}f_{p2} - 16a_{p1}c_{p1}d_{p2}f_{p2} - 16a_{p2}b_{p1}b_{p2}g_{p1} + 16a_{p1}b_{p2}^2g_{p1} - 16a_{p2}b_{p2}c_{p1}g_{p1} - 16a_{p2}b_{p1}c_{p2}g_{p1} + 32a_{p1}b_{p2}c_{p2}g_{p1} - 16a_{p2}c_{p1}c_{p2}g_{p1} + 16a_{p1}c_{p2}^2g_{p1} + 32a_{p2}^2e_{p1}g_{p1} - 32a_{p1}a_{p2}e_{p2}g_{p1} + 32a_{p2}^2f_{p1}g_{p1} - 32a_{p1}a_{p2}f_{p2}g_{p1} + 16a_{p2}b_{p1}^2g_{p2} - 16a_{p1}b_{p1}b_{p2}g_{p2} + 32a_{p2}b_{p1}c_{p1}g_{p2} - 16a_{p1}b_{p2}c_{p1}g_{p2} + 16a_{p2}c_{p1}^2g_{p2} - 16a_{p1}b_{p1}c_{p2}g_{p2} - 16a_{p1}c_{p1}c_{p2}g_{p2} - 32a_{p1}a_{p2}e_{p1}g_{p2} + 32a_{p1}^2e_{p2}g_{p2} - 32a_{p1}a_{p2}f_{p1}g_{p2} + 32a_{p1}^2f_{p2}g_{p2} \tag{20}$$

$$w_2=-24a_{p2}b_{p1}b_{p2}e_{p1} + 72a_{p1}^2b_{p2}^2e_{p1} + 8a_{p2}b_{p2}c_{p1}e_{p1} + 8a_{p2}b_{p1}c_{p2}e_{p1} - 16a_{p1}b_{p2}c_{p2}e_{p1} + 40a_{p2}c_{p1}c_{p2}e_{p1} - 40a_{p1}c_{p2}^2e_{p1} - 64a_{p2}d_{p1}d_{p2}e_{p1} + 64a_{p1}d_{p2}^2e_{p1} + 24a_{p2}^2e_{p1}^2 + 24a_{p2}b_{p1}^2e_{p2} - 24a_{p1}b_{p1}b_{p2}e_{p2} - 16a_{p2}b_{p1}c_{p1}e_{p2} + 8a_{p1}b_{p2}c_{p1}e_{p2} - 40a_{p2}c_{p1}^2e_{p2} + 8a_{p1}b_{p1}c_{p2}e_{p2} + 40a_{p1}c_{p1}c_{p2}e_{p2} + 64a_{p2}d_{p1}^2e_{p2} - 64a_{p1}d_{p1}d_{p2}e_{p2} - 48a_{p1}a_{p2}e_{p1}e_{p2} + 8a_{p2}b_{p1}b_{p2}f_{p1} - 24a_{p1}^2b_{p2}^2f_{p1} + 40a_{p2}b_{p2}c_{p1}f_{p1} + 40a_{p2}b_{p1}c_{p2}f_{p1} -$$

$$\begin{aligned}
&80a_{p1}b_{p2}c_{p2}f_{p1} + 72a_{p2}c_{p1}c_{p2}f_{p1} - 72a_{p1}c_{p2}^2f_{p1} - \\
&64a_{p2}d_{p1}d_{p2}f_{p1} + 64a_{p1}d_{p2}^2f_{p1} - 16a_{p2}^2e_{p1}f_{p1} + \\
&16a_{p1}a_{p2}e_{p2}f_{p1} - 40a_{p2}^2f_{p1}^2 - 8a_{p2}b_{p1}^2f_{p2} + \\
&8a_{p1}b_{p1}b_{p2}f_{p2} - 80a_{p2}b_{p1}c_{p1}f_{p2} + 40a_{p1}b_{p2}c_{p1}f_{p2} - \\
&72a_{p2}c_{p1}^2f_{p2} + 40a_{p1}b_{p1}c_{p2}f_{p2} + 72a_{p1}c_{p1}c_{p2}f_{p2} + \\
&64a_{p2}d_{p1}^2f_{p2} - 64a_{p1}d_{p1}d_{p2}f_{p2} + 16a_{p1}a_{p2}e_{p1}f_{p2} - \\
&16a_{p1}^2e_{p2}f_{p2} + 80a_{p1}a_{p2}f_{p1}f_{p2} - 40a_{p1}^2f_{p2}^2 - \\
&64a_{p2}b_{p2}d_{p1}g_{p1} - 64a_{p2}c_{p2}d_{p1}g_{p1} - 64a_{p2}b_{p1}d_{p2}g_{p1} + \\
&128a_{p1}b_{p2}d_{p2}g_{p1} - 64a_{p2}c_{p1}d_{p2}g_{p1} + \\
&128a_{p1}c_{p2}d_{p2}g_{p1} + 64a_{p2}^2g_{p1}^2 + 128a_{p2}b_{p1}d_{p1}g_{p2} - \\
&64a_{p1}b_{p2}d_{p1}g_{p2} + 128a_{p2}c_{p1}d_{p1}g_{p2} - 64a_{p1}c_{p2}d_{p1}g_{p2} - \\
&64a_{p1}b_{p1}d_{p2}g_{p2} - 64a_{p1}c_{p1}d_{p2}g_{p2} - \\
&128a_{p1}a_{p2}g_{p1}g_{p2} + 64a_{p1}^2g_{p2}^2 \qquad (21)
\end{aligned}$$

$$\begin{aligned}
w_3 = &-48a_{p2}b_{p2}d_{p1}e_{p1} + 80a_{p2}c_{p2}d_{p1}e_{p1} - \\
&48a_{p2}b_{p1}d_{p2}e_{p1} + 96a_{p1}b_{p2}d_{p2}e_{p1} + 80a_{p2}c_{p1}d_{p2}e_{p1} - \\
&160a_{p1}c_{p2}d_{p2}e_{p1} + 96a_{p2}b_{p1}d_{p1}e_{p2} - 48a_{p1}b_{p2}d_{p1}e_{p2} - \\
&160a_{p2}c_{p1}d_{p1}e_{p2} + 80a_{p1}c_{p2}d_{p1}e_{p2} - 48a_{p1}b_{p1}d_{p2}e_{p2} + \\
&80a_{p1}c_{p1}d_{p2}e_{p2} + 80a_{p2}b_{p2}d_{p1}f_{p1} + 208a_{p2}c_{p2}d_{p1}f_{p1} + \\
&80a_{p2}b_{p1}d_{p2}f_{p1} - 160a_{p1}b_{p2}d_{p2}f_{p1} + 208a_{p2}c_{p1}d_{p2}f_{p1} - \\
&416a_{p1}c_{p2}d_{p2}f_{p1} - 160a_{p2}b_{p1}d_{p1}f_{p2} + 80a_{p1}b_{p2}d_{p1}f_{p2} - \\
&416a_{p2}c_{p1}d_{p1}f_{p2} + 208a_{p1}c_{p2}d_{p1}f_{p2} + 80a_{p1}b_{p1}d_{p2}f_{p2} + \\
&208a_{p1}c_{p1}d_{p2}f_{p2} - 48a_{p2}b_{p1}b_{p2}g_{p1} + 48a_{p1}b_{p2}^2g_{p1} + \\
&80a_{p2}b_{p2}c_{p1}g_{p1} + 80a_{p2}b_{p1}c_{p2}g_{p1} - 160a_{p1}b_{p2}c_{p2}g_{p1} + \\
&208a_{p2}c_{p1}c_{p2}g_{p1} - 208a_{p1}c_{p2}^2g_{p1} - 256a_{p2}d_{p1}d_{p2}g_{p1} + \\
&256a_{p1}d_{p2}^2g_{p1} + 96a_{p2}^2e_{p1}g_{p1} - 96a_{p1}a_{p2}e_{p2}g_{p1} - \\
&160a_{p2}^2f_{p1}g_{p1} + 160a_{p1}a_{p2}f_{p2}g_{p1} + 48a_{p2}b_{p1}^2g_{p2} - \\
&48a_{p1}b_{p1}b_{p2}g_{p2} - 160a_{p2}b_{p1}c_{p1}g_{p2} + 80a_{p1}b_{p2}c_{p1}g_{p2} - \\
&208a_{p2}c_{p1}^2g_{p2} + 80a_{p1}b_{p1}c_{p2}g_{p2} + 208a_{p1}c_{p1}c_{p2}g_{p2} + \\
&256a_{p2}d_{p1}^2g_{p2} - 256a_{p1}d_{p1}d_{p2}g_{p2} - 96a_{p1}a_{p2}e_{p1}g_{p2} + \\
&96a_{p1}^2e_{p2}g_{p2} + 160a_{p1}a_{p2}f_{p1}g_{p2} - 160a_{p1}^2f_{p2}g_{p2} \qquad (22)
\end{aligned}$$

$$\begin{aligned}
w_4 = &-60a_{p2}b_{p1}b_{p2}e_{p1} + 60a_{p1}b_{p2}^2e_{p1} + \\
&68a_{p2}b_{p2}c_{p1}e_{p1} + 68a_{p2}b_{p1}c_{p2}e_{p1} - 136a_{p1}b_{p2}c_{p2}e_{p1} - \\
&60a_{p2}c_{p1}c_{p2}e_{p1} + 60a_{p1}c_{p2}^2e_{p1} + 60a_{p2}^2e_{p1}^2 + \\
&60a_{p2}b_{p1}^2e_{p2} - 60a_{p1}b_{p1}b_{p2}e_{p2} - 136a_{p2}b_{p1}c_{p1}e_{p2} + \\
&68a_{p1}b_{p2}c_{p1}e_{p2} + 60a_{p2}c_{p1}^2e_{p2} + 68a_{p1}b_{p1}c_{p2}e_{p2} - \\
&60a_{p1}c_{p1}c_{p2}e_{p2} - 120a_{p1}a_{p2}e_{p1}e_{p2} + 60a_{p1}^2e_{p2}^2 + \\
&68a_{p2}b_{p1}b_{p2}f_{p1} - 68a_{p1}b_{p2}^2f_{p1} - 60a_{p2}b_{p2}c_{p1}f_{p1} - \\
&60a_{p2}b_{p1}c_{p2}f_{p1} + 120a_{p1}b_{p2}c_{p2}f_{p1} - 444a_{p2}c_{p1}c_{p2}f_{p1} + \\
&444a_{p1}c_{p2}^2f_{p1} + 512a_{p2}d_{p1}d_{p2}f_{p1} - 512a_{p1}d_{p2}^2f_{p1} - \\
&136a_{p2}^2e_{p1}f_{p1} + 136a_{p1}a_{p2}e_{p2}f_{p1} + 60a_{p2}^2f_{p1}^2 - \\
&68a_{p2}b_{p1}^2f_{p2} + 68a_{p1}b_{p1}b_{p2}f_{p2} + 120a_{p2}b_{p1}c_{p1}f_{p2} - \\
&60a_{p1}b_{p2}c_{p1}f_{p2} + 444a_{p2}c_{p1}^2f_{p2} - 60a_{p1}b_{p1}c_{p2}f_{p2} - \\
&444a_{p1}c_{p1}c_{p2}f_{p2} - 512a_{p2}d_{p1}^2f_{p2} + 512a_{p1}d_{p1}d_{p2}f_{p2} + \\
&136a_{p1}a_{p2}e_{p1}f_{p2} - 136a_{p1}^2e_{p2}f_{p2} - 120a_{p1}a_{p2}f_{p1}f_{p2} + \\
&60a_{p1}^2f_{p2}^2 + 512a_{p2}c_{p2}d_{p1}g_{p1} + 512a_{p2}c_{p1}d_{p2}g_{p1} - \\
&1024a_{p1}c_{p2}d_{p2}g_{p1} - 1024a_{p2}c_{p1}d_{p1}g_{p2} + \\
&512a_{p1}c_{p2}d_{p1}g_{p2} + 512a_{p1}c_{p1}d_{p2}g_{p2} \qquad (23)
\end{aligned}$$

$$\begin{aligned}
w_5 = &-32a_{p2}b_{p2}d_{p1}e_{p1} + 96a_{p2}c_{p2}d_{p1}e_{p1} - \\
&32a_{p2}b_{p1}d_{p2}e_{p1} + 64a_{p1}b_{p2}d_{p2}e_{p1} + 96a_{p2}c_{p1}d_{p2}e_{p1} - \\
&192a_{p1}c_{p2}d_{p2}e_{p1} + 64a_{p2}b_{p1}d_{p1}e_{p2} - 32a_{p1}b_{p2}d_{p1}e_{p2} - \\
&192a_{p2}c_{p1}d_{p1}e_{p2} + 96a_{p1}c_{p2}d_{p1}e_{p2} - 32a_{p1}b_{p1}d_{p2}e_{p2} + \\
&96a_{p1}c_{p1}d_{p2}e_{p2} + 96a_{p2}b_{p2}d_{p1}f_{p1} - 800a_{p2}c_{p2}d_{p1}f_{p1} + \\
&96a_{p2}b_{p1}d_{p2}f_{p1} - 192a_{p1}b_{p2}d_{p2}f_{p1} - 800a_{p2}c_{p1}d_{p2}f_{p1} + \\
&1600a_{p1}c_{p2}d_{p2}f_{p1} - 192a_{p2}b_{p1}d_{p1}f_{p2} + \\
&96a_{p1}b_{p2}d_{p1}f_{p2} + 1600a_{p2}c_{p1}d_{p1}f_{p2} - \\
&800a_{p1}c_{p2}d_{p1}f_{p2} + 96a_{p1}b_{p1}d_{p2}f_{p2} - 800a_{p1}c_{p1}d_{p2}f_{p2} - \\
&32a_{p2}b_{p1}b_{p2}g_{p1} + 32a_{p1}b_{p2}^2g_{p1} + 96a_{p2}b_{p2}c_{p1}g_{p1} + \\
&96a_{p2}b_{p1}c_{p2}g_{p1} - 192a_{p1}b_{p2}c_{p2}g_{p1} - \\
&800a_{p2}c_{p1}c_{p2}g_{p1} + 800a_{p1}c_{p2}^2g_{p1} + 768a_{p2}d_{p1}d_{p2}g_{p1} - \\
&768a_{p1}d_{p2}^2g_{p1} + 64a_{p2}^2e_{p1}g_{p1} - 64a_{p1}a_{p2}e_{p2}g_{p1} - \\
&192a_{p2}^2f_{p1}g_{p1} + 192a_{p1}a_{p2}f_{p2}g_{p1} + 32a_{p2}b_{p1}^2g_{p2} - \\
&32a_{p1}b_{p1}b_{p2}g_{p2} - 192a_{p2}b_{p1}c_{p1}g_{p2} + 96a_{p1}b_{p2}c_{p1}g_{p2} + \\
&800a_{p2}c_{p1}^2g_{p2} + 96a_{p1}b_{p1}c_{p2}g_{p2} - 800a_{p1}c_{p1}c_{p2}g_{p2} - \\
&768a_{p2}d_{p1}^2g_{p2} + 768a_{p1}d_{p1}d_{p2}g_{p2} - 64a_{p1}a_{p2}e_{p1}g_{p2} + \\
&64a_{p1}^2e_{p2}g_{p2} + 192a_{p1}a_{p2}f_{p1}g_{p2} - 192a_{p1}^2f_{p2}g_{p2} \qquad (24)
\end{aligned}$$

$$\begin{aligned}
w_6 = &-80a_{p2}b_{p1}b_{p2}e_{p1} + 80a_{p1}b_{p2}^2e_{p1} + \\
&112a_{p2}b_{p2}c_{p1}e_{p1} + 112a_{p2}b_{p1}c_{p2}e_{p1} - \\
&224a_{p1}b_{p2}c_{p2}e_{p1} - 208a_{p2}c_{p1}c_{p2}e_{p1} + 208a_{p1}c_{p2}^2e_{p1} + \\
&128a_{p2}d_{p1}d_{p2}e_{p1} - 128a_{p1}d_{p2}^2e_{p1} + 80a_{p2}^2e_{p1}^2 + \\
&80a_{p2}b_{p1}^2e_{p2} - 80a_{p1}b_{p1}b_{p2}e_{p2} - 224a_{p2}b_{p1}c_{p1}e_{p2} + \\
&112a_{p1}b_{p2}c_{p1}e_{p2} + 208a_{p2}c_{p1}^2e_{p2} + 112a_{p1}b_{p1}c_{p2}e_{p2} - \\
&208a_{p1}c_{p1}c_{p2}e_{p2} - 128a_{p2}d_{p1}^2e_{p2} + 128a_{p1}d_{p1}d_{p2}e_{p2} - \\
&160a_{p1}a_{p2}e_{p1}e_{p2} + 80a_{p1}^2e_{p2}^2 + 112a_{p2}b_{p1}b_{p2}f_{p1} - \\
&112a_{p1}b_{p2}^2f_{p1} - 208a_{p2}b_{p2}c_{p1}f_{p1} - 208a_{p2}b_{p1}c_{p2}f_{p1} + \\
&416a_{p1}b_{p2}c_{p2}f_{p1} + 1008a_{p2}c_{p1}c_{p2}f_{p1} - 1008a_{p1}c_{p2}^2f_{p1} - \\
&896a_{p2}d_{p1}d_{p2}f_{p1} + 896a_{p1}d_{p2}^2f_{p1} - 224a_{p2}^2e_{p1}f_{p1} + \\
&224a_{p1}a_{p2}e_{p2}f_{p1} + 208a_{p2}^2f_{p1}^2 - 112a_{p2}b_{p1}^2f_{p2} + \\
&112a_{p1}b_{p1}b_{p2}f_{p2} + 416a_{p2}b_{p1}c_{p1}f_{p2} - \\
&208a_{p1}b_{p2}c_{p1}f_{p2} - 1008a_{p2}c_{p1}^2f_{p2} - 208a_{p1}b_{p1}c_{p2}f_{p2} + \\
&1008a_{p1}c_{p1}c_{p2}f_{p2} + 896a_{p2}d_{p1}^2f_{p2} - 896a_{p1}d_{p1}d_{p2}f_{p2} + \\
&224a_{p1}a_{p2}e_{p1}f_{p2} - 224a_{p1}^2e_{p2}f_{p2} - 416a_{p1}a_{p2}f_{p1}f_{p2} + \\
&208a_{p1}^2f_{p2}^2 + 128a_{p2}b_{p2}d_{p1}g_{p1} - 896a_{p2}c_{p2}d_{p1}g_{p1} + \\
&128a_{p2}b_{p1}d_{p2}g_{p1} - 256a_{p1}b_{p2}d_{p2}g_{p1} - \\
&896a_{p2}c_{p1}d_{p2}g_{p1} + 1792a_{p1}c_{p2}d_{p2}g_{p1} - 128a_{p2}^2g_{p1}^2 - \\
&256a_{p2}b_{p1}d_{p1}g_{p2} + 128a_{p1}b_{p2}d_{p1}g_{p2} + \\
&1792a_{p2}c_{p1}d_{p1}g_{p2} - 896a_{p1}c_{p2}d_{p1}g_{p2} + \\
&128a_{p1}b_{p1}d_{p2}g_{p2} - 896a_{p1}c_{p1}d_{p2}g_{p2} + \\
&256a_{p1}a_{p2}g_{p1}g_{p2} - 128a_{p1}^2g_{p2}^2 \qquad (25)
\end{aligned}$$

APPENDIX B. Comparison of the absolute maximum error with available literature

Reference	Mechanism configuration	Function	Input Range	Maximum Error (in absolute value)	
Our study	Slider-crank mechanism	$y = \sin(x)$	$0° \leq x \leq 90°$	Precision Point:	-0.00014533
				Sub-domain:	0.00025793
				Galerkin:	-0.00010383
		$y = \tan(x)$	$0° \leq x \leq 45°$	Precision Point:	-0.00011431
				Sub-domain:	-0.00102642
				Galerkin:	-0.00053734
		$y = e^x$	$0 \leq x \leq 1$	Precision Point:	0.00027071
				Sub-domain:	-0.00069492
				Galerkin:	-0.00037269
		$y = \ln(x)$	$1 \leq x \leq 2$	Precision Point:	0.00025632
				Sub-domain:	-0.00080016
				Galerkin:	-0.00055926
Singh et al. 2005	Four-bar mechanism	$y = \sin(x)$	$0° \leq x \leq 90°$	-0.012573	
		$y = \tan(x)$	$0° \leq x \leq 45°$	-0.004634	
		$y = e^x$	$0 \leq x \leq 1$	-0.000489	
		$y = \ln(x)$	$1 \leq x \leq 2$	0.002359	
Akçalı and Dittrich 1989	Four-bar mechanism	$y = \sin(x)$	$0° \leq x \leq 90°$	-0.0630	
		$y = \tan(x)$	$0° \leq x \leq 45°$	-0.0015	
Jaiswal and Jawale 2018	Four-bar mechanism	$y = \sin(x)$	$0° \leq x \leq 90°$	0.002666	
		$y = \tan(x)$	$0° \leq x \leq 45°$	0.000821	
		$y = e^x$	$0 \leq x \leq 1$	0.000203	
		$y = \ln(x)$	$1 \leq x \leq 2$	0.000046	
Mehar et al. 2015	Four-bar mechanism	$y = \tan(x)$	$0° \leq x \leq 45°$	0.0010	
		$y = e^x$	$0 \leq x \leq 1$	0.00094218	
		$y = \ln(x)$	$1 \leq x \leq 2$	0.000059580	

Turkish Journal of Engineering

https://dergipark.org.tr/en/pub/tuje

e-ISSN 2587-1366

Image processing based autonomous landing zone detection for a multi-rotor drone in emergency situations

Veysel Turan [1], Ercan Avşar *[1], Davood Asadihendoustani [2], Emine Avşar Aydın[2]

[1]Çukurova University, Faculty of Engineering, Department of Electrical and Electronics Engineering, Adana, Turkey
[2]Adana Alparslan Türkeş Science and Technology University, Faculty of Aeronautics and Astronautics, Department of Aerospace Engineering, Adana, Turkey

Keywords
Autonomus landing
Image processing
Object detection
UAV

ABSTRACT

Flight safety and reliability improvement is an important research issue in aerial applications. Multi-rotor drones are vulnerable to motor failures leading to potentially unsafe operations or collisions. Therefore, researchers are working on autonomous landing systems to safely recover and land the faulty drone in on a desired landing area. In such a case, a suitable landing zone should be detected rapidly in for emergency landing. Majority of the works related with autonomous landing utilize a marker and GPS signals to detect landing site. In this work, we propose a landing system framework that involves only the processing of images taken from the onboard camera of the vehicle. First, the objects in the image are determined by filtering and edge detection algorithm, then the most suitable landing zone is searched. The area that is free from obstacles and closest to the center of the image is defined as the most immediate and suitable landing zone. The method has been tested on 25 images taken from different heights and its performance has been evaluated in terms runtime on a single board computer and detection precision and recall values. The average measured runtime is 2.4923 seconds and 100% of precision and recall values are achieved for the images taken from 1m and 2m. The smallest precision and recall values are 79.1% and 81.2%, respectively.

1. INTRODUCTION

The use of Unmanned Aerial Vehicles (UAV) has increased at an unpredictable rate in recent years. Although these devices have been used particularly in military applications for a long time, their use in non-military applications such as fire extinguishing (Aydin et al. 2019), meteorological research (Martin et al. 2010; PropotoUAV 2019), exploration (Jakob et al. 2016; Heincke et al. 2019) and agricultural activities (Veroustraete 2015) have become very widespread nowadays. Quadrotors are the most common devices to use among UAV types due to their uncomplicated mechanical structures. Quadrotors can fulfill 3D motion tracking requirements with various technical systems such as Global Positioning System (GPS), ultrasonic detection, angular velocity sensors and linear accelerometers (Zhao and Wang 2012). Despite the use of these integrated systems and sensors, the control of the quadrotors is still one of the most difficult issues, but research and development activities continue in many research centers (Hoffmann et al. 2007; Zhao and Wang 2012). The vast majority of research activities address control issues during flying. The ultimate goal of UAV systems is to reach fully autonomous operations (Kim and Sukkarieh 2002).

One of the most important issue for UAV is autonomous landing in motion. Meanwhile, demands for automatic landing of drones on a defined position, safely, accurately, and without human's intervention, increase every day. It is always possible for a UAV to unavoidably face emergencies during flight, such as engine failure, interruption of data link from the ground and other unexpected accidents (strong wind, rain, etc.). Thus, forced landing measures should urgently be adopted in such situations. Methods of forced landing such as parachute and other flight termination systems can cause damage on the body of the multi-rotor (Fitzgerald et al., 2005). In addition, GPS signals are highly susceptible to be interrupted especially at lower altitudes (Lee et al.

---

* **Corresponding Author**

*(veyselturnn@gmail.com) ORCID ID 0000 – 0002 – 0197 – 5227
(ercanavsar@cu.edu.tr) ORCID ID 0000 – 0002 – 1356 – 2753
(dasadihendoustani@atu.edu.tr) ORCID ID 0000 – 0002 – 2066 – 6016
(eaydin@atu.edu.tr) ORCID ID 0000 – 0002 – 5068 - 2957

Cite this article

Turan V, Avşar E, Asadihendoustani D & Aydın E A (2021). Image processing based autonomous landing zone detection for a multi-rotor drone in emergency situations. Turkish Journal of Engineering, 5(4), 193-200

Research Article / DOI: XXXXXXXXXXXX

Received: 29/05/2020; Accepted: 20/07/2020

2012; Ho 2017), and in indoor environments. Furthermore, GPS signals are controlled by other nations, which causes vulnerability issues. For instance, in 29*th* October 2018, the GPS jamming that caused 46 drones to plummet during a display over Victoria Harbour caused at least HK$1 million (US$127,500) of damage, according to a senior official from the Hong Kong Tourism Board (Liteye 2018). As a result, some alternative methods were adopted to minimize the damage on that UAVs by enabling them to autonomously find a safe area suitable for landing. Some studies about forced landing in emergency situations for UAVs were presented in indoor environment without using GPS (Nemati et al. 2015).

In the past years, in design of emergency landing systems, effective algorithms of machine learning such as Support Vector Machines (SVM) and Artificial Neural Networks (ANN) were utilized in combination with digital image processing techniques for selection of appropriate landing site (Guo et al. 2014, Lunghi et al. 2015). It is observed that the above mentioned machine learning algorithms have different performance constraints, e.g. SVM is complex and requires huge computational power, whereas, ANN requires large training data set which corresponds to greater training time. Due to these constraints, both algorithms cannot meet the rapidly changing requirements for landing area selection in emergency flight conditions. For instance, in a previous study about detection of forced landing sites, 901 images were used to train and test of an ANN model (Fitzgerald and Walker 2005). Because the images fed to the ANN model were not representative of the training set, the final classification accuracy is very low when compared to training accuracy (Lu et al. 2013). Thus, that situation prevents it from being completely reliable.

Image processing is an appropriate and reliable way to find safe landing sites in case of an emergency. This is generally accomplished by detection of objects in the images taken from UAVs. Most of the related studies are about detection of some “marker” in an image (Barták et al. 2014; Cabrera-Ponce and Martinez-Carranza, 2017; Sani and Karimian 2017) which represents the desired landing spot. Utilization of a marker may not be a feasible way for emergency landing conditions. Since markers can be far from the UAV then it will take time to find the markers. For instance, the recent demonstration of package delivery using an UAV by Amazon shows the feasibility of an UAV sending a package to its consumer (AMAZON 2017). A marker which is placed by the consumer on the ground is used to allow the UAV to land safely. In some circumstances where the marker is unavailable or inappropriately placed, these vehicles need to be able to sense and avoid the surrounding objects in the environment and perform a smooth descent automatically. Without this capability, the safety of the surrounding animals, humans, and property cannot be ensured. Additionally, in some emergency situations, the UAV needs to land as quickly as possible. Therefore, it is essential to select a safe landing spot automatically and emergently, without depending on external systems.

Motivated by the above reasons, in this paper, an image processing method for object detection is proposed. The method is developed to work on the images taken from a drone’s onboard camera. The aim is to rapidly detect a suitable landing zone in an unstructured and unknown environment. The method initially proposes a candidate landing zone at the center of the image. If the initial proposal is not suitable then new candidates in the neighboring area are evaluated until an available spot is detected (Fig. 1). The suitability of a spot is determined by existence of an object inside it. The object detection is accomplished by means of several image processing methods including edge detection, color processing, morphologic operations and thresholding. The major advantages of the method are (i) no requirement for a marker and (ii) no need for huge amount of data for training a model.

2. METHOD

2.1. The Landing System Framework

The use of multi-rotor drones has undeniably increased in the past decade, both in the military and civilian applications, thus raising a number of vital unsolved issues including safety and reliability. Engine malfunction or failures are among the common faults in multi-rotor drones, which apparently endanger the drone and the people's safety on the ground. In order to increase flight safety and reliability of drones, researchers are working on automation enhancement to safely recover the impaired drone (Lopez-Franco et al. 2017; Mazeh et al. 2018; Nguyen et al. 2019).

There are several challenges related with safe recovery or landing of impaired aerial vehicles. Majority of these challenges are about obstacle detection, suitable landing site detection/selection, fault detection and identification, characterizing the aircraft’s new kinematic constraints, trajectory planning, and control of the faulty aircraft on the landing trajectory. To cover these challenges, an emergency landing system has been proposed according to Fig. 1. In fault or failure scenarios where continuation of flight is not possible or endangers the flight safety, the emergency flight system is triggered to recover drone’s stability and safely land the drone on a suitable landing site.

The emergency landing system is translated to an architecture consisting of various subsystems that are capable of landing a faulty drone to a desired landing site along a designed trajectory without colliding to any human or animal. The architecture autonomously detects objects as well as possible landing sites, determines the most suitable landing site, develops the landing trajectory based on new kinematic and dynamic constraints of impaired drone, and controls it to the landing site, using onboard camera data and other common sensor information like IMU (Inertial Measurement Unit).

2.2. Landing Zone Detection

Emergency landing mode of the UAV is activated whenever a fault in any of the motors is detected. Then the onboard camera is immediately triggered to take a top-view photo of the ground in perpendicular direction. This image is the field of view (FOV) of the UAV and it constitutes the search space for finding a suitable landing zone. In such an emergency situation, locating the appropriate zone in a short time is very important. Therefore, the algorithm starts checking the suitability of center of the image which denotes the closest area to the UAV. If the image center is occupied by an object than it is labelled as "negative" and a neighborhood of the image center checked for suitability. The distance of the neighborhood to the image center is gradually increased until a vacant spot is found and that spot is labelled to be "positive". Next, the coordinates of this "positive" spot is sent to the flight controller to initialize the autonomous landing process. The steps for emergency landing are presented in Fig. 2.

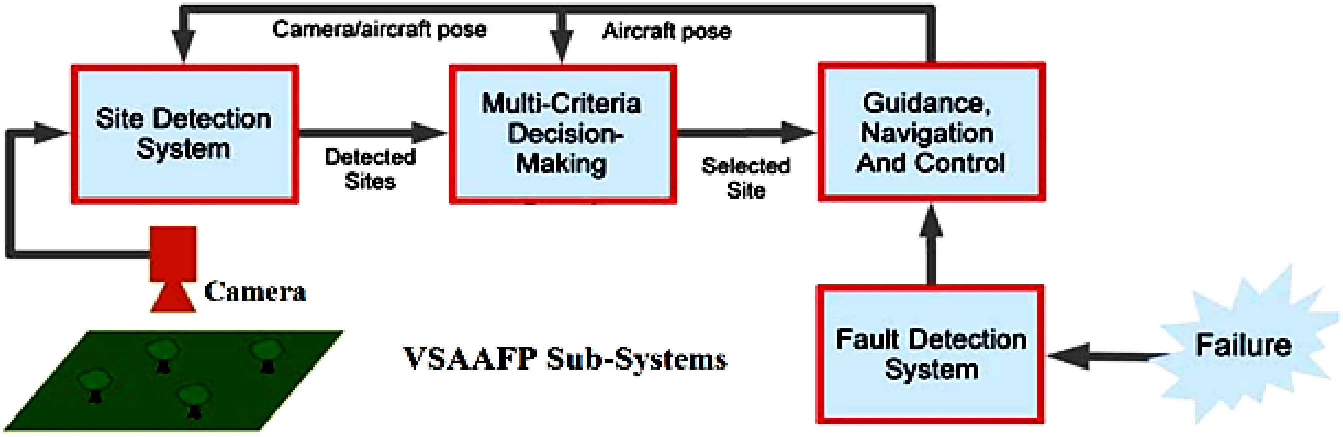

Figure 1. Emergency landing system architecture and subsystem

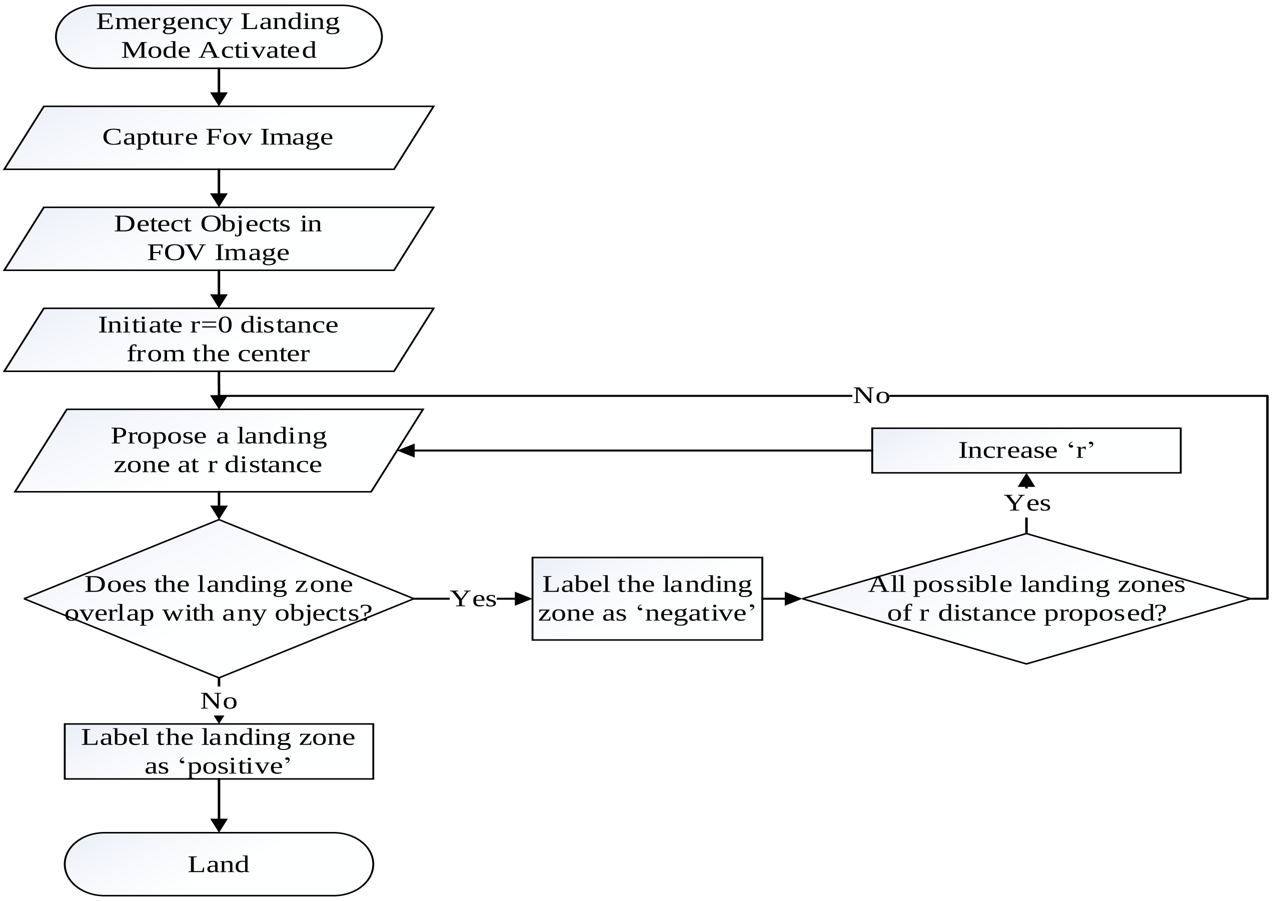

Figure 2. Suitable Landing site detection flowchart

2.2.1. Object detection in FOV images

The object detection starts with converting the FOV image into a grayscale image. This is necessary for preparing the image for canny operator, which is a method for edge detection to find objects on image. The Canny edge detector is an edge detection operator that uses a multi-stage algorithm to detect a wide range of edges in images (Canny 1986). The advantage of using Canny edge detection technique over other well-known edge detection algorithms is that it gives better results even in noisy conditions (Kumar et al. 2015).

The edge detection operator has four steps.

- Smooth an image with Gaussian filter.
- Calculate gradient magnitude and gradient direction.
- "Non - maximum suppression" to ensure the desired edge with one single pixel width.
- Determine two threshold values, and then select possible edge points and trace edges.

The first step in canny edge detector algorithm is to delete the noise in the frames by applying a Gaussian filter. In Canny algorithm, the Gaussian function is applied to smooth the image prior to edge detection. The filtering or smoothing operation actually supports two purposes. The first one is noise effect reduction prior to the detection of pixel intensity changes. The second purpose is setting the resolution or scale at which intensity changes are to be detected (Chen et al. 2014). These two purposes are necessary to improve the efficiency of edge detection method. In other words, Gaussian filtering helps reduction of detecting false edges.

Next step is to calculate the magnitude and gradient of the edges in the smoothed image. This is accomplished by filtering the smoothed image with a Sobel kernel in vertical and horizontal directions.

The complete scan of image is done after receiving gradient magnitude and direction, to remove any unwanted pixels, which may not establish the edge. In this step, just local maxima must be considered as edges through applying non-maximum suppression. Non-maximum suppression exchanges the smoothed edges in the frame of the gradient magnitudes to sharp edges. This step is necessary to keep every local maximum in the gradient image, and remove any other detected edges which are possibly false detections.

The final step of canny edge detector algorithm is hysteresis thresholding. In this step, two threshold values are selected. The edges with intensity gradient greater than the maximum threshold are labeled as "sure-edge". Similarly, the edges with intensity gradient smaller than the minimum threshold are labeled as "non-edge". Other edges between these threshold values are labeled as "sure-edge" if they are connected to another "sure-edge", otherwise labeled as "non-edge". Obviously, this step removes small edges in the images that are possibly false detections. These threshold values are the only parameters of the method and are selected as 100 and 200 in this work.

Typically, the edge lines at the output of Canny method are thin lines. Therefore, dilation is applied to binary edge image as morphological operation to thicken the line of objects on image. Because thin line may cause errors when finding a landing zone. The binary image obtained after this operation is named as objects image. The outputs of these steps are given in Fig. 3.

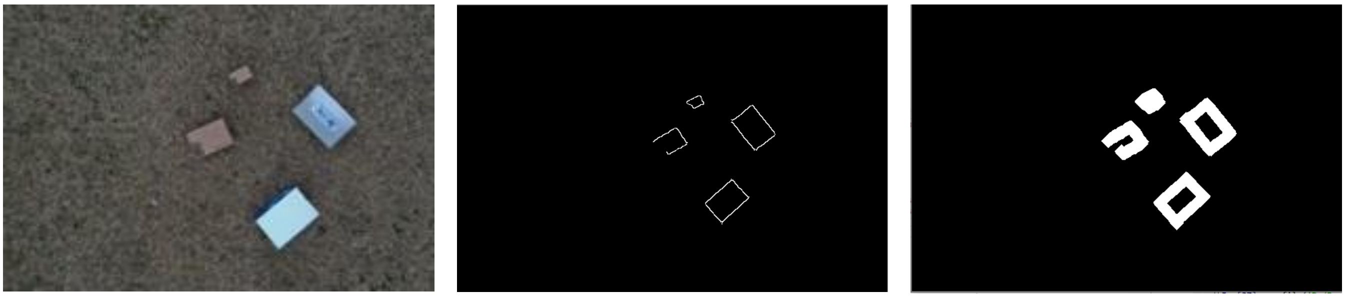
(a) (b) (c)

Figure 3. Steps of object detection. *(a)* FOV image, *(b)* Edge detection of FOV image, *(c)* Morphological operations are applied to binary image (objects image)

2.2.2. Searching for a landing zone

Once the objects in the FOV image are detected, the next step is to find the closest available zone for landing. The first parameter to consider for this step is the minimum dimensions of the suitable landing zone. Obviously, this parameter depends on the altitude at which the FOV image is taken. As illustrated in Fig. 4, in order to find a relation between the dimensions and the altitude, a calibration procedure is carried out on the images taken at five different altitudes. When the altitude is 1 meter, the ideal dimensions are 60x60 pixels; on the other hand, when the altitude is 5 meters, the ideal dimensions reduce to 20x20 pixels. The ideal dimensions for suitable landing zone change linearly with respect to altitude.

In a typical emergency landing scenario, a maximum altitude of 5 meters is appropriate for initialization of image processing tasks (Lee et al. 2014). Therefore, we used the same altitude value for our analysis as well. In case of triggering the emergency landing at a higher altitude, the UAV is initially brought to 5-meter altitude, then the image processing is activated.

After determining the optimal dimensions for landing, an available space for these dimensions is searched in the FOV image. The availability of a spot in the image is defined as the area in which no object is present. In order to check the availability, a *binary mask* is created. In the binary mask, an area with the optimal dimensions is made "1", and all the remaining area is left as "0". The area with "1" values in the binary image is the proposed region the availability of that region is checked. By observing the output of the logical AND operation between the binary mask and the objects image, it is possible to determine if a spot is available or not. If the logical AND operation returns "1" value, then it means that there is an overlap between any of the objects and the proposed region in the binary mask. Therefore, this proposed region is labeled as "negative". On the other hand, if a value of "0" is returned from the AND operation, then no overlap is present, hence the proposed region is labeled as "positive".

When a proposed region is labeled as "negative", another region should be proposed immediately until a "positive" label is achieved. Since this work concerns only with the emergency situations, the location of the first proposed region is the middle of the FOV image which is the spot that is closest to UAV. If this spot is not available then a circular vicinity of the middle point is searched for availability, and the radius of the circle is gradually increased until an available spot is found. The steps of searching for a landing zone are given in Fig. 5.

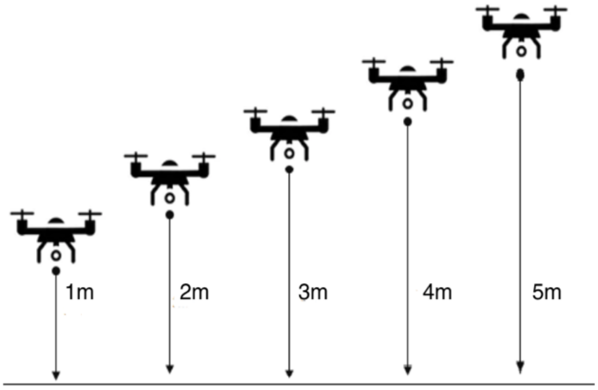

Figure 4. Ideal position to initialize the search of landing pad in different heights

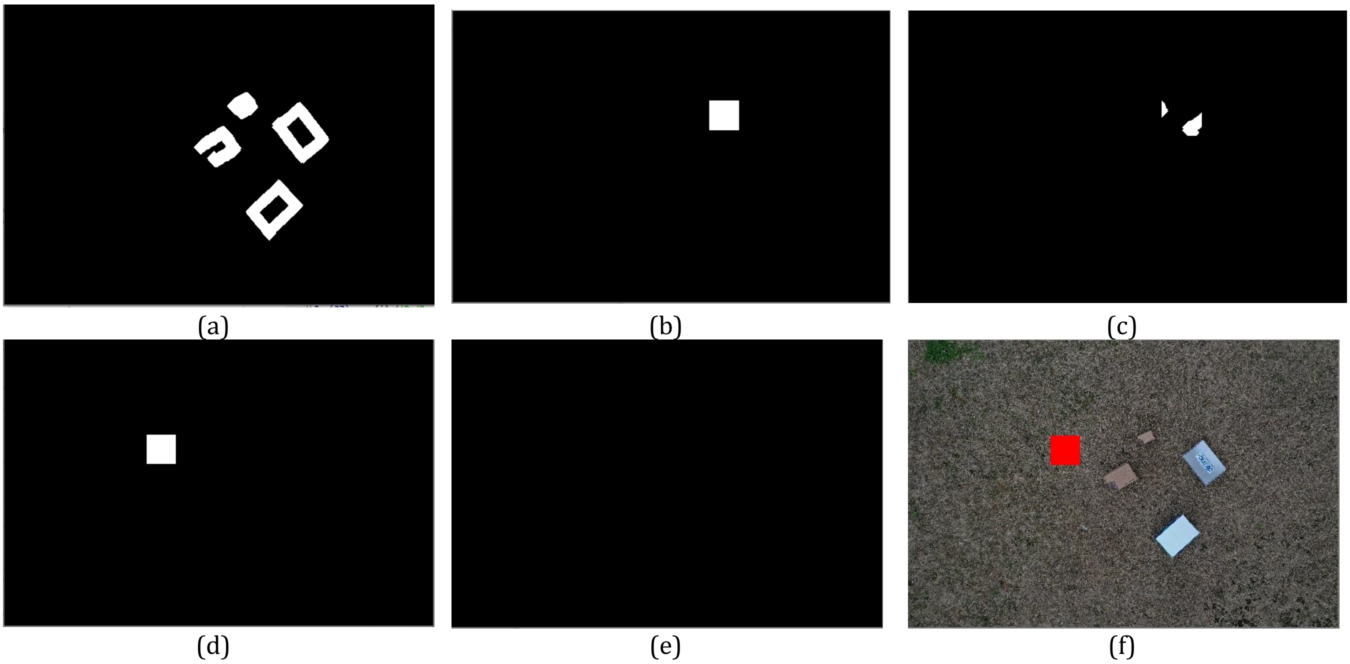
(a) (b) (c) (d) (e) (f)

Figure 5. Steps of searching for a landing zone. ***(a)*** Objects image, ***(b)*** A binary mask for proposing a region, ***(c)*** Output of AND operation between (*a*) and (*b*): "negative" labeling, ***(d)*** Another binary mask for proposing a region, ***(e)*** Output of AND operation between (*a*) and (*d*): "positive" labeling, ***(f)*** Detected landing zone shown on the FOV image

3. RESULTS AND DISCUSSION

The method has been evaluated in terms of speed (i.e. runtime) and detection performance on a set of images taken from different altitudes. Here, we define the speed as the runtime of the algorithm to find a suitable landing zone in the image. On the other hand, the detection performance is defined as precision and recall values related with the object detection in the images.

As explained earlier, the landing zone detection is a part of autonomous landing system framework for emergency situations. Hence, the entire detection task has been experimented on a single board computer, which may easily be involved in a UAV system. The single board computer used in the experiments is Raspberry Pi 3 model B that has a Broadcom BCM2837B0 chipset, Cortex-A53 (ARMv8) 64-bit processor working at 1.4GHz frequency and 1GB of memory. Besides, all the processed images have dimensions of 600 x 400 pixels.

During the experiments, it has been observed that the runtime of the algorithm for a particular image is different for consecutive runs. This may be because of the tasks related to operating system of the single board computer. Therefore, the algorithm has been run on all of the images for 10 separate times (i.e., 25 images x 10 times = 250 observations) and then some statistical values are calculated on the observed runtimes. The range of the observations is [1.3940, 2.8478] seconds where the mean and standard deviation is calculated as 2.4923 seconds and 0.3899 seconds, respectively.

For calculating the precision and recall values, number of true detections (TP), false positive (FP) and false negative (FN) detections are determined. In order to determine these values, intersection over union (IoU) for all the detections are utilized. Calculation of IoU involves computing the overlap between the ground truth object and the detections. Since the purpose of this work is to find a suitable landing location, the threshold for IoU is set as 95%. It means that if the IoU for a detection is smaller than this threshold then it is considered as FP, otherwise TP. On the other hand, any misdetections of an object are counted as FN.

In the terminology of object detection, the precision is defined as the probability of the detected objects matching the actual objects. On the other hand, recall is a way to measure the probability actual objects being correctly detected.

Once the related quantities are determined, the precision and recall are calculated as follows:

$$precision = \frac{TP}{TP + FP} \tag{1}$$

$$recall = \frac{TP}{TP + FN} \tag{2}$$

There are five test images taken from five different altitudes, hence a total 25 images are used for evaluating the performance object detection. Besides, the algorithm is expected to work efficiently at different times of the day. Therefore, the same experiments were repeated by changing the brightness of the test images. The added brightness amounts vary from -20% to 60%. The related results are given in Table 1.

Table 1. Precision and recall for different brightness levels and altitudes

	Altitude									
Amount of Brightness Added (%)	1m		2m		3m		4m		5m	
	Precision	Recall	Precision	Recall	Precision	Recall	Precision	Recall	Precision	Recall
-20	0.916	0.916	0.850	0.950	0.875	0.916	0.812	0.916	0.833	0.875
-10	0.916	1.000	0.900	1.000	0.875	0.916	0.875	0.937	0.875	0.916
0	1.000	1.000	1.000	1.000	0.958	1.000	0.937	1.000	0.916	1.000
+10	1.000	1.000	1.000	1.000	0.958	1.000	0.937	1.000	0.916	1.000
+20	0.916	0.916	0.900	0.950	0.916	0.916	0.875	0.937	0.916	0.916
+40	0.875	0.916	0.850	0.900	0.875	0.875	0.812	0.875	0.833	0.875
+60	0.833	0.833	0.800	0.850	0.833	0.850	0.812	0.812	0.791	0.833

As can be seen from the Table 1 that the highest precision and recall values are obtained at low altitudes (1m and 2m) when no or +10% brightness is added to the images. It is also notable that the results belonging to brightness addition of 0 and +10% are identical for all of the altitudes. It means that the object detection is robust to addition of small amount of illumination. On the other hand, when the brightness or darkness of the images are increased, rate of FP and FN detections increase as well yielding decrements in precision and recall values. Preprocessing of the images using various filters or histogram equalization may be a useful step to improve the detection performance under different illumination levels.

When the table is analyzed according to different altitude levels, slight decrements in performance are observed as the altitude is increased. Thus, it may be a good practice to check the object locations during the emergency landing so that the detected locations may be updated when necessary. Furthermore, the recall value is generally higher than the precision value for all of the test instances. This means that the rate of FN detections is smaller than FP detections. When the application area of the framework is considered, burden of a FN detection is higher than a FP detection because misdetection of an object (i.e. FN) may cause a crash. However, on the other hand, detecting an object at an available area (i.e. FP) will just cause the runtime of the program to increase.

The overall accuracy of landing site detection is directly related with speed and performance of object detection step. As a result, high speed, precision, and recall values indicate the suitability of this method for autonomous landing.

4. CONCLUSION

An emergency landing system framework is proposed together with the details of the related image processing algorithm. The system is intended to work without any kind of markers showing the landing zone. Additionally, it does not utilize GPS signals, which may be unavailable under certain circumstances. It is based on direct detection of a suitable landing zone by processing of images taken from the onboard camera on the UAV. Since it does not involve any training and testing of a predictive model, the computational load is low and hence the corresponding response time is reasonable. On average, it takes around 2.5 seconds to make the detection for a single board computer and 100% of correct detection rate is achieved for the images taken from 1m and 2m. The smallest precision and recall values are 79.1% and 81.2%, respectively. These results show that the method is suitable for real-world scenarios. In addition, higher detection performance at lower altitudes means that the algorithm should be fast enough to make a final decision at 2 meters. In the future, the object detection may be run at different altitudes of the emergency landing process and update the landing trajectory accordingly. Also, the latencies in the data transfer pipeline may be considered for more accurate response time. This method is obviously intended to work on terrestrial zones. In other words, it may not detect water area, which is not a suitable zone for landing. Therefore, the algorithm may be improved to work on the images involving water area.

ACKNOWLEDGEMENT

This research was supported by Scientific Research Project Unit of Adana Alparslan Türkeş Science and Technology University with the project number of 19119001.

REFERENCES

AMAZON (2017). Prime Air. from https://www.amazon.com/Amazon-Prime-Air/b?ie=%20UTF8&node=8037720011.

Aydin B, Selvi E, Tao J & Starek M (2019). Use of Fire-Extinguishing Balls for a Conceptual System of Drone-Assisted Wildfire Fighting. Drones, 3(1). https://doi.org/10.3390/drones3010017

Barták R, Hraško A & Obdržálek D (2014). On autonomous landing of AR.Drone: Hands-on experience. Proceedings of the 27th International Florida Artificial Intelligence Research Society Conference, FLAIRS 2014: 400-405.

Cabrera-Ponce A A & Martinez-Carranza J (2017). A vision-based approach for autonomous landing. 2017 Workshop on Research, Education and Development of Unmanned Aerial Systems (RED-UAS). Linköping, Sweden. DOI: 10.1109/RED-UAS.2017.8101655

Canny J (1986). A Computational Approach to Edge Detection. IEEE Transactions on Pattern Analysis and Machine Intelligence PAMI-8(6): 679-698. DOI: 10.1109/TPAMI.1986.4767851

Chen W, Yue H, Wang J & Wu X (2014). An improved edge detection algorithm for depth map inpainting. Optics and Lasers in Engineering, 55: 69–77. https://doi.org/10.1016/j.optlaseng.2013.10.025

Sani M F & Karimian G (2017). Automatic navigation and landing of an indoor AR. drone quadrotor using ArUco marker and inertial sensors. 2017 International Conference on Computer and Drone Applications (IConDA), Kuching, Malaysia. DOI: 10.1109/ICONDA.2017.8270408

Fitzgerald D & Walker R (2005). Classification of Candidate Landing Sites for UAV Forced Landings. AIAA Guidance, Navigation, and Control Conference and Exhibit, San Francisco, California.

Fitzgerald D, Walker R & Campbell D (2005). A Vision Based Emergency Forced Landing System for an Autonomous UAV. Australian International Aerospace Congress, Melbourne, Australia.

Guo X, Denman S, Fookes C, Mejias L & Sridharan S (2014). Automatic UAV Forced Landing Site Detection Using Machine Learning. 2014 International Conference on Digital Image Computing: Techniques and Applications (DICTA). Wollongong, NSW, Australia. DOI: 10.1109/DICTA.2014.7008097

Heincke B, Jackisch R, Saartenoja A, Salmirinne H, Rapp S, Zimmermann R, Pirttijärvi M et al. (2019). Developing multi-sensor drones for geological mapping and mineral exploration: setup and first results from the MULSEDRO project. Geological Survey of Denmark and Greenland Bulletin 43. https://doi.org/10.34194/GEUSB-201943-03-02

Ho H W (2017). Autonomous landing of Micro Air Vehicles through bio-inspired monocular vision. PHD Thesis, ISBN: 978-94-6186-818-3

Hoffmann G M, Huang H, Waslander S L & Tomlin C (2007). Quadrotor Helicopter Flight Dynamics and Control: Theory and Experiment. AIAA Guidance, Navigation and Control Conference and Exhibit, South Carolina

Jakob S, Zimmermann R & Gloaguen R (2016). Processing of drone-borne hyperspectral data for geological applications. 2016 8th Workshop on Hyperspectral Image and Signal Processing: Evolution in Remote Sensing (WHISPERS). Los Angeles, CA, USA. DOI: 10.1109/WHISPERS.2016.8071689

Kim J & Sukkarieh S (2002). Flight Test Results of GPS/INS Navigation Loop for an Autonomous Unmanned Aerial Vehicle (UAV). Proceedings of the 15th International Technical Meeting of the Satellite Division of The Institute of Navigation (ION GPS 2002). Portland, OR, 510 - 517

Kumar K, Li J & Khan S (2015). Comparative Study on Various Edge Detection Techniques for 2-D Image. International Journal of Computer Applications 119(22), 6-10.

Lee D, Lim H, Kim H J & Kim Y (2012). Adaptive Image-Based Visual Servoing for an Underactuated Quadrotor System. Journal of Guidance, Control, and Dynamics, 35(4), 1335-1353.

Lee M R, Su S, Yeah J E, Huang H & Chen J (2014). Autonomous landing system for aerial mobile robot cooperation. 2014 Joint 7th International Conference on Soft Computing and Intelligent Systems (SCIS) and 15th International Symposium on Advanced Intelligent Systems (ISIS). Kitakyushu, Japan, DOI: 10.1109/SCIS-ISIS.2014.7044826

Liteye (2018). HK$1 million in damage caused by GPS jamming that caused 46 drones to plummet during Hong Kong show. from https://liteye.com/hk1-million-in-damage-caused-by-gps-jamming-that-caused-46-drones-to-plummet-during-hong-kong-show/.

Lopez-Franco C, Gomez-Avila J, Alanis A, Arana-Daniel N & Villaseñor C (2017). Visual Servoing for an Autonomous Hexarotor Using a Neural Network Based PID Controller. Sensors, 17(8), 1865. https://doi.org/10.3390/s17081865

Lu A, Ding W & Li H (2013). Multi-information Based Safe Area Step Selection Algorithm for UAV's Emergency Forced Landing. Journal of Software, 8(4), 995-1002.

Lunghi P, Ciarambino M & Lavagna M (2015). Vision-Based Hazard Detection With Artificial Neural Networks for Autonomous Planetary Landing. In 13th ESA/ESTEC Symposium on Advanced Space Technologies in Robotics and Automation, ASTRA

Mazeh H, Saied M, Shraim H and F. Clovis (2018). Fault-Tolerant Control of an Hexarotor Unmanned Aerial Vehicle Applying Outdoor Tests and Experiments. IFAC-PapersOnLine 51(22), 312-317. https://doi.org/10.1016/j.ifacol.2018.11.560

Nemati A, Sarim M, Hashemi M, Schnipke E et al. (2015). Autonomous Navigation of UAV through GPS-Denied Indoor Environment with Obstacles. AIAA SciTech, Kissimmee, Florida

Nguyen N P, Mung N X & Hong S K (2019). Actuator Fault Detection and Fault-Tolerant Control for Hexacopter. Sensors 19(21), 4721. https://doi.org/10.3390/s19214721

PropotoUAV (2019). Drones are being used for weather forecasting by meteorologists. from https://www.prophotouav.com/meteorologists-storm-weather-drones/.

Martin S, Bange J & Beyrich F (2010). Meteorological profiling of the lower troposphere using the research UAV "M^{2}AV Carolo". Atmospheric Measurement Techniques Discussions 4, 705–716. DOI:10.5194/amt-4-705-2011

Veroustraete F (2015). The Rise of the Drones in Agriculture. EC Agriculture 2(2), 325-327.

Zhao H & Wang Z (2012). Motion Measurement Using Inertial Sensors, Ultrasonic Sensors, and Magnetometers With Extended Kalman Filter for Data Fusion. IEEE Sensors Journal - IEEE SENS J 12(5), 943-953. DOI: 10.1109/JSEN.2011.2166066

CONTENTS

ISSN 2587-1366

TURKISH JOURNAL OF ENGINEERING

VOLUME 5 ISSUE 4 OCTOBER 2021